Alkaline Electrochemical Water Oxidation by NiFe-based Metal Oxide Catalysts

By

Jamie Yung-Chieh Chen

A dissertation submitted in partial fulfillment of

the requirements for the degree of

Doctor of Philosophy

(Chemistry)

at the

UNIVERSITY OF WISCONSIN-MADISON

2015

Date of final oral examination: 07/16/2015
The dissertation is approved by the following members of the Final Oral Committee:
Shannon S. Stahl, Professor, Chemistry (Inorganic)
Thomas C. Brunold Professor, Chemistry (Inorganic)
Robert J. Hamers, Professor, Chemistry (Materials)
Kyoung-Shin Choi, Professor, Chemistry (Materials/Inorganic)
Song Jin, Professor, Chemistry (Materials)

Alkaline Electrochemical Water Oxidation by Ni/Fe-based Metal Oxide Catalysts

Jamie Yung-Chieh Chen

Under the supervision of Professor Shannon S. Stahl

At the University of Wisconsin-Madison

ABSTRACT:

The oxygen evolution reaction (OER) is the ideal anodic reaction for a photoelectrochemical cell that converts solar energy into chemical fuels; however it is currently limited by catalyst efficiency and cost. In order to overcome these limitations, much effort has been devoted to the discovery of more efficient earth-abundant metal oxide electrocatalysts, particularly mixed-metals oxides, as well as understanding their mechanisms. This thesis addresses both of these challenges.

An O_2-sensitive fluorescence-based screening assay was developed and arrays of ternary oxide electrocatalysts were examined. Analysis of the intensity of the resulting fluorescence signal allowed for the identification of compositions with high activity. Compositions exhibiting the highest activities were validated through Tafel analyses, and good qualitative agreement was observed between screening results and electrochemical measurements. While Fe is known to improve the activity of Ni oxide catalysts, the incorporation of a third metal into Ni-Fe binary oxides was often observed to further enhance OER activity, with Ni-Fe-Al amorphous oxide showing the highest activity during our initial screening.

The previously observed instability led to the investigation of a well-defined $NiFeAlO_4$ inverse spinel oxide as a water oxidation electrocatalyst, where structural analyses confirmed the

substitution of Al for Fe lattice sites. A comparison of electrochemical activity against compositionally and structurally relevant oxides, including the known OER catalysts NiO, NiFe 9:1, and $NiFe_2O_4$ established $NiFeAlO_4$ as a superior electrocatalyst with no Al leaching, and cyclic voltammograms of the oxides indicated that the electron-withdrawing M^{+3} ions in the inverse spinels make Ni^{+2} sites more difficult to oxidize. Furthermore, it was observed that neither of the bimetallic spinel oxides ($NiFe_2O_4$ & $NiAl_2O_4$) outperformed $NiFeAlO_4$, suggesting a unique synergistic effect between all three metal sites that influences the OER rate determining step.

In addition to catalyst discovery, we also pursued mechanistic studies to better understand the dramatic activity enhancement that results when Fe is added to various Ni oxide electrocatalysts. Operando Mössbaurer spectroscopic studies of a 3:1 Ni:Fe layered oxide and anhydrous Fe oxide electrocatalyst was performed. Catalyst materials were prepared by a hydrothermal precipitation method that enabled growth of the oxide catalysts directly on a carbon paper electrode, thereby enhancing charge transport and mechanical stability needed for the operando studies. Fe^{+4} species are evident in the NiFe-oxide catalyst during steady-state water oxidation, accounting for up to 21% of the total Fe in the catalyst. No Fe^{+4} is detected under any conditions in the Fe-oxide catalyst. The lifetime of the observed Fe^{+4} species suggests they do not participate directly in water oxidation; however, their presence has important implications for the promoting effect of Fe in NiFe-oxide electrocatalysts.

.

ACKNOWLEDGEMENTS

I would first like to thank Professor Shannon Stahl for his continual support, trust, and ppatience over the past 6 years, as I paddle my way through the unfamiliar deep waters of materials chemistry and heterogeneous catalysis. Without his guidance, demand for perfection, and understanding, I would not be the scientist that I am today.

I would also like to thank my collaborators at Argonne National Laboratory. Dr. Jeffrey Miller for being very helpful with our XAS experiments and have been incrdibly generous with his time walking me through all the data analysis step-by-step on multiple occasions. Dr. Ercan Alp taught me everything I know about Mössbauer and synchrotron Mössbauer spectroscopy, and took the time to help me collect data and perform analysis. Without the help of these two PIs, I could not have completed my research project.

I would also like to thank all the friends I've made in and outside of graduate school for all the help and support, both in science and in getting through graduate school. This very difficult journey would not have been possible without these people who continuously reminded me of the good work I have done and how much I have overcome.

Finally, I want to thank my loving family, especially my father who wanted more than anything to see me finish my PhD, for being the consistent source of encouragement, inspiration, and support. They have always been there for me and have always believed in me. I would not be able to get to where I am today if not for the sacrifices that they have made for me, and for that, I'm forever grateful.

TABLE OF CONTENTS

Abstract i

Acknowledgements iii

Table of Contents iv

List of Figures vii

List of Schemes x

List of Tables xi

List of Equations xii

Abbreviations and Acronyms xiii

Chapter I. Introduction to NiFe-Based Metal Oxide OEC 1

1.1 Introduction 2

1.2 Ni Oxide Electrocatalysts and Fe Impurity 5

1.3 NiFe Composite Oxygen Evolution Electrocatalysts 5

1.3.1 Discovery 5

1.3.2 Investigation of Different Types of NiFe Composite OEC 6

1.3.2.1 NiFe Composite Anode Prepared by Coprecipitation and Electrodeposition 7

1.3.2.2 NiFe Composite Anode prepared by Calcination 8

1.3.2.3 NiFe Composite Anode prepared by Hydrothermal Synthesis 9

1.4 Ni/Fe/X OEC 11

1.4.1 Well Defined Ni/Fe/X Oxides 11

1.4.2 Amorphous Ni/Fe/X Oxides 13

1.5 Mechanistic Investigation of NiFe-LDH Electrocatalysts 15

1.5.1 X-ray Absorption Spectroscopic Studies 16

1.5.2 Mössbauer Spectroscopic Studies 17

1.5.3 Other *In situ* Studies 18

1.6 Thesis Overview 19

Chapter II. Development of an O_2-Sensitive Fluorescence Quenching Screening Assay 24

2.1 Introduction 25
2.2 Results and Discussion 26
2.3 Conclusion 31
2.4 Experimental Details 32
2.4.1 General Experimental Conditions and Apparatus 32
2.4.1.1 The Electrochemical Cell 32
2.4.1.2 The O_2-Senseing Paint-covered Mesh 33
2.4.2 Sample Preparation and Calcination 33
2.4.3 Data Acquisition and Processing 35
2.4.4 Tabulated Catalyst Screening Activities 38
2.4.5 Tafel Measurements on Selected Catalysts 40
2.4.5.1 Electrode Preparation 40
2.4.5.2 Tafel Analysis 40
2.4.6 O_2 Detection of $Ni_{0.4}Fe_{0.2}Al_{0.4}$ 42
2.4.7 SEM Imagine and EDS Elemental Analysis of $Ni_{0.4}Fe_{0.2}Al_{0.4}$ 42
2.5 References 44

Chapter III. Inverse Spinel $NiFeAlO_4$ as a Highly Active OECtalyst 47
3.1 Introduction 48
3.2 Results and Discussions 49
3.2.1 Physical Characterizations of the Oxides 49
3.2.2 Electrochemical Analysis of the Oxides 54
3.3 Conclusions 58
3.4 Experimental Details 58
3.4.1 Catalyst Preparation 59
3.4.2 Materials Characterizations 59
3.4.3 Rietveld Refinement and XRD Simulation 60
3.4.4 Electrochemistry 61
3.4.4.1 Electrochemical Activity Normalization Methods 62
3.4.5 Oxygen Detection 66
3.4.6 EDS Analysis of $NiFeAlO_4$ Before and After 15-hour Electrolysis 67
3.4.7 X-ray Absorption Spectroscopy 67
3.5 References 70

Chapter IV. *In operando* Mössbauer Analysis of NiFe- and Fe-Oxide OEC 75
4.1 Introduction 76
4.2 Results and Discussion 77
4.2.1 Catalyst Synthesis 77
4.2.2 Physical Characterizations 77
4.2.3 Cyclic Voltammetry 80
4.2.4 Mössbauer Measurements 80
4.3 Conclusion 85
4.4 Experimental Details 85
4.4.1 Materials 85
4.4.2 Syntheses 86
4.4.2.1 $^{57}FeSO_4 \bullet 7H_2O$ 86
4.4.2.2 Hydrophilic-Treated Carbon Paper 87
4.4.2.3 Preparation of Ni/Fe-LDH Catalyst on Carbon Paper Electrode 87
4.4.3 Characterization 88
4.4.4 *In operando* Mössbauer-Electrochemical Cell 88
4.4.5 Mössbauer Measurements 90
4.4.6 Spectroscopic Data of Electrodeposited NiFe-LDH Catalysts 93
4.5 References 94

Appendix I. Optimization Tables of NiFe-LDH Synthesis directly on Carbon Paper 98

LIST OF FIGURES

Figure 1-1. X-ray crystal structure of the oxygen evolving complex in photosystem II 3

Figure 1-2. The influence of a trace Fe impurity in KOH electrolyte 7

Figure 1-3. CVs of NiFe-LDH with varying Fe concentration. Figure taken from reference 11. 8

Figure 1-4. LSV of crystalline vs. electrodeposited NiFe-LDH with and without CNT 10

Figure 1-5. Schematic representation of LDH structures during exfoliation. 10

Figure 1-6. Contour plots of Tafel slope, η_{onset}, and η @ J=1 mA/cm^2 14

Figure 2-1. Schematic drawing of the electrochemical cell 27

Figure 2-2. Oxide composition diagram and arrangement on the electrode array 28

Figure 2-3. Image processing sequence 29

Figure 2-4. Activity vs. composition plot for the Ni-Fe-Al and Ni-Ca-Fe triads 30

Figure 2-5. a) Representative Tafel data and correlation of catalyst activity 31

Figure 2-6. Electrochemical cell used in this screening study 33

Figure 2-7. Template for spotting mixtures on a FTO electrode. 35

Figure 2-8. Fully assembled apparatus, except for connections to the potentiostat 36

Figure 2-9. Fluorescence Screening Results for triads examined in this study 40

Figure 2-10. Tafel curves of selected highly-active (and less-active) compositions 41

Figure 2-11. O_2 detection trace of $Ni_{0.4}Fe_{0.2}Al_{0.4}$ 42

Figure 2-12. SEM images of the $Ni_{0.4}Fe_{0.2}Al_{0.4}$ catalyst before and after electrolysis. 42

Figure 2-13. Elemental mapping of $Ni_{0.4}Fe_{0.2}Al_{0.4}$ catalyst before and after electrolysis. 43

Figure 3-1. Ternary diagrams showing relative electrocatalytic OER activity of thin-films 48

Figure 3-2. Mo Kα pXRD patterns of NiO and Ni-containing mixed metal oxides 49

Figure 3-3. Simplified structural representation of $NiFeAlO_4$ 50

Figure 3-4. Ni-edge XAS spectra of the oxides 51

Figure 3-5. Fe-edge XAS spectra of the oxides 52

Figure 3-6. Experimental (black) and simulated (red) Cu Kα pXRD patterns for $NiFeAlO_4$ 53

Figure 3-7. Mo Kα pXRD spectra of oxides examined for electrochemical activity 54

Figure 3-8. Redox properties of different Ni-based oxide materials. 55

Figure 3-9. Steady-state Tafel plot of the oxides in the low current density linear regime 56

Figure 3-10. SEM images of oxides with particle size and BET surface area measurements. 60

Figure 3-11. CV illustrating area integrated in the determination of redox-active Ni-atom. 63

Figure 3-12. Correlation between the moles of redox active Ni and BET surface area. 63

Figure 3-13. BET Surface area normalized Tafel plot 64

Figure 3-14. Example cyclic voltammetry and i – v plot of acetylene black 65

Figure 3-15. CV traces of acetylene black (AB), $NiFeAlO_4$, and [AB+$NiFeAlO_4$]. 66

Figure 3-16. O_2 detection tracewith calculated Faradaic yield 66

Figure 3-17. Electrolysis trace of $NiFeAlO_4$ over 15 hours. 67

Figure 4-1. SEM images of NiFe- and Fe-oxide catalysts. 78

Figure 4-2. Powder X-ray diffraction pattern of the NiFe-LDH and Fe-catalyst precursors 79

Figure 4-3. EDX elemental mapping of the 3:1 NiFe-LDH catalyst 80

Figure 4-4. CV of Ni-, 3:1 Ni:Fe-, and Fe-oxide catalysts. 80

Figure 4-5. Mössbauer spectra of each catalyst 82

Figure 4-6. Two sets of parameters were found to produce reasonable fit for the Fe^{+4} specie. 83

Figure 4-7. *Operando* Mössbauer-electrochemical cell. 88

Figure 4-8. View of the experimental setup for *operando* Mössbauer experiment 91

Figure 4-9. The working electrode assembly 92

Figure 4-10. Mössbauer spectra of electrodeposited 40% Fe NiFe-LDH 93

Figure 4-11. Ni and Fe K-edge XAS spectra of electrodeposited 20% Fe NiFe-LDH. 94

LIST OF SCHEMES

Scheme 1-1. Schematic representations of photoelectrochemical cell 2

Scheme 2-1. Catalyst array preparation workflow 34

Scheme 2-2. Image Processing Procedure, Co-Al-Ni data shown 37

Scheme 4-1. Design prints for the *operando* Mössbauer-electrochemical cell 89

LIST OF TABLES

Table 1-1. Summary of Parameters for Cr, V, doped $NiFe_2O_4$ and Fe doped $NiMoO_4$ OEC 12

Table 1-2. Summary of Parameters for Mg-doped $NiFe_2O_4$ OEC 13

Table 2-1. List of metal triads investigated in this study 28

Table 2-2. Composition of metals A, B, and C of each of the 21 spots on the FTO anode 35

Table 2-3. Assay data post-processing macro for use with ImageJ 38

Table 2-4. Elemental analysis of $Ni_{0.4}Fe_{0.2}Al_{0.4}$ catalyst before and after electrolysis. 43

Table 3-1. Elemental analysis of $NiFeAlO_4$ before and after electrolysis. 57

Table 3-2. Averaged moles of redox active Ni 62

Table 3-3. Tafel slopes of the oxides examined 64

Table 3-4. Averaged capacitance of the oxides in Farad. 65

Table 3-5. Ni and Fe EXAFS Fittting Results 68

Table 4-1. Specific Reaction Conditions Employed for Catalyst Synthesis 87

Table 4-2. Mössbauer Parameters for the layered 3:1 NiFe-Oxide Catalyst 92

Table 4-3. Mössbauer Parameters for the hydrous Fe-Oxide Catalyst. 92

Table 5-1. Anaerobic vs. Aerobic Condition 99

Table 5-2. $FeSO_4 \cdot 7H_2O$ vs. $FeCl_2$ 100

Table 5-3. TEA vs. EG and Reducing Urea Concentration 100

Table 5-4. Effect of $[M]_{tot}$ on Catalyst Loading and Reducing Reaction Volume 101

TABLE OF EQUATIONS

Equation 1-1. The water splitting reaction 3

Equation 3-1. The water oxidation half reaction 48

ABBREVIATION AND ACRONYMS

η	Overpotential
CP	Carbon Paper
CPE	Constant Potential Electrolysis
CNT	Carbon Nanotube
CV	Cyclic Voltammogram
EDX	Energy Dispersive X-Ray
EG	Ethylene Glycol
EXAFS	Extended X-ray Absorption Fine Structure
FTO	Fluorine-doped Tin Oxide
GC	Glassy Carbon
IDA	Interdigitated Array
IS	Isomer Shift
LDH	Layered Double Hydroxide
MWCNT	Multiwalled Carbon Nanotube
OEC	Oxygen Evolution Catalyst
OER	Oxygen Evolution Reaction
PEC	Photoelectrochemical Cell
QS	Quadrupole Splitting
SEM	Scanning Electron Microscope/Microscopy
TEA	Triethanolamine
XAS	X-ray Absorption Spectroscopy

XANES	X-ray Absorption Near Edge Spectroscopy
XPS	X-ray Photoelectron Spectroscopy
XRD	X-ray Diffraction

Chapter I

Introduction to NiFe-Based Metal Oxide Oxygen Evolution Electrocatalysts

1.1 Introduction

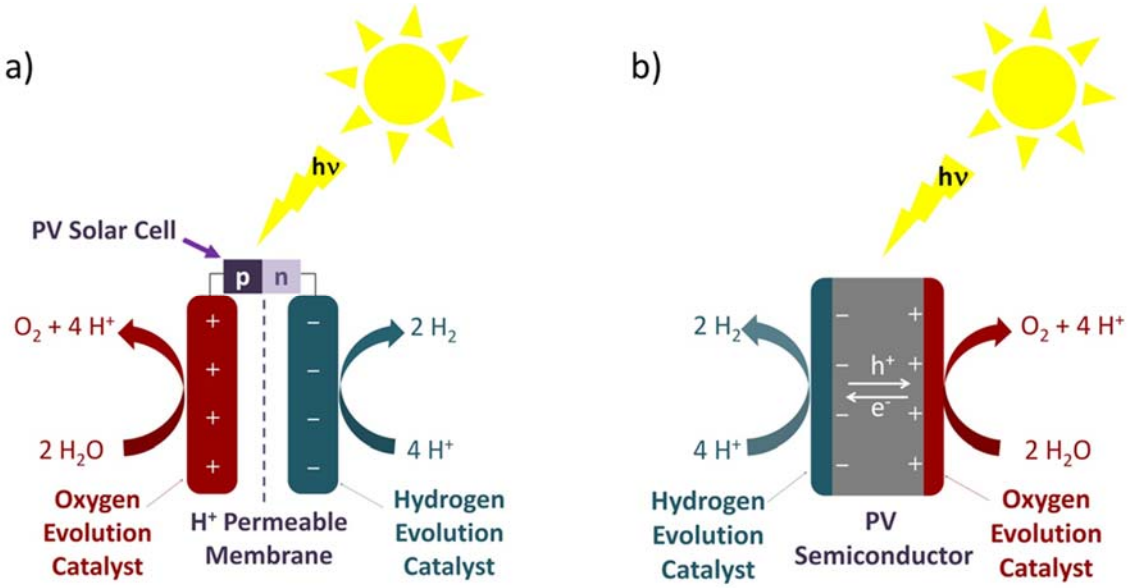

Scheme 1-1. Schematic representations of indirect (a) and direct (b) photoelectrochemical configurations for water splitting.

As the world's energy consumption continues to increase, one of the biggest technological challenges faced by scientists is to reduce our dependence on non-renewable sources of energy (such as fossil fuels and coals) and finding ways to efficiently utilize available renewable energy sources. Among them, the sun provides more than enough energy in one day to supply global energy needs for an entire year. However, due to uneven distribution and availability only during the day, new technologies are needed to enable efficient storage of solar energy. One such technology is the photoelectrochemical cell (PEC) in either the indirect or direct configuration (Scheme 1-1). The former employs a photovoltaic (PV) solar cell coupled to an electrolysis cell, whereas the latter features a direct integration of the electrocatalysts with the charge-separating PV semiconductor.

In a photoelectrochemical cell, a chemical species is oxidized at the anode compartment to provide the protons and electrons necessary for a variety of fuel-forming reactions in the cathode compartment, and the driving force for these reactions is solar energy. Water splitting, where an

abundant and readily assessable feedstock is used, is the ideal anodic reaction: water molecules are oxidized to dioxygen at the anode, releasing four protons and four electrons that can recombine to form hydrogen gas at the cathode (Eq. 1-1). However, the development of an efficient and inexpensive water oxidation catalyst remains the major bottleneck in the realization of such a system.

$$2\,H_2O \longrightarrow O_2 + H_2 \qquad \text{(Eq. 1-1)}$$

$$2\,H_2O \longrightarrow O_2 + 4\,H^+ + 4\,e^- \quad \text{Water Oxidation}$$

$$4\,H^+ + 4\,e^- \longrightarrow 2\,H_2 \quad \text{Proton Reduction}$$

Equation 1-1. The water splitting reaction and the corresponding anodic (water oxidation) and cathodic (proton reduction) half reactions

Water oxidation is a thermodynamically uphill reaction, requiring 1.23 V vs. NHE at pH 0. Additionally, the catalyst must also be able to manage the transfer of four protons and electrons, with the concomitant formation of an O–O bond to avoid high overpotential, which introduces a high kinetic barrier to the process. Furthermore, if such a system is to be practical in large scale solar energy conversion, the catalyst must be sufficiently robust to withstand strongly oxidizing conditions over long periods of time without significant loss of activity, and be made from inexpensive, earth-abundant elements.

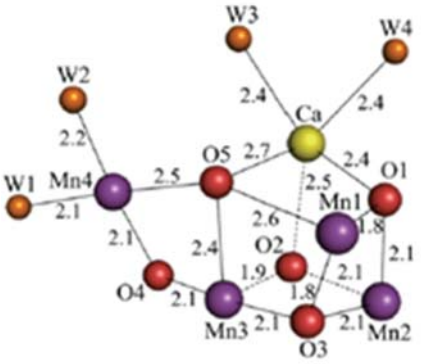

Figure 1-1. X-ray crystal structure of the oxygen evolving complex in photosystem II (PDB code 3WU2). Figure taken from reference 1.

Fortunately, inspiration can be drawn from the oxygen-evolving complex of photosystem II (PS II). A recent high-resolution crystal structure of PS II has provided an accurate picture of the oxygen-evolving complex (Figure 1-1).[1] It consists of an inorganic Mn_4CaO_5 cluster with water molecules bond to both Mn and Ca sites. Intimate interaction with the surrounding amino acids and extensive hydrogen-bonding networks were also observed which are proposed to manage the multiple proton and electron transfers and O–O bond formation. This complex is highly active; however, it also requires regeneration every thirty minutes due to decomposition. Many mechanistic proposals for water splitting by the OEC favor a series of light-induced proton-coupled-electron transfer events resulting in the formation of an electrophilic Mn^{+4} oxo species. Subsequent nucleophilic attack by water furnishes the O–O bond, which is followed by O_2 release.[2] This inorganic metal oxide cluster provides inspiration for designing an artifical catalytst system. Such system should be composed of highly stable inorganic metal oxide clusters with metal ions capable of multi-electron processes within a potential range comparable to the thermodynamic potential of water oxidation. Furthermore, components capable of facilitating water adsorption and proton transfer must also be present.

Many transition metal oxides have been examined as oxygen evolution catalyst (OEC) under a variety of pHs. Base metal oxides offers the most economically feasible catalysts and are most stable under alkaline conditions. Among the base metal oxides that have been studied, oxides containing at least Ni and Fe have been shown to be the most active under alkaline conditions. This review will provide an overview of the development of catalysts based upon the NiFe binary oxide catalyst, as well as studies that sought to elucidate the origin of the beneficial effects of Fe.

1.2 Ni Oxide Electrocatalysts and Fe Impurity

Ni oxide has traditionally been used as an OEC in commercial alkaline electrolyzers due to its high activity and resistance to corrosion.[3] In recent years, Nocera and co-workers have renewed interest in this material through a series of electrochemical and spectroscopic studies of anodically deposited thin Ni oxide film in borate buffer (pH 9.2).[4] One notable observation from their studies was that the Ni-B_i catalyst required 30 – 60 minutes of anodization in the borate buffer, during which time an OER activity enhancement of more than two orders of magnitude was observed. This activity increase upon anodization was also observed by Noufi[5] where electrodeposited thin Ni oxide film was examined in 1 M NaOH (pH 14). Nocera and co-workers examined both the as-prepared and anodized films using X-ray absorption spectroscopy. They found that upon anodization, the Ni-B_i catalyst transformed from having Jahn-Teller distorted Ni^{+3} sites (i.e. β-NiOOH) to a new phase that was characterized as γ-NiOOH, concomitant with an increase in the average oxidation state of Ni to +3.7.

However, a recent study by Boettcher et al. demonstrated that the improved activity of the Ni-B_i systems results not from anodization but rather the incorporation of Fe impurities from the borate buffer during the experiment.[6] Furthermore, the presence of Fe impurities was also identified in KOH – the electrolyte of choice for the Ni oxide catalyst systems.[7]

1.3 NiFe Composite Oxygen Evolution Electrocatalysts

1.3.1 Discovery

The beneficial effect of the presence of Fe in Ni-based OECs was first serendipitously discovered through observations made in the field of alkaline battery research. In alkaline battery systems that uses $Ni(OH)_2$ electrodes, Fe impurities were found to be detrimental. It was observed that an Fe impurity present in as low as 0.35% led to a decrease in charge capacity and diminished

life cycle in these batteries by facilitating OER.[8] This undesirable side reaction, however, is a rather challenging anodic reaction that limited the efficiency of alkaline electrolyzers, and many researchers began to investigate OER catalyzed by the mixed NiFe oxide.

1.3.2 Investigation of Different Types of NiFe Composite OEC

Mixed NiFe oxide electrodes have been prepared via a variety of methods. Traditionally, room temperature coprecipitation and cathodic deposition methods were used to prepare these composite electrodes. The former involves the addition of hydroxide ions to a solution containing Ni and Fe salts. Cathodic deposition utilizes the same principle, however the hydroxide ions are generated *in situ* at the electrode surface, which then cause metal ions in solution to precipitate onto the electrode. The as-prepared materials from these two methods can be described as mixed NiFe hydroxides which upon oxidation turns into oxyhydroxides. These hydroxides and oxyhydroxides are generally proposed to have a layered structure with intercalating ions or water molecules, and are thus called the layered double hydroxides (LDH).

Another approach is to prepare oxides via calcination/annealing at elevated temperatures (100-850 ^{o}C). NiFe mixed oxides prepared using this approach are dehydrated and do not possess the layered structure. Additionally, depending on the calcination temperature the inverse spinel $NiFe_2O_4$ can also form, which itself has been studied as an OEC.[9]

Recently, efforts have been directed towards hydrothermal synthesis of crystalline nanoplates of LDH in order to generate high surface area materials. Although also performed at elevated temperatures, the presence of water in hydrothermal synthesis helps to maintain the layered structure and prevent bulk oxide formation. In addition to engineering a material with high activity, the exposure of a large number of active sites and the well-defined nature of this type of material

is also beneficial for any mechanistic studies. Regardless of the method of preparation, the extraordinary activity of the NiFe oxide electrode is demonstrated in all cases.

1.3.2.1 NiFe Composite Anode Prepared by Coprecipitation and Electrodeposition

Córdoba and Macagno[10] examined coprecipitated composite electrodes prepared by alternate immersion of a Pt substrate into a bath containing [$NiSO_4$ + $FeSO_4$] followed by treatment with NaOH. They showed that the composite electrode outperformed both of the constituent monometallic oxides and an anodic shift of the Ni^{+2}/Ni^{+3} redox feature was observed. Additionally, maximum activity was observed with Fe doping between 5-25%, with the 25% Fe sample showing a Tafel slope of 30 mV/dec and a reaction order of 2 with respect to [OH^-].

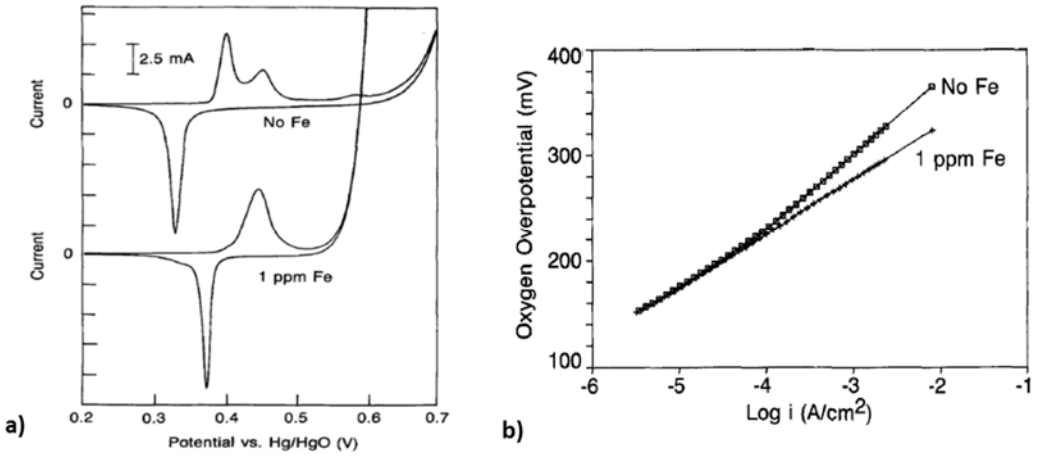

Figure 1-2. The influence of a trace Fe impurity in KOH electrolyte on the CV response (a) and Tafel slope (b) of electrodeposited Ni oxide electrode. Figures taken from reference 7b.

Corrigan[7b] reported the first thorough examination of NiFe oxide electrodes prepared from cathodic deposition. He demonstrated that the KOH electrolyte solution was the source of Fe contamination, and showed that even the presence of 1 ppm of Fe impurity in reagent grade KOH can significantly enhance OER upon repeated voltammetric cycling (Figure 1-2). Additionally, he also provided a method for KOH electrolyte purification via prolonged electrolysis using a Ni metal anode. Relevant OER parameters obtained by Corrigan were similar to those reported by

Córdoba and Macagno. Corrigan showed that the Tafel slope decreases with increasing Fe concentration and the lowest overpotential was achieved between 10-50% Fe (Tafel slope between 21-25 mV/dec).

In a recent complementary study, Bell and co-workers[11] showed that the presence of Fe can systematically modulate the oxidation potential of Ni^{+2}. As can be seen in CVs of NiFe-LDH with varying Fe concentrations (Figure 1-3), increasing Fe doping resulted in an anodic shift of the Ni^{+2} redox feature until Ni^{+2} oxidation completely merged with the OER catalytic wave at >41% Fe. This anodic shift was also accompanied by a reduction in the peak currents of the redox feature. Simultaneously, the onset potential for OER shifts cathodically and is the lowest at 41% Fe. The opposite potential shifts of the redox couple and catalytic wave suggest that while the electron-deficient Fe^{+3} makes the oxidation of Ni^{+2} more difficult, once oxidized, the resulting $Ni^{+3/+4}$ sites are much more potent oxidants in the presence of Fe, until Fe becomes the predominant species.

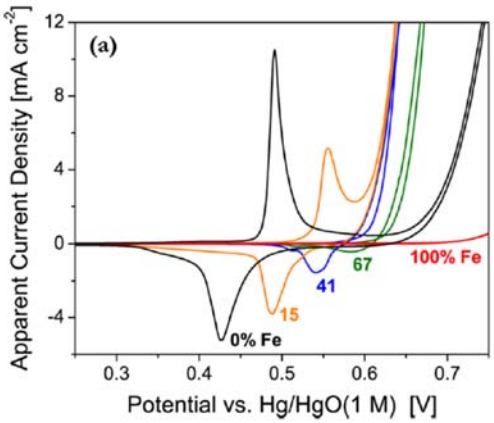

Figure 1-3. CVs of NiFe-LDH with varying Fe concentration. Figure taken from reference 11.

1.3.2.2 NiFe Composite Anode prepared by Calcination

Kitchins examined a series of mixed NiFe oxides prepared via evaporation-induced self-assembly (EISA).[12] A surfactant was used initially to alter bulk oxide composition and

subsequently removed via calcination at 350 ºC and 550 ºC. Fe concentration was varied from 0 - 50%. In all cases, both the NiO and $NiFe_2O_4$ phases were observed, and elemental mapping showed occasional aggregation of Fe. OER activity plateaued with catalysts containing 10-15% Fe and quickly dropped off when dopant exceeded 20%. Slightly higher Tafel slopes of ~40 mV/dec were observed for these mixed oxide electrodes compared to those prepared at room temperature, presumably due to the presence of two different oxide phases as well as their bulk nature.

The 10% Fe composite electrode was also examined by *in operando* X-ray absorption spectroscopy (XAS) in the extended XAS fine structure region (EXAFS). No change was observed in the Ni edge under steady-state turnover, likely due to the bulk nature of this electrode; however, an increase in the intensity of the Fe_{Oh}-Fe_{Td} backscattering peak was seen. The authors suggested that these changes could result from the movement of Fe from the tetrahedral site to the octahedral sites. However, while this spectrum appeared different than that of the pristine catalyst, no differences were observed from that of the *in situ* catalyst under open circuit. It is therefore unclear whether useful insights can be gleaned from this experiment.

1.3.2.3 NiFe Composite Anode prepared by Hydrothermal Synthesis

A recent interesting application of NiFe-LDH prepared using hydrothermal synthesis is the incorporation of multiwalled carbon nanotubes (MWCNT).[13] By adding mildly oxidized MWCNT during a typical synthesis of NiFe-LDH, Dai and co-workers generated the NiFe-LDH/CNT hybrid material. It was demonstrated that the activity of the hybrid catalyst exceeded that of just the NiFe-LDH alone (Figure 1-4a). Furthermore, the authors showed that this crystalline material exhibited higher activity than an amorphous electrodeposited NiFe-LDH catalyst (Figure 1-4b). The authors concluded that the crystalline NiFe-LDH is intrinsically more active towards OER, and the associated CNT network helps to facilitate electron transport.

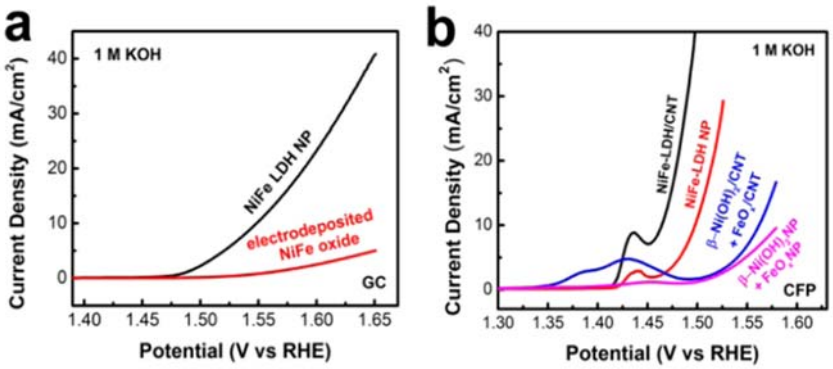

Figure 1-4. Linear sweep voltammograms of (a) crystalline NiFe-LDH nanoplates vs. electrodeposited NiFe-LDH and (b) crystalline NiFe-LDH with and without CNT. Figure taken from reference 13.

Another interesting extension is the application of an "exfoliation" step to the hydrothermally prepared LDH.[14,15] Exfoliation of the LDH is manifested in the delamination and breakage of the layers to expose more active sites. Typically, the as-prepared LDH (Figure 1-5a) first undergoes anion exchange to increase interlayer distance (Figure 1-5b). Subsequently, it is stirred in formamide for days, during which time formamide intercalates between the layers to disrupt existing hydrogen bonding networks or electrostatic forces holding the layers together (Figure 1-5c).

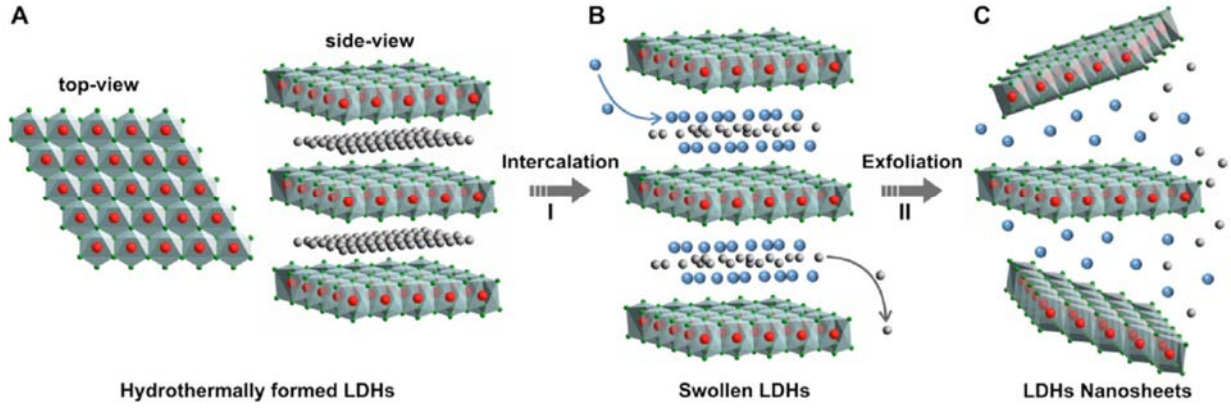

Figure 1-5. Schematic representation of LDH structures during exfoliation. Figure taken from reference 15.

Hu and co-worker[14] examined several metal LDH catalysts for OER and found that NiFe exhibited the highest activity. Upon exfoliation, the activity of NiFe-LDH further improved 4.5

fold at an overpotential of 300 mV. Intriguingly, the activity of exfoliated NiFe-LDH was almost 3 times greater than expected based on the increase in electrochemical surface area. When considered along with the observation that individual LDH sheets break upon exfoliation, the authors suggested that the edge sites might contribute more significantly to OER activity in LDH catalysts.

1.4 Ni/Fe/X OEC

Several researchers have tried to further improve the activity of NiFe bimetallic oxides by the addition of a third metal. However, one of the major limitations in this effort is the difficulty in preparing compositionally and morphologically homogeneous multi-metal oxide, while still being able to systematically vary composition and incorporate any metal of choice. For example, the coprecipitation, electrodeposition, and hydrothermal synthesis methods described previously all relied on the precipitation of metal hydroxides. However, the solubility of metal hydroxides and the starting metal salts varies greatly, making it difficult to systematically vary compositions and sample a wide range of metal ions. On the other hand, calcination methods impose constraints of the thermodynamically favored crystal structure. Phase segregation can be a major issue that complicates data analysis, and often times, composition cannot be varied without also changing the oxide crystal structure.

1.4.1 Well-Defined Ni/Fe/X Oxides

Until recently, most efforts in this area have focused on examining trimetallic inverse spinels. This is in part due to the aforementioned difficulty associated with mixed oxide synthesis. Singh and co-workers have examined Cr and V as transition metal dopants for $NiFe_2O_4$. Both metals exhibited a beneficial effect on the OER activity of $NiFe_2O_4$; however, a direct comparison between the two dopant is not possible based on the information reported by the authors. A

summary of key parameters for the three systems is provided in Table 1-1. For Cr it appears that the most significant effect was the increase in roughness factor, which led to the lowering of potential required to achieve an apparent current density of 100 mA/cm^2. (However, Cr^{+6} detected by X-ray photoelectron spectroscopy may play a role in catalysis.[16]) In contrast, the increase in surface area resulting from V incorporation is much smaller than the magnitude of increase in specific activity, demonstrating an influence on the intrinsic activity of the oxide.[17] Singh and co-workers also examined a series of $NiFeMoO_4$ compounds for OER. In this case, $NiMoO_4$ serves as the parent oxide and Fe is substituting for Ni sites. The enhancement upon Fe incorporation is rather dramatic in this case, which intriguingly was accompanied by a change in the crystal structure to resemble that of an inverse spinel phase.[18]

Table 1-1. Summary of Key Parameters for Cr, V, doped $NiFe_2O_4$ and Fe doped $NiMoO_4$ OEC

Oxide	**η* (mV)** 100 mA/cm$^2_{geom}$	**η (mV)** 300 mA/cm$^2_{geom}$	**j (mA/cm^2)** η=0.7 V	**R_f****	**BET** (m^2/g)	**Tafel Slope** (mV/dec)	**Spec. Activity** (A/m^2)
$NiFe_2O_4$	655	716		~300	38	38	
$NiFe_{1.8}Cr_{0.2}O_4$	622	664		~520	43	37	
$NiFe_{1.6}Cr_{0.4}O_4$	613	656		~770	56	41	
$NiFe_{1.4}Cr_{0.6}O_4$	598	640		~1880	57	39	
$NiFe_{1.2}Cr_{0.8}O_4$	588	629		~1780	54	38	
$NiFeCrO_4$	586	621		~1320	47	40	
$NiFe_2O_4$			11		20.9	~40	20
$NiFe_{1.75}V_{0.25}O_4$			67		22.0	~40	93
$NiFe_{1.5}V_{0.5}O_4$			122		28.8	~40	112
$NiFeVO_4$			104		30.5	~40	107
	η (mV) 100 mA/cm$^2_{geom}$			**j (mA/cm^2)** η=0.65 V	**BET** (m^2/g)	**Tafel Slope** (mV/dec)	**Spec. Activity** (A/m^2)
$Ni_{0.75}Fe_{0.25}MoO_4$	641			154	2.5	33	36
$Ni_{0.5}Fe_{0.5}MoO_4$	640			148	2.8	34	27
$Ni_{0.25}Fe_{0.75}MoO_4$	645			123	1.6	34	36
$NiMoO_4$	n/a			7.9	12.8	75	0.3

* η stands for overpotential; **R_f stands for roughness factor as determined by capacitance measurement

The effect of doping $NiFe_2O_4$ with an alkaline earth metal, mimicking that of the oxygen evolving complex in PS II, has also been investigated. Augustin et. al, prepared Mg-doped $NiFe_2O_4$ and found that Mg also exhibited a beneficial effect on OER activity, with $Ni_{0.4}Mg_{0.6}Fe_2O_4$ requiring the lowest overpotential for achieving a current density of 1.5 mA/cm^2 (Table 1-2). DC conductivity was also the highest for this composition, contributing to its improved activity.

Table 1-2. Summary of Key Parameters for Mg-doped $NiFe_2O_4$ OEC

Oxide	**η** 1.5 mA/cm^2_{geom}	**R_f**	**Tafel Slope** (mV/dec)	**Σ @ 1000 °C** (S/cm)
$NiFe_2O_4$	457	~109.7	80	1.90
$Ni_{0.7}Mg_{0.3}Fe_2O_4$	437	~69.1	80	2.53
$Ni_{0.4}Mg_{0.6}Fe_2O_4$	402	~41.3	90	3.3
$Ni_{0.1}Mg_{0.9}Fe_2O_4$	482	~17.1	52	0.43

1.4.2 Amorphous Ni/Fe/X Oxides

Macagno[19] first examined the effect on OER of adding Mn to an electrode prepared via layer-by-layer coprecipitation. Unfortunately, either no improvement or a detrimental effect was observed, depending on the exact preparation of the electrode.

Recently, Berlinguette et. al[20] applied the photochemical metal-organic deposition method (PMOD)[21] to the synthesis of thin-film mixed metal oxides. PMOD relies on the use of metal complexes with hydrophobic ligands that can be decomposed via photolysis. While access to appropriate metal complexes is not always possible and may require additional synthetic effort, PMOD nonetheless offers an easy way to controllably vary the identity of metal dopant and stoichiometry, while avoiding lattice constraints of crystalline oxides. In a PMOD synthesis, a premixed metal solution is first spin-coated onto the desired electrode substrate, followed by >24 hours of photolysis. The resulting film is then annealed at 100 °C for 1 hour to remove any residual ligands and improve adhesion to the substrate. The authors successfully demonstrated the synthesis

of compositionally and morphologically homogenous mixed metal oxide films and assessed catalyst performance using several different parameters (Figure 1-6).

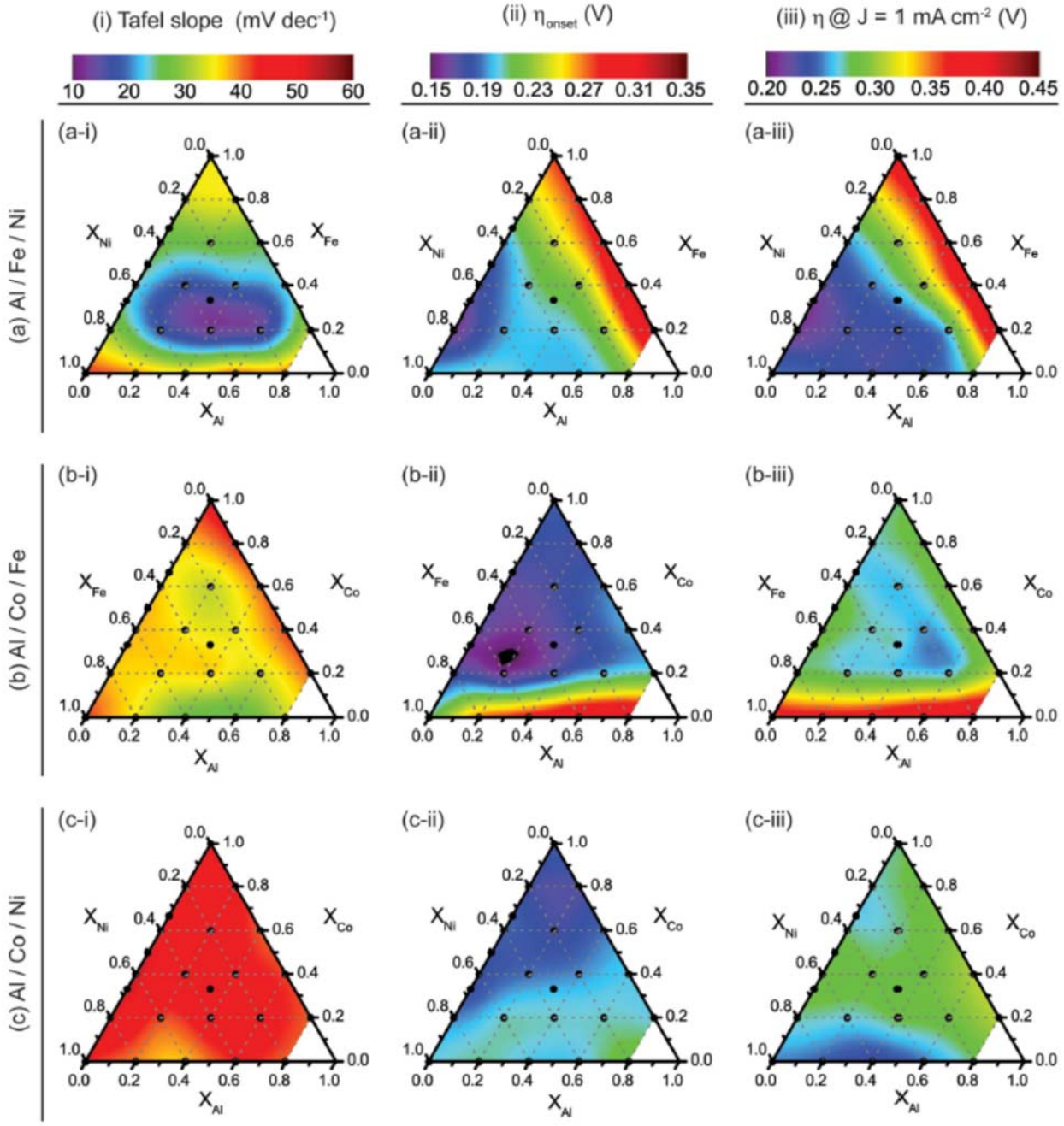

Figure 1-6. Contour plots of Tafel slope, η_{onset}, and η @ J=1 mA/cm^2 of the three triads examined by Berlinguette et al. Image taken from reference 20c.

Overall, the binary $Ni_{0.8}Fe_{0.2}$ oxide remains the most active OER catalyst with the lowest η_{onset}, and η @ J=1 mA/cm^2. Triads containing Co were found to generally have lower η_{onset} but exhibited higher Tafel slopes and η @ J=1 mA/cm^2. Aluminum appeared to combine most favorably with Ni and Fe, exhibiting not only relatively low η_{onset}, and η @ J=1 mA/cm^2, but also unprecedentedly low Tafel slopes of <20 mV/dec, with $Ni_{0.4}Fe_{0.2}Al_{0.4}$ being the lowest at 11 mV/dec. Materials with low Tafel slopes are desirable in devices that operate at high current densities; however, stability is also crucial. Prolonged electrolysis of $Ni_{0.4}Fe_{0.2}Al_{0.4}$ in 0.1 M KOH showed a 1.2% decrease in current density per hour, accompanied by the leaching of Al ions that plateaued at ~50%. This leaching phenomenon is not surprising given the known solubility of Al under alkaline conditions. However, that the leaching stops at 50% under the conditions tested suggest that Al is not simply leaching to create higher surface area material. This is also supported by measuring Tafel slope after the leaching test, which only increased slightly to ~15 mV/dec.

1.5 Mechanistic Investigations of NiFe-LDH Electrocatalysts

Among the different types of NiFe oxide electrocatalysts, NiFe-LDH has been the most extensively studied because this structure is highly suitable for catalysis. The thin-plate morphology readily give rise to material with high surface area, and the layered structure allows substrate water to easily come in contact with the metal active sites. The LDH structure also has the unique ability to easily accommodate highly oxidized metal centers via anions intercalation between the layers (i.e. swelling). Furthermore, the intercalation process requires minimal structural rearrangement, thus reducing the kinetic barrier to the reaction.

A number of *in situ* studies employing various techniques have been performed in efforts to better understand how Fe improves the activity of NiFe electrocatalysts. However, it was not until

recently that these types of studies were done under truly steady-state catalytic conditions (i.e. *in operando*). One reason that steady-state conditions was avoided was to prevent complications that can result from bubble formation during turnover. Instead, *in situ* experiments were carried out where a CV scan is first swept to a potential where OER takes place, followed by reversal back to a potential more anodic than $Ni^{+2}/Ni^{+3/+4}$ redox feature but insufficient for OER. Secondly, much of research has focused on using these materials as battery cathodes, and in these cases, OER conditions were purposely avoided. In the following discussion, "*in situ*" studies are those where steady-state OER is not taking place, while "*in operando*" studies refer to those done under steady-state catalytic conditions.

1.5.1 X-ray Absorption Spectroscopic Studies (XAS)

While good agreement exist between different studies regarding the spectroscopic changes that take place upon oxidation in the Ni K-edge XAS data, no consensus has been reached for the changes that take place in the Fe K-edge data.

Recently, Bell and coworkers reported the first *in operando* XAS investigation of NiFe-LDH electrocatalysts over a range of Fe dopant concentrations performed under steady-state OER conditions.[22] Changes observed in the Ni K-edge near edge (XANES) and extended fine structure (EXAFS) spectra upon oxidation were both consistent with the formation of a γ-NiOOH lattice. A small increase in the edge energy was observed in the Fe K-edge XANES spectra recorded during OER, while EXAFS analysis showed a contraction of Fe-O distance of from 2.00 Å to 1.90 Å, similar to the Fe^{+4}-O distance in $SrFeO_3$. The authors believed that the edge energy shift was too small to signify the presence of Fe^{+4} species and can be explained by the destabilization of the Fe-4p valence orbital resulting from bond contraction. The unusually short Fe^{+3}-O bond observed was attributed to structural imposition from the surrounding oxidized $[NiO_6]$ octahedra. Additionally,

using site-specific overpotentials calculated from the DFT+U methodology, Fe^{+3} sites within a matrix of γ-NiOOH were found to exhibit the lowest overpotential, leading the authors to propose Fe^{+3} as the catalytically relevant oxidation site for OER.

Interestingly, the experimental results of Bell and coworkers are very similar to results obtained earlier by Balasubramanian et al.,[23] even though this earlier *in situ* XAS study was not done under steady-state OER conditions. However, a different interpretation of experimental results were presented by Balasubramanian and coworkers. They concluded that Fe exists as Fe^{+4} in the oxidized NiFe-LDH catalyst and the observed small energy shift is a result of the high degree of covalency of the Fe^{+4}-O bond (i.e. electron-rich Fe^{+4}).

In addition to differences in the interpretation of experimental results, the earliest *in situ* XAS study of Scherson and co-workers[24] reported no change in the Fe K-edge XANES spectrum for the oxidized catalyst. However, EXAFS analysis also showed an Fe^{+3}-O distance of 1.92±0.02 Å in both the oxidized and reduced catalysts. While bond contraction is possible for Fe^{+3}-O in a highly oxidized γ-NiOOH lattice, it is puzzling that such a short Fe^{+3}-O bond length is also observed when the γ-NiOOH lattice has been reduced. The issue was not addressed and author concluded that Fe remains Fe^{+3} which substitutes into the α-$Ni(OH)_2$/γ-NiOOH lattice without observable structural perturbation.

1.5.2 Mössbauer Spectroscopic Studies

Parallel *in situ* Mössbauer studies were performed by Corrigan et al.[25] under conditions identical to the Scherson XAS study. The spectrum of the oxidized catalyst consisted of a singlet with an isomer shift (IS) of 0.22 mm/s, while the reduced catalyst exhibited a doublet with an IS of 0.35 mm/s and quadrupole splitting (QS) of 0.44 mm/s. An IS of 0.22 mm/s is not consistent with reported IS values for a true Fe^{+4} species (around 0 mm/s or less), thus this species is best

described as an electron-deficient Fe^{+3} species. Nonetheless, this result is consistent with the in-situ XAS results obtained by Scherson, where no change was observed in the Fe K-edge XANES spectrum upon oxidation.

In related studies, Delmas[26] and Glemser[27] both undertook *in situ* Mössbauer investigations of NiFe-LDH under constant-current charge/discharge conditions in highly alkaline KOH electrolyte. The precise potential experienced by the NiFe-LDH in studies is unclear, but their focus on stabilizing Ni/Cd batteries through Fe-doping suggest that OER conditions were avoided. While a doublet with nearly identical Mössbauer parameters was reported for the discharged electrodes (i.e. reduced) by both groups, these authors observed an Fe^{+4} species with isomer shift of either 0 mm/s (doublet) or -0.19 mm/s (singlet), depending on method of fitting chosen by the respective authors. Although material preparation and electrolyte pH were quite different for these latter two studies, they do demonstrate that an Fe^{+4} species is obtainable in NiFe-LDH. Furthermore, the Pourbaix diagram of Fe predicts both the existence of Fe^{+3} and Fe^{+4} under OER conditions,[28] thus a true *in operando* Mössbauer study of NiFe-LDH would be very enlightening.

1.5.3 Other *In situ* Studies

Bell and co-workers performed *in operando* Raman spectroscopic investigations of electrodeposited NiFe-LDH over a range of Fe concentrations.[11] At open-circuit potential, the Ni-O vibrational bands could be assigned to those of α-$Ni(OH)_2$, and the Fe-O band resembled either α-FeOOH or Fe_2O_3. Upon oxidation, the Ni-O stretch resembled that of γ-NiOOH, consistent with results from XAS studies. However, signal interference from the high Raman cross section of γ-NiOOH, as well as the existence of many structurally similar Fe oxyhydroxide phases, made the precise assignment of the Fe-O bands impossible.

Boettcher et al. examined the conductivity of NiFe-LDH as a function of applied potential and Fe concentration using an interdigitated array (IDA) electrode. For all NiFe-LDH catalysts examined, conductivity of the film increases dramatically as soon as Ni^{+2} becomes oxidized, demonstrating that NiOOH is more conductive than $Ni(OH)_2$. However, this 30-60 fold increase in conductivity was insufficient to explain the improvement in activity between a 25% Fe LDH and the Ni-only LDH. Additionally, they also demonstrated that the electron-deficient Fe^{+3} induces partial electron transfer from $Ni^{+3/+4}$ by examining the turnover frequency (TOF) as a function of film thickness. This electron-withdrawing effect can also explain why while Ni^{+2} becomes more difficult to oxidize in the presence of Fe. The resulting $Ni^{+3/+4}$ species is able to oxidize water more efficiently.

1.6 Thesis Overview

The original research presented in this thesis describes two approaches to addressing the challenge faced in making the oxygen evolution reaction more efficient. The first approach focused on the development of a high throughput combinatorial screening method that directly detects the product of water oxidation, followed by the characterization of "hit" catalysts. My work consisted of the optimization of a prototype screening apparatus and associated experimental protocol, including electrode array preparation, determination of screening metrics, analysis of screening results, and validation of "hit" compositions via standard electrochemical techniques. From the initial screening of 216 distinct oxide compositions, it was observed that the incorporation of a third metal into Ni-Fe binary oxides often enhanced OER activity, with Ni-Fe-Al amorphous oxide showing the highest activity (Chapter 2). This discovery led to the synthesis of a well-defined $NiFeAlO_4$ inverse spinel oxide and its subsequent application in OER. Comparisons of the electrochemical activities for compositionally and structurally relevant oxides, including known

OER catalysts NiO, $Ni_9Fe_1O_x$, and $NiFe_2O_4$ established $NiFeAlO_4$ as a superior electrocatalyst with no Al leaching (Chapter 3).

The second approach focused on understanding the origin of the high activity in the best OER electrocatalysts. Combinatorial screening efforts from our group have examined thousands of trimetallic oxides, the most active of which consist of Ni-Fe-X combinations. In order to begin probing the mechanistic basis for the effect of the third metal, we first sought a better understanding of the simpler Ni-Fe oxide catalysts. An *in operando* Mössbauer study was carried out in order to compare Fe speciation between 25% Fe NiFe-LDH and the 100% hydrous Fe oxide electrocatalyst under steady-state catalysis. A new synthetic method was developed by which the catalysts can be directly grown onto a carbon paper electrode, and an *in operando* Mössbauer-electrochemical cell was constructed. An Fe^{+4} species was observed in the 25% Fe catalyst during steady-state catalysis but not in the 100% Fe catalyst. The stability of this Fe^{+4} species induced by the γ-NiOOH lattice suggests that it is not the site of catalysis but it might help to increase the oxidizing ability of the true active site (Chapter 4).

---

1. Umena, Y.; Kawakami, K.; Shen, J. R.; Kamiya, N. *Nature* **2011,** *473,* 55-60.
2. McEvoy, J. P.; Brudvig, G. W. "Water-Splitting Chemistry of Photosystem II." *Chem. Rev.* **2006,** *106,* 4455-83.
3. Kinoshita, K. *Electrochemical Oxygen Technology*; Wiley−Interscience: New York, 1992; Chapt 2.
4. (a) Dinca, M.; Surendranath, Y.; Nocera, D. G. *Proc. Nat. Acad. Sci. USA* **2010**, *107*, 10337-10341; (b) Bediako, D. K.; Lassalle-Kaiser, B.; Surendranath, Y.; Yano, J.; Yachandra, V. K.;

Nocera, D. G. *J. Am. Chem. Soc.* **2012**, *134*, 6801-6809; (c) Bediako, D. K.; Surendranath, Y.; Nocera, D. G. *J. Am. Chem. Soc.* **2013**, *135*, 3662-3674.

5. Chen, Y. W. D.; Noufi, R. N. *J. Electrochem. Soc.* **1984**, *131*, 1447-1451.
6. Smith, A. M.; Trotochaud, L.; Burke, M. S.; Boettcher, S. W. *Chem. Commun.* **2015**, *51*, 5261-5263.
7. (a) Trotochaud, L.; Young, S. L.; Ranney, J. K.; Boettcher, S. W. *J. Am. Chem. Soc.* **2014**, *136*, 6744-6753. (b) Corrigan, D. A. *J. Electrochem. Soc.* **1987**, *134*, 377-384.
8. (a) Tichenor, R. L. *Ind. Eng. Chem.***1952**, *44*, 973–977; (b) Foerster, F.; Piguet, A. On the understanding of anodic formation of oxygen. *Z. Angew. Phys. Chem.* **1904**, *10*, 714–721; (c) Seiger, H. N.; Shair, R. C. Oxygen evolution from heavily doped nickel oxide electrodes. *J. Electrochem. Soc.* **1961**, *108*, C163. (d) Falk, S. U.; Salkind, A. J. "Alkaline Storage Batteries," John Wiley & Sons, Inc., New York, 1969; (e) Munshi, M. Z. A.; Tseung, A. C. C.; Parker, J. *J. Appl. Electrochem.* **1985**, *15*, 711-717. (f) Troilious, G., Alfelt, G. *J. Power Sources* **1966**, *22*, 337; (g) Mlynarek, G.; Paszkiewicz, M.; Radniecka, A. *J. Appl. Electrochem.* **1984**, *14*, 145-149.
9. (a) Orehotsky, J.; Huang, H.; Davidson, C. R.; Srinivasan, S. *J. Electroanal. Chem.* **1979**, *95*, 233-235; (b) Iwakura, C.; Nishioka, M.; Tamura, H. *Nippon Kagaku Kaishi* **1982**, 1294-1298; (c) Singh, N. K.; Singh, R. N. *Indian J. Chem., Sect A* **1999**, *38*, 491-495; (d) Hong, D.; Yamada, Y.; Nagatomi, T.; Takai, Y.; Fukuzumi, S. *J. Am. Chem. Soc.* **2012**, *134*, 19572-19575.
10. Córdoba, S. I.; Carbonio, R. E.; Teijelo, M. L.; Macagno, V. A. *Electrochim. Acta* **1987**, *32*, 749-755.
11. Louie, M. W.; Bell, A. T. *J. Am. Chem. Soc.* **2013**, *135*, 12329-12337.

12. Landon, J.; Demeter, E.; İnoğlu, N.; Keturakis, C.; Wachs, I. E.; Vasić, R.; Frenkel, A. I.; Kitchin, J. R. *ACS Catal.* **2012**, *2*, 1793-1801.

13. Gong, M.; Li, Y.; Wang, H.; Liang, Y.; Wu, J. Z.; Zhou, J.; Wang, J.; Regier, T.; Wei, F.; Dai, H. *J. Am. Chem. Soc.* **2013**, *135*, 8452-8455.

14. Song, F.; Hu, X. *Nat Commun* **2014**, *5*.

15. Liang, H. F.; Meng, F.; Caban-Acevedo, M.; Li, L. S.; Forticaux, A.; Xiu, L. C.; Wang, Z. C.; Jin, S. *Nano Lett* **2015**, *15*, 1421-1427.

16. (a) Singh, R. N.; Singh, N. K.; Singh, J. P. *Electrochim. Acta* **2002**, *47*, 3873-3879; (b) Singh, R. N.; Singh, J. P.; Cong, H. N.; Chartier, P. *Int. J. Hydrogen Energy* **2006**, *31*, 1372-1378.

17. Anindita; Singh, A.; Singh, R. N. *Int. J. Hydrogen Energy* **2010**, *35*, 3243-3248.

18. Kumar, M.; Awasthi, R.; Sinha, A. S. K.; Singh, R. N. *Int. J. Hydrogen Energy* **2011**, *36*, 8831-8838.

19. Cordoba, S. I.; Teijelo, M. L.; Macagno, V. A. *Electrochim. Acta* **1987**, *32*, 1783-1786.

20. (a) Smith, R. D. L.; Prevot, M. S.; Fagan, R. D.; Zhang, Z. P.; Sedach, P. A.; Siu, M. K. J.; Trudel, S.; Berlinguette, C. P. *Science* **2013**, *340*, 60-63; (b) Smith, R. D. L.; Prévot, M. S.; Fagan, R. D.; Trudel, S.; Berlinguette, C. P. *J. Am. Chem. Soc.* **2013**, *135*, 11580-11586; (c) Zhang, C. J.; Fagan, R. D.; Smith, R. D. L.; Moore, S. A.; Berlinguette, C. P.; Trudel, S. *J Mater Chem A* **2015**, *3*, 756-761.

21. Avey, A. A.; Hill, R. H. *J Am Chem Soc* **1996**, *118*, 237-238.

22. Friebel, D.; Louie, M. W.; Bajdich, M.; Sanwald, K. E.; Cai, Y.; Wise, A. M.; Cheng, M. J.; Sokaras, D.; Weng, T. C.; Alonso-Mori, R.; Davis, R. C.; Bargar, J. R.; Norskov, J. K.; Nilsson, A.; Bell, A. T. *J. Am. Chem. Soc.* **2015**, *137*, 1305-1313

23. Balasubramanian, M.; Melendres, C. A.; Mini, S. *J. Phys. Chem. B* **2000**, *104*, 4300-4306.

24. Kim, S. H.; Tryk, D. A.; Antonio, M. R.; Carr, R.; Scherson, D. *J. Phys. Chem.* **1994**, *98*, 10269-10276.

25. Corrigan, D. A.; Conell, R. S.; Fierro, C.; Scherson, D. A. *J. Electrochem. Soc.* **1987**, *134*, C131-C131.

26. (a) Demourguesguerlou, L.; Fournes, L.; Delmas, C. *J. Sol. St. Chem.* **1995**, *114*, 6-14; (b) Guerlou-Demourgues, L.; Fournes, L.; Delmas, C. *J. Electrochem. Soc.* **1996**, *143*, 3083-3088.

27. (a) Axmann, P.; Erdbrügger, C. F.; Buss, D. H.; Glemser, O. *Angew Chem Int Edit* **1996**, *35*, 1115-1118; (b) Axmann, P.; Glemser, O. *J. Alloys Compd.* **1997**, *246*, 232-241.

28. Schweitzer, G. K.; Pesterfield, L. L. *The Aqueous Chemistry of The Elements*; Oxford University Press: Oxford, 2010.

Chapter II

Development of an O_2-Sensitive Fluorescence Quenching Screening Assay

This work was published:

Gerken, J. B., Chen, J. Y. C., Massé, R. C., Powell, A. B., Stahl S. S., *Angew. Chem. Int. Ed*. **2012**, 51, 1-7

2.1 Introduction

Valuable progress has been made in understanding the mechanism of electrocatalysts for water oxidation;[1-5] however, the rational design of optimal catalysts is still infeasible. The number of possible combinations of metal cations, even those with well-defined metal stoichiometry, far exceeds the number that can be tested in a traditional sequential fashion. Consequently, recent efforts have focused on combinatorial or array-based methods to discover new electrocatalysts. For example, a soluble fluorescent pH-indicator has been used to screen electrocatalyst activity for reactions that consume or generate protons,[6] and this technique has been employed to assess platinum-group-metal electrocatalysts for water oxidation.[7] These studies highlight the appeal of fluorescence as a rapid detection method for electrocatalytic activity, but the method is constrained by the pKa of the fluorescent indicator, the need to use poorly buffered electrolytes to ensure sensitivity to pH changes, and the fact that organic fluorescent pH indicators can degrade rapidly under water-oxidation conditions, potentially leading to spurious results. In another approach, several groups have used combinatorial methods to probe the photoelectrocatalytic performance of mixed metal oxide materials. In most of these assays, the oxides are required to act simultaneously as a light-harvesting semiconductor and as the electrocatalyst for one or both water-splitting half-reactions.[8-13] It seems unlikely, however, that nature will provide a single inorganic material that exhibits multiple orthogonal optimal properties. Recognizing that the most efficient PEC cells are likely to integrate separate photovoltaic and catalytic materials,[14-17] we targeted the development of an assay that would enable rapid assessment of electrocatalysts for water oxidation independent of the other PEC cell functions.

The *sine qua non* of electrocatalytic water oxidation is the production of O_2, and an ideal catalyst screening assay would monitor O_2 evolution directly. As noted above, fluorescence-based

techniques benefit from high sensitivity and efficiency relative to many other analytic techniques; enable parallel, rather than serial, analysis of activity; and can avoid the need for costly specialized analytical instrumentation.

Fluorescent "pressure sensitive paints" are ideally suited for use in the analysis of O_2-evolving electrocatalysts. These paints are used in the automobile and aerospace industries to study aerodynamics in wind tunnels, and their utility arises from the sensitivity of their fluorescence intensity to the partial pressure of O_2 (pO_2).[18] Quantitative measurements are improved through the use of a paint containing two fluorophores, one of which is insensitive to O_2 and serves as a background reference, and another that exhibits fluorescence quenching in proportion to the pO_2. Our assay takes advantage of a commercially available dual-chromophore paint that exhibits O_2-insensitive green and O_2-sensitive red fluorescence.

2.2 Results and Discussion

A schematic representation of the electrochemical cell is depicted in Figure 2-1. The key components of the cell are a fluorine-doped tin oxide (FTO) electrode with an array of prospective metal-oxide electrocatalysts and a stainless steel mesh coated with fluorescent paint. These components are aligned in parallel layers, separated by a thin (1 mm) spacer, and immersed in the electrolyte (0.1 M NaOH). The three-electrode cell is then sealed, purged with N_2, and electrolyzed at 670 mV vs. Ag/AgCl [overpotential (η) = 406 mV]. During electrolysis, the cell is irradiated at specified time intervals with 400 nm light, and the green and red fluorescence emanating from the painted mesh is captured using a digital camera. Because the red fluorescence signal is quenched by O_2, analysis of the red/green fluorescence-intensity ratios provides the basis for monitoring the water-oxidation activity of individual catalysts.

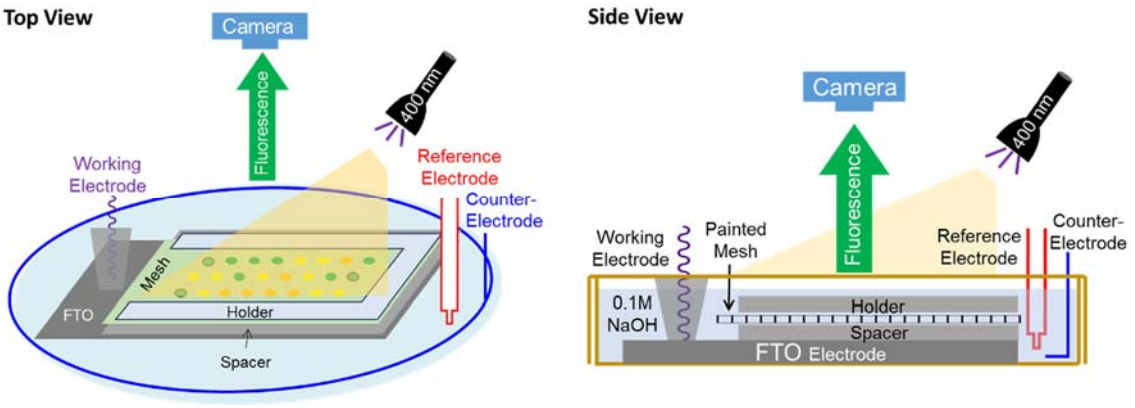

Figure 2-1. Schematic drawing of the electrochemical cell showing the positions of the electrode array, O_2-sensing mesh, light source, and camera.

The selection of prospective electrocatalysts emphasized metals from among the first-row transition series, which are sufficiently abundant in the earth's crust to ensure their viability in large-scale applications. Mixed oxides of these metals in well-defined stoichiometry (e.g. $NiCo_2O_4$, etc.) have been investigated, as have nonstoichiometric binary and ternary mixed oxides,[19-23] but the diversity space is far from well explored. Mid-to-late first-row transition metals provide excellent capacity to access multiple oxidation states, and different redox-active metals in the catalytic material could play synergistic roles in buffering the multi-electron processes needed to achieve efficient water oxidation. The role of a Ca^{2+} ion in the oxygen-evolving complex of Photosystem II[24,25] suggested to us that incorporation of non-redox-active metal ions (e.g., Ca^{2+}, Mg^{2+}, Al^{3+}) could have a beneficial structural role in the oxide material or serve as a Lewis acidic site to facilitate deprotonation of a reactive water molecule and/or formation of the O–O bond, which is often rate-limiting.[1,2,19]

Twenty-one different ternary metal-oxide combinations (Table. 2-1) were screened. For each triad, solutions of the corresponding metal salts were mixed in stoichiometries of $A_{(100\%-x)}:B_{(x-y)}:C_y$, with x and y varied in units of 20% from 0 to 100%, in order to sample across the ternary composition diagram (Figure 2-2a). These mixtures were then arrayed onto an FTO-coated glass

electrode (Figure 2-2b) and calcined at 500 °C. The arrays were then electrolysed and assayed for oxygen evolution as described above.

Table 2-1. List of metal triads investigated in this study

Metal-Ion Triads Tested (M1-M2-M3)						
Co-Al-Fe	Co-Fe-Mn	Co-Ce-Fe	Co-La-Al	Ni-Fe-Cr	Ni-Ca-Fe	Ni-Ce-Al
Co-Al-Ni	Co-Fe-Cr	Co-La-Ca	Ni-Al-Fe	Ni-Ce-Fe	Ni-Mg-Fe	Ni-La-Al
Co-Fe-Ni	Co-La-Fe	Co-Ce-Al	Ni-Fe-Mn	Ni-Al-Cr	Ni-Zn-Fe	Ni-La-Fe

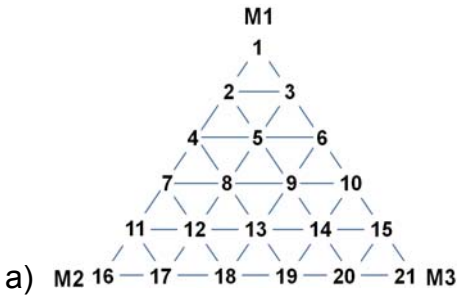

a)

b)

	R	1	2	3	4	5	6	7
	8	9	10	11	12	13	14	**R**
	R	15	16	17	18	19	20	21

R = Reference Oxide

Figure 2-2. a) Ternary-oxide composition diagram, spot 1 is 100% M1, spot 5 is 60% M1, 20% M2, 20% M3, etc. b) Arrangement of metal-oxide compositions on the electrode array; R reflects reference metal-oxide compositions held constant from electrode to electrode

Cobalt and nickel oxides have been widely studied as water-oxidation electrocatalysts,[1,3,19,26,27] and analysis of screening data for the Co-Al-Ni triad will be used to illustrate the assay methodology. Catalytic O_2 evolution manifests itself as a quenching of the red fluorescence signal, and photographs obtained during electrolysis reveal green spots over some of the electrocatalyst positions (Figure 2-3a). Image processing enables red and green channels to be separated within the photographs (see Experimental Section), and the red/green intensity ratios from each photograph were summed and background corrected to create a single greyscale image in which the integrated spot intensities correlate with the amount of O_2 produced from individual electrocatalysts (Figure 2-3b).[28] These intensities were normalized with respect to reference spots

in the array and plotted as a false-colour map on a ternary composition diagram for the triad (Figure 2-3c).

A noteworthy result from the Co-Al-Ni triad data is the effect of the redox-inert, Lewis-acidic Al^{3+} ion on electrocatalytic activity. As shown in Figure 2-3c, the $Co_{20}Al_{20}Ni_{60}$ oxide composition exhibits higher activity than the monometallic Co and Ni oxides, as well as Co-Ni binary oxides, which have been used extensively in water electrolysis applications.[1,19,26,27,29]

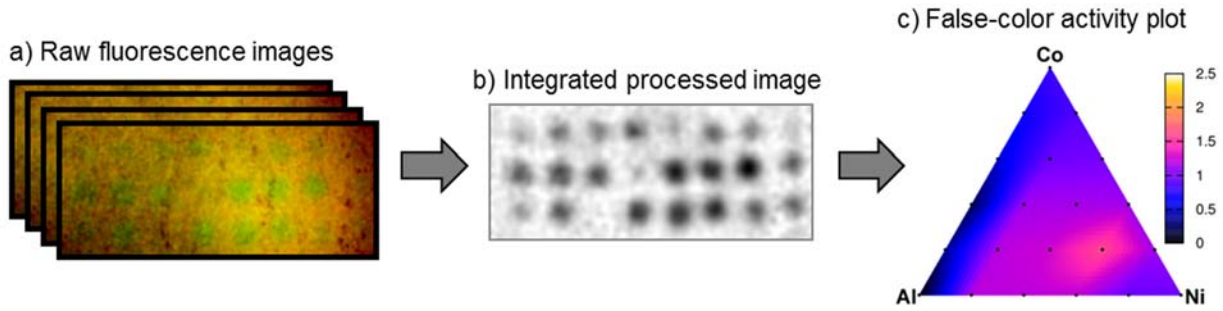

Figure 2-3. a) Stacked raw images of the fluorescent grid above a Co-Al-Ni array during electrolysis (contrast-enhanced for clarity). b) Background-subtracted greyscale image of the sum of the red/green processed images from the stack depicted in a). c) False color ternary composition diagram of the Co-Al-Ni triad data (average of 3 experiments) showing normalized activities with an optimum at $Co_{20}Al_{20}Ni_{60}O_x$.

Analogous fluorescence-based activity data were acquired for each of the other twenty triads identified in Table 2-1 (cf. Figs. 2-9). Relative activities obtained from the screening data roughly correlate with the limited literature data available for similar binary and ternary mixtures. For example, interpolation between the assayed Co-Fe-Ni, Co-Fe-Mn, and Co-Fe-Cr points give composition/activity trends that match those previously reported.[20,22] Oxides with lanthanide admixtures are consistent under-performers; we suspect the poor activity of these triads relative to previously reported activity[4,5,19,29] arises from the calcination temperature-limit imposed by the FTO-on-glass electrode[8] (see Supplementary Information). The highest electrocatalytic activity was detected from combinations of Ni, Fe and a redox-inert metal ion, in particular, $Ni_{60}Al_{20}Fe_{20}O_x$ and $Ni_{40}Al_{40}Fe_{20}O_x$ (Figure 2-4). These observations have important implications for solar fuel

formation in light of a previously reported photoelectrochemical cell with a binary Ni-Fe oxide electrocatalyst, $Ni_{80}Fe_{20}O_x$, that achieved solar-to-hydrogen conversion efficiencies as high as 7.8%.[14] The improved activity observed upon incorporation of Al^{3+} into the Ni-Fe oxide material further demonstrates the beneficial effect of redox-inert metal ions on water-oxidation electrocatalyst activity. The relative activities of different spots in the arrays were reproducible across multiple runs and replicated samples, as revealed by the similar activities of independently tested Ni-Fe binary mixtures from the Ni-Fe-Al and Ni-Ca-Fe triads (cf. the shared edge from these triads in Figure 2-5).

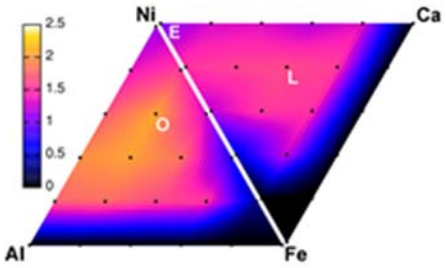

Figure 2-4. Activity vs. composition plot for the Ni-Fe-Al and Ni-Ca-Fe triads, with labels identifying compositions investigated by steady-state Tafel analysis. L: $Co_{60}Al_{20}Fe_{20}$, O: $Ni_{20}Al_{60}Fe_{20}$

In order to further validate the results of the fluorescence assays, 15 of the 441 oxide compositions tested were selected for further investigation by steady-state Tafel analysis (Figs. 2-5a and 2-10). A close correlation was observed between the relative catalytic activities obtained from the fluorescence assay and steady-state current densities at a constant overpotential from the Tafel analysis (Figure 2-5b). These results clearly demonstrate that the fluorescence-based data are an excellent predictor of electrocatalyst performance.

The merits of this electrochemical assay may be compared to previous photoelectrochemical screening studies wherein similar metal-oxide materials served as a photovoltaic semiconductor and as an electrocatalyst. For example, oxide compositions within the Co-Al-Fe triad exhibited no

anodic activity in a photoelectrochemical screen,[9] but they show respectable oxygen-evolving activity in the present screen (cf. Figure 2-9). Observations such as these underscore the need to measure directly the property that one wishes to optimise via screening because good photovoltaic materials are not necessarily good water oxidation catalysts and vice-versa.

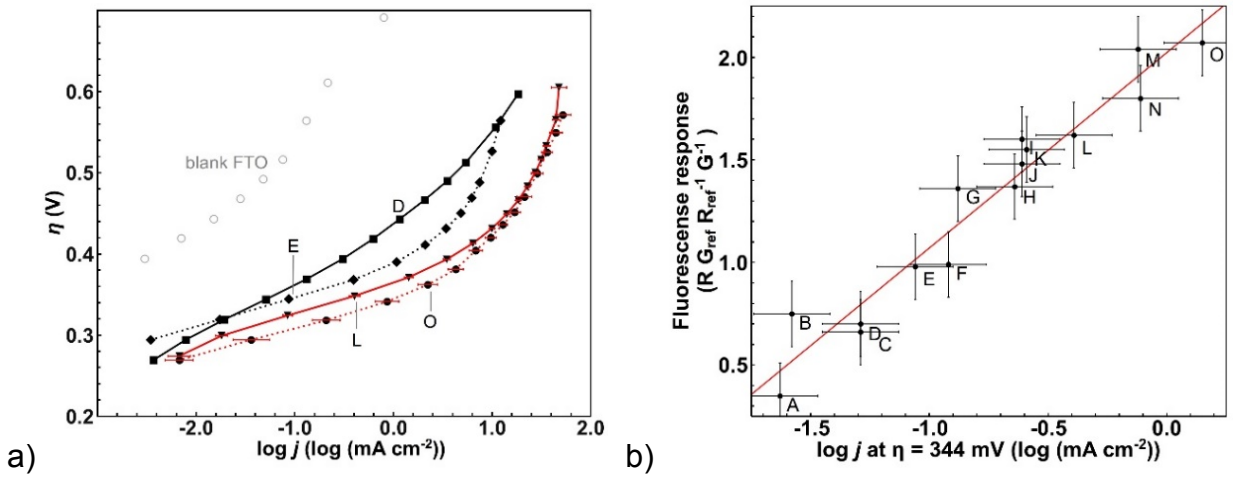

Figure 2-5. a) Representative Tafel current/polarization data for selected catalyst compositions identified from the fluorescence-quenching assays. X-axis error bars reflect one standard deviation based on multiple, independently prepared samples. b) Correlation of catalyst activity derived from the fluorescence-quenching assays and steady-state Tafel data. Error bars reflect one standard deviation based on multiple, independently prepared samples (linear fit R^2 = 0.94). Compositions tested: A: Ni_{100}, B: $Ni_{40}Ca_{40}Fe_{20}$, C: $Ni_{60}Al_{20}Fe_{20}$, D: Co_{100}, E: $Co_{40}Fe_{40}Cr_{20}$, F: $Co_{40}Fe_{20}Mn_{40}$, G: $Co_{20}Fe_{40}Mn_{40}$, H: $Co_{20}Fe_{20}Cr_{60}$, I: $Co_{20}Fe_{20}Ni_{60}$, J: $Co_{60}Al_{20}Fe_{20}$, K: $Co_{20}Al_{20}Ni_{60}$, L: $Co_{60}Al_{20}Fe_{20}$, M: $Ni_{20}Ca_{60}Fe_{20}$, N: $Ni_{40}Al_{40}Fe_{20}$, O: $Ni_{20}Al_{60}Fe_{20}$

2.3 Conclusion

Overall, the results presented above demonstrate an efficient and effective fluorescence-based assay for discovery of new oxygen-evolving electrocatalysts. The data acquired in this initial work suggest redox-inert Lewis-acidic metal ions can be effective promoters of electrocatalytic activity of mixed-metal oxides, possibly resembling the role of Ca^{2+} in biological oxygen evolution.[24,25] Earth-abundant Lewis-acidic metal ions, such as Al^{3+}, represent appealing, economical alternatives to La^{3+} and other rare-earth elements commonly featured in heterogeneous water oxidation catalysts.[4,5,29] Primary screening methods of the type described here are critical to the identification

of promising catalytic materials worthy of more-systematic investigation and optimization, and they will play an important role in the development of practical and efficient photoelectrochemical devices for solar energy storage.

2.4 Experimental Details

2.4.1 General Experimental Conditions and Apparatus

Unless otherwise noted, all chemicals used were obtained from Sigma-Aldrich and used without further purification. All aqueous solutions were prepared from purified water (ThermoFisher-Scientific Nanopure, 18.2 $M\Omega cm^{-1}$). All metal solutions were prepared from their respective nitrate salts, except for chromium where $CrCl_3$ was used.

The paint used for O_2-sensing is the "Binary Unicoat Pressure Sensitive Paint" purchased from Innovative Science Solution Inc. Commercially available LED UV flashlights were obtained with approximately 400 nm output.[30]

Electrochemical experiments were conducted using the Bioanalytical System EC Epsilon potentiostat with three-component electrochemical cells. Fluorine-doped tin oxide (FTO) coated glass (Hartford Tec Glass Co. Inc.) and Ag/AgCl electrodes were used as the working and reference electrode, respectively, in all experiments. Nickel and platinum wires were used as the counter electrode in the mixed-metal oxide screening and Tafel experiments, respectively.

2.4.1.1 The Electrochemical Cell

Three 0.5-cm diameter holes were drilled on the cover of a 15-cm diameter glass petri dish and fitted with septa. The septa-fitted holes allowed the insertion of the working, reference, and counter electrodes, as well as easy purging of the electrochemical cell. The base of the petri dish contains the electrolyte solution, the oxide-spotted working electrode, and the painted stainless steel mesh, with various plastic holders and spacer (Figure 2-6).

Figure 2-6. Electrochemical cell used in this screening study

2.4.1.2 The O_2-Senseing Paint-covered Mesh

A piece of 100 mesh stainless-steel mesh is required for sufficient O_2 diffusion and ionic conductivity as well as image processing (coarser mesh resulted in the appearance of moiré patterns in the images acquired that prevented image processing). A 5 cm x 8 cm piece of mesh is used. Optimal paint coverage is achieved by holding the nozzle about 45 cm away from the mesh and spray-painting between twenty to twenty-five times. The painted mesh should remain largely see-through without significant clogging. Evenness of the painted mesh can be checked by performing an experiment using a FTO slide that is spotted with only the internal reference. The mesh should be re-painted after about fifteen experiments, or when the spots are no longer easily distinguished from the background. The old paint can be stripped off by sonicating the mesh in acetone for at least thirty minutes.

2.4.2 Sample Preparation and Calcination

An array of individual mixed-oxide spots on the FTO electrode were deposited from premixed metal solutions as shown in Scheme 2-1. Aliquots of 5 mM aqueous metal salt solutions containing 9 vol % glycerol were mixed in ratios as shown in Table 2-2. Subsequently, one 0.5 µl drop of

each mixture was deposited onto a FTO (7.5 cm x 2.5 cm) electrode using the template as shown in Figure 2-7, where R stands for the CoFeNi (4:4:2) internal reference. This composition was selected as the reference because it was found to reach steady-state more rapidly than pure Ni or Co oxides and maintained a consistent level of activity over prolonged electrolysis. Each electrode contained twenty-one unique spots and three internal reference spots. After allowing the deposits to dry on a hotplate, the coated electrodes were calcined in an electric kiln at 500 °C for 6 hours. This temperature was selected because it is the maximum that the glass substrate of the FTO electrode can withstand without undergoing distortion that would destroy the continuity of the FTO conductive layer. This limitation suggests that alternative substrates must be used to properly screen certain mixed oxides, such as those incorporating lanthanides, that require higher-temperature calcination to sinter.[31,32]

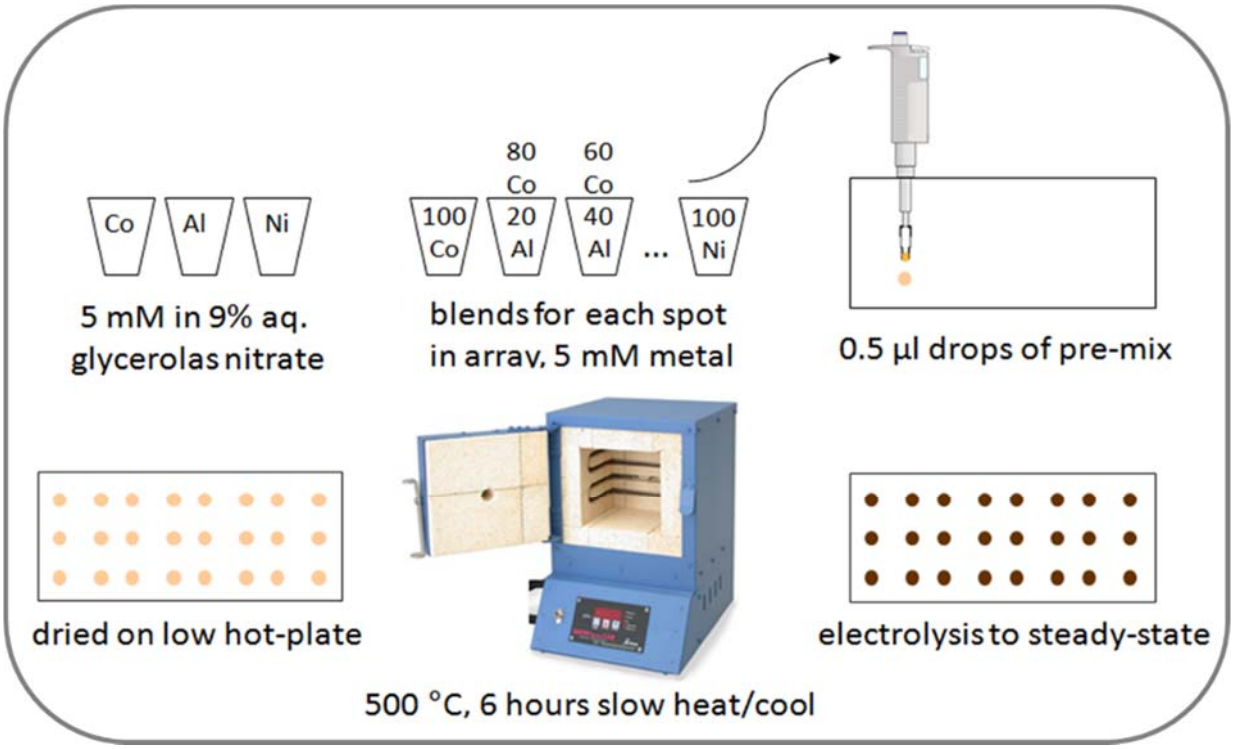

Scheme 2-1. Catalyst array preparation workflow

Table 2-2. Composition of metals A, B, and C of each of the 21 spots on the FTO anode

Spot #	A	B	C	Spot #	A	B	C	Spot #	A	B	C
1	100	-	-	**8**	40	40	20	**15**	20	-	80
2	80	20	-	**9**	40	20	40	**16**	-	100	-
3	80	-	20	**10**	40	-	60	**17**	-	80	20
4	60	40	-	**11**	20	80	-	**18**	-	60	40
5	60	20	20	**12**	20	60	20	**19**	-	40	60
6	60	-	40	**13**	20	40	40	**20**	-	20	80
7	40	60	-	**14**	20	20	60	**21**	-	-	100

R	1	2	3	4	5	6	7	Anode contact
8	9	10	11	12	13	14	**R**	
R	15	16	17	18	19	20	21	

Figure 2-7. Template for spotting mixtures on a FTO electrode. R stands for the CoFeNi (4:4:2) reference

2.4.3 Data Acquisition and Processing

Electrolysis and image acquisition is done in a dark room. In the customized electrochemical cell, a FTO slide bearing the array to be tested is secured in a plastic holder. A 1 mm thick plastic spacer is placed between the holder and the O_2-sensing mesh with the painted side of the mesh up. Another holder is placed atop the mesh, after which the entire cell is clamped tight, sealed with parafilm, and purged with argon for five minutes before injecting 100 mL of purged 0.1 M NaOH solution (Figure 2-8). The cell is purged for an additional fifteen minutes (or until the red fluorescence is predominant). A conventional digital camera is clamped about 20 cm above the cell, as well as a light filter that blocks wavelengths below 440 nm. Two ~ 400 nm UV flashlights are set up so as to ensure optimal coverage of the mesh.

Subsequent constant potential electrolysis is carried out at 670 mV vs. Ag/AgCl (420 mV overpotential) for ten minutes, during which the O2-sensing paint is briefly excited using the UV

flashlights while each of twenty photos are acquired at thirty-second intervals. In order to lengthen the lifetime of the paint and avoid spurious photochemical effects, the flashlights are only turned on when each photo is being acquired. To ensure that each metal oxide mixture has reached steady-state turnover, a sixty-minute electrolysis is done at 670 mV vs. Ag/AgCl following initial image acquisition, after which a second set of images are acquired. The results presented here are all from measurements following electrolysis to steady-state.

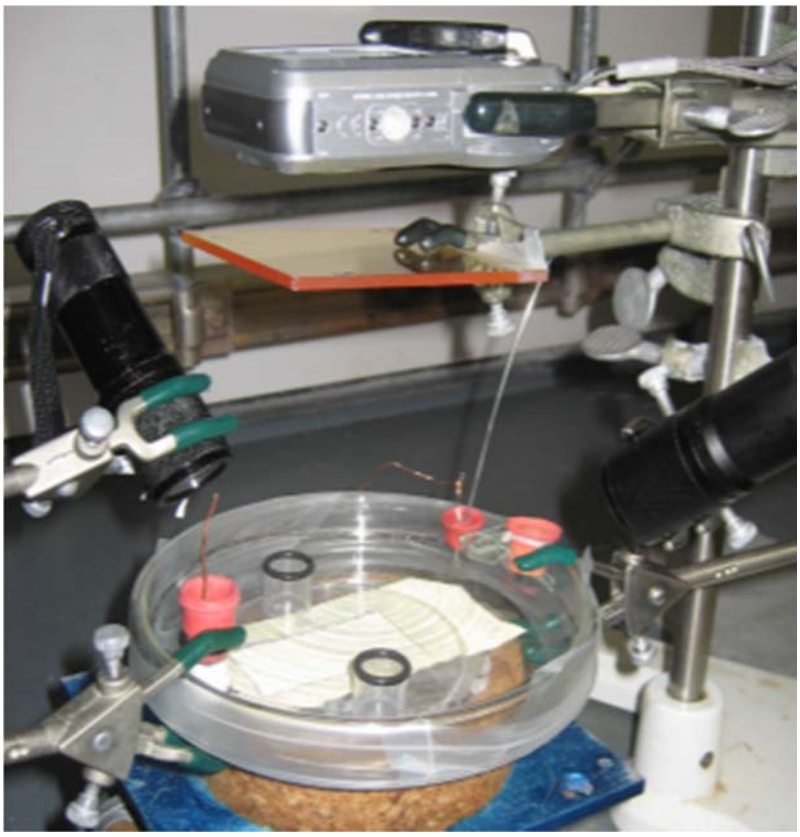

Figure 2-8. Fully assembled apparatus, except for connections to the potentiostat

The set of images from a measurement run were opened in the program ImageJ[33] and collated in an image stack after any necessary rotation or translation of images to align them. Following the procedure in Scheme 2-2, the image stack was cropped to the region containing the array being

tested, and the RGB channels were split into separate stacks. Discarding the blue channel, the red and green channels were converted to 32-bit representation and subjected to a Gaussian blur with a 12-pixel radius. The red channel was then divided by the green channel to generate a 32-bit grayscale result stack. This result was multiplied by 128 and a time-integrated result was obtained by summing the images in the stack with the Z-project command. The resulting image was inverted and subjected to background subtraction using a sliding parabola with a radius of 150 pixels to generate the background map. A macro to perform the above procedure on a stack of aligned and cropped images is given in Table 2-3. Maxima of the peaks in the image were then found, normalized relative to the average intensity of the three reference spots, and plotted via spreadsheet in the corresponding positions on the ternary composition diagram.[34] Surface plots of the image can also be produced in ImageJ. Shaded ternary diagrams (vide infra) were generated via Gnuplot with 10 interpolation steps between data points.

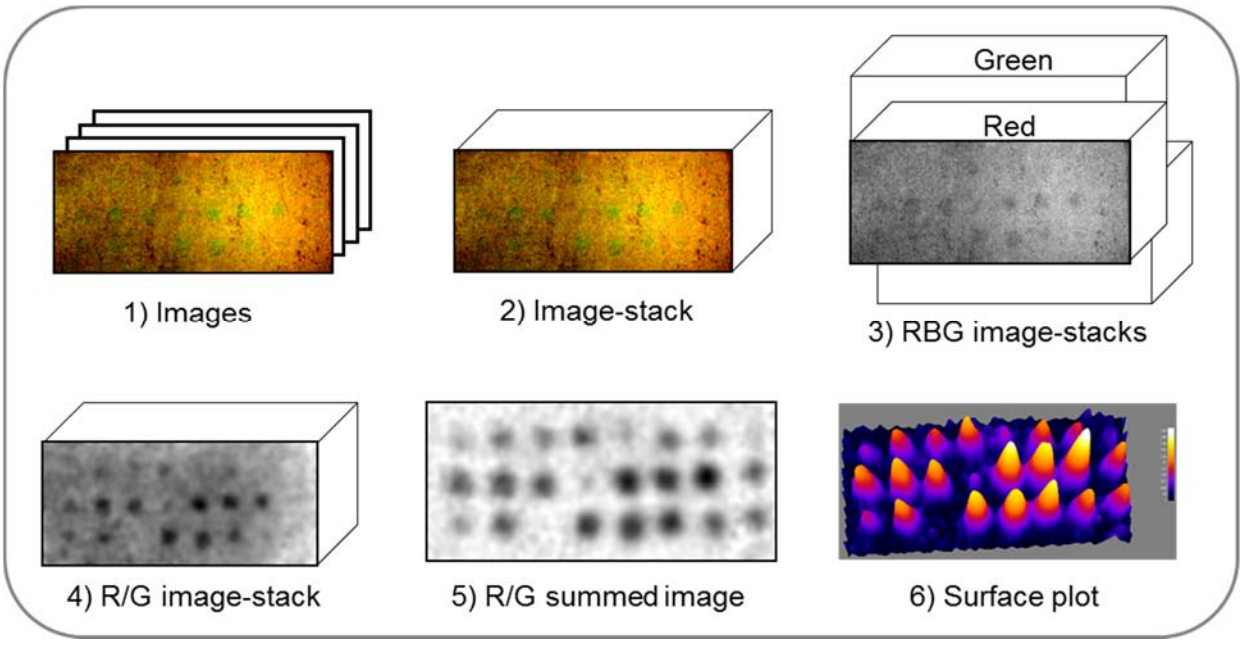

Scheme 2-2. Image Processing Procedure, Co-Al-Ni data shown

Table 2-3. Assay data post-processing macro for use with ImageJ

Step	Script
1	`run("Split Channels");`
2	`selectWindow("Stack (blue)");`
3	`close();`
4	`selectWindow("Stack (green)");`
5	`run("32-bit");`
6	`run("Gaussian Blur...", "sigma=12 stack");`
7	`selectWindow("Stack (red)");`
8	`run("32-bit");`
9	`run("Gaussian Blur...", "sigma=12 stack");`
10	`imageCalculator("Divide create 32-bit stack", "Stack (red)","Stack (green)");`
11	`selectWindow("Result of Stack (red)");`
12	`run("Invert", "stack");`
13	`run("Multiply...", "value=128 stack");`
14	`x = nSlices;`
15	`run("Z Project...", "start=1 stop=x projection=[Sum Slices]");`
16	`selectWindow("SUM_Result of Stack (red)");`
17	`run("Subtract Background...", "rolling=150 sliding");`

2.4.4 Tabulated Catalyst Screening Activities

The activities shown are all averages of multiple independently prepared arrays, normalized to a Co-Fe-Ni (4:4:2) reference (Figure 2-9). Based on comparison of compositions that appear in multiple triads, e.g. the Co-Ni edge of the Co-Al-Ni and the Co-Fe-Ni triads, the precision of this assay appears to be approximately ±0.2. Given that the dynamic range is on the order of 0 - 3, this is adequate to distinguish hits and misses as an initial screen for catalytic activity.

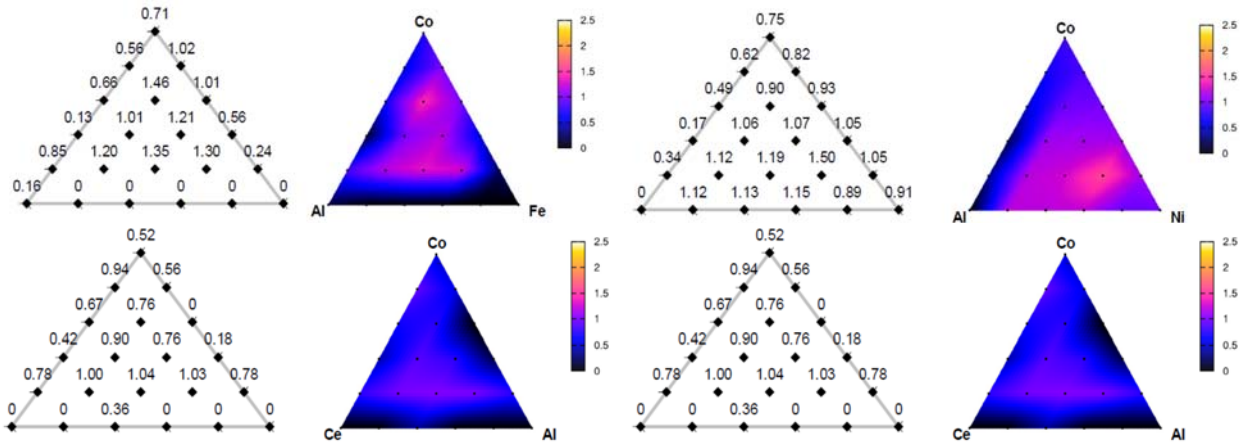

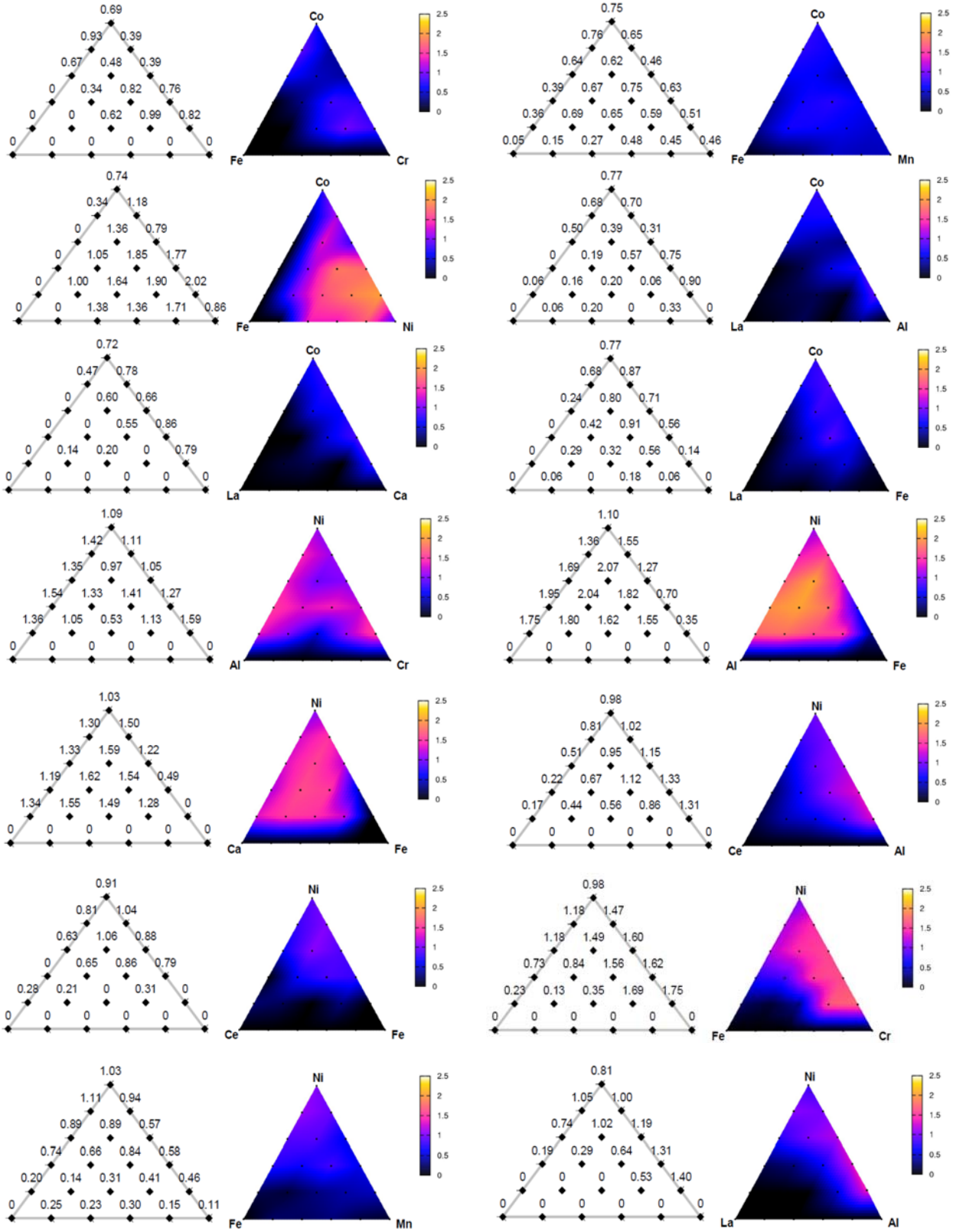
0.69
0.93 0.39
0.67 0.48 0.39
0 0.34 0.82 0.76
0 0 0.62 0.99 0.82
0 0 0 0 0 0
Co
Fe Cr
2.5 2 1.5 1 0.5 0
0.75
0.76 0.65
0.64 0.62 0.46
0.39 0.67 0.75 0.63
0.36 0.69 0.65 0.59 0.51
0.05 0.15 0.27 0.48 0.45 0.46
Co
Fe Mn
2.5 2 1.5 1 0.5 0
0.74
0.34 1.18
0 1.36 0.79
0 1.05 1.85 1.77
0 1.00 1.64 1.90 2.02
0 0 1.38 1.36 1.71 0.86
Co
Fe Ni
2.5 2 1.5 1 0.5 0
0.77
0.68 0.70
0.50 0.39 0.31
0 0.19 0.57 0.75
0.06 0.16 0.20 0.06 0.90
0 0.06 0.20 0 0.33 0
Co
La Al
2.5 2 1.5 1 0.5 0
0.72
0.47 0.78
0 0.60 0.66
0 0 0.55 0.86
0 0.14 0.20 0 0.79
0 0 0 0 0 0
Co
La Ca
2.5 2 1.5 1 0.5 0
0.77
0.68 0.87
0.24 0.80 0.71
0 0.42 0.91 0.56
0 0.29 0.32 0.56 0.14
0 0.06 0 0.18 0.06 0
Co
La Fe
2.5 2 1.5 1 0.5 0
1.09
1.42 1.11
1.35 0.97 1.05
1.54 1.33 1.41 1.27
1.36 1.05 0.53 1.13 1.59
0 0 0 0 0 0
Ni
Al Cr
2.5 2 1.5 1 0.5 0
1.10
1.36 1.55
1.69 2.07 1.27
1.95 2.04 1.82 0.70
1.75 1.80 1.62 1.55 0.35
0 0 0 0 0 0
Ni
Al Fe
2.5 2 1.5 1 0.5 0
1.03
1.30 1.50
1.33 1.59 1.22
1.19 1.62 1.54 0.49
1.34 1.55 1.49 1.28 0
0 0 0 0 0 0
Ni
Ca Fe
2.5 2 1.5 1 0.5 0
0.98
0.81 1.02
0.51 0.95 1.15
0.22 0.67 1.12 1.33
0.17 0.44 0.56 0.86 1.31
0 0 0 0 0 0
Ni
Ce Al
2.5 2 1.5 1 0.5 0
0.91
0.81 1.04
0.63 1.06 0.88
0 0.65 0.86 0.79
0.28 0.21 0 0.31 0
0 0 0 0 0 0
Ni
Ce Fe
2.5 2 1.5 1 0.5 0
0.98
1.18 1.47
1.19 1.49 1.60
0.73 0.84 1.56 1.62
0.23 0.13 0.35 1.69 1.75
0 0 0 0 0 0
Ni
Fe Cr
2.5 2 1.5 1 0.5 0
1.03
1.11 0.94
0.89 0.89 0.57
0.74 0.66 0.84 0.58
0.20 0.14 0.31 0.41 0.46
0 0.25 0.23 0.30 0.15 0.11
Ni
Fe Mn
2.5 2 1.5 1 0.5 0
0.81
1.05 1.00
0.74 1.02 1.19
0.19 0.29 0.64 1.31
0 0 0 0.53 1.40
0 0 0 0 0 0
Ni
La Al
2.5 2 1.5 1 0.5 0

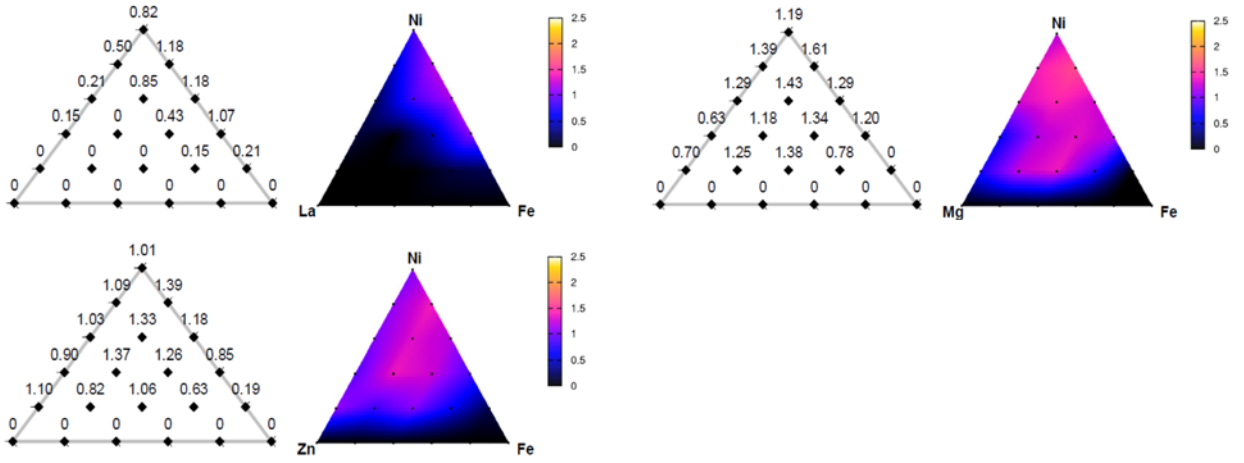

Figure 2-9. Fluorescence Screening Results for triads examined in this study

2.4.5 Tafel Measurements on Selected Catalysts

2.4.5.1 Electrode Preparation

Aliquots of 5 mM aqueous metal solutions (9 vol% glycerol) were mixed in the desired ratio. Two 1 µl drops were deposited onto a FTO (2.5cm x 1cm) electrode and dried on hotplate. Subsequently, the FTO electrode is calcined at 500 °C for six hours. The spots deposited tend to be slightly elliptical, thus major and minor axes were measured to 0.1 mm using a microscope to determine the area of the spots. Current densities are reported in terms of the projected area of the resulting ellipse, assuming uniform surface coverage and neglecting roughness or porosity of the deposit.

2.4.5.2 Tafel Analysis

Tafel data (Figure 2-10) were acquired using a standard three-compartment divided cell with 0.1 M NaOH (pH=13) electrolyte solution. Pre-electrolysis is first performed at 700 mV (vs. Ag/AgCl) until equilibrium is reached (i.e. observed current remains constant). Subsequently, steady-state currents were monitored as applied potential was varied, starting from 1000 mV (vs.

Ag/AgCl) and decreasing at 25 mV intervals until observed current is too low. Overpotentials are reported following correction for iR drop.[35] Following Tafel measurements on a blank FTO electrode, subtraction of background current at high overpotentials was performed.

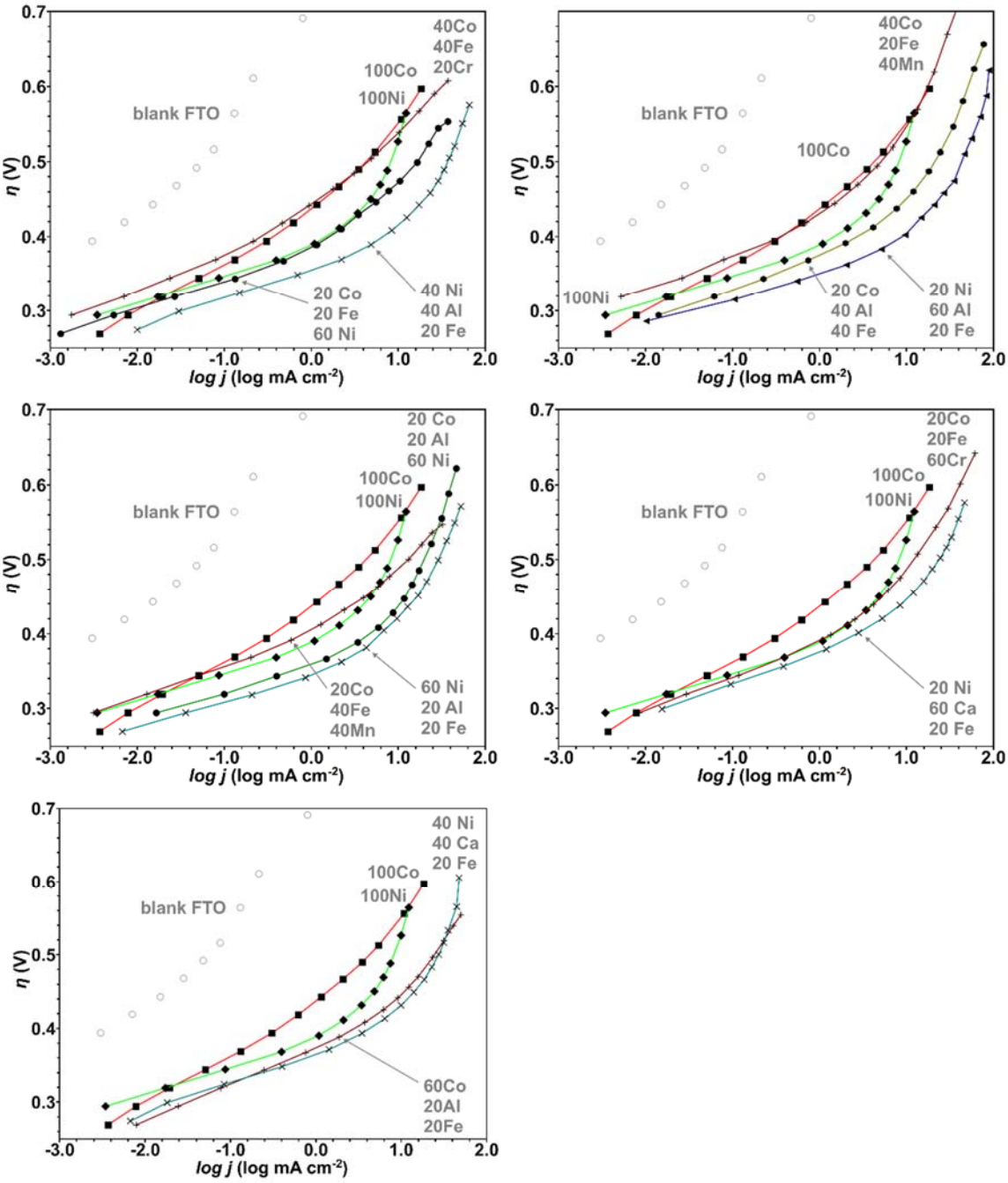

Figure 2-10. Tafel curves of selected highly-active (and less-active) compositions

2.4.6 O_2 Detection of $Ni_{0.4}Fe_{0.2}Al_{0.4}$

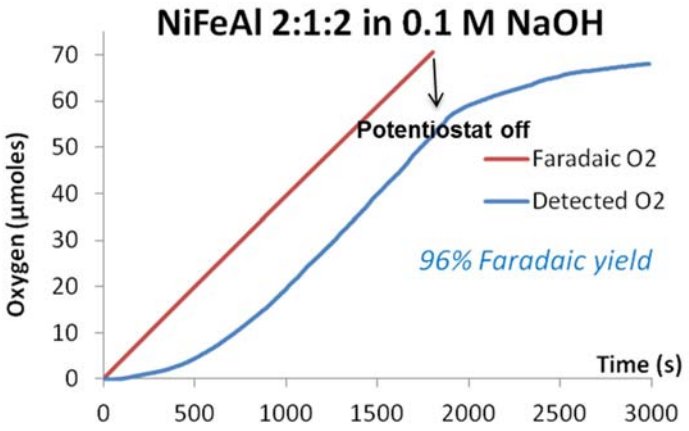

Figure 2-11. O_2 detection trace of $Ni_{0.4}Fe_{0.2}Al_{0.4}$.

O_2-detection was carried out in fully deoxygenated 0.1 M NaOH electrolyte using an Ocean Optic FOSPOR O_2 probe (O_2 sensitivity of 0 – 5%). Two 1 µl drops of 5 mM mixed metal solution were deposited onto a cleaned fluorine-doped tin oxide (FTO) electrode and calcined at 500 ºC for 6 hours. An air-tight H-cell with inlets for N_2 purging and insertion of the O_2 sensing probe was used for this experiment. Current density was fixed at 1 mA/cm^2_{geom} for 50 minutes. A 96% Faradaic yield was obtained (Figure 2-11).

2.4.7 SEM Imaging and EDX Elemental Analysis of $Ni_{0.4}Fe_{0.2}Al_{0.4}$

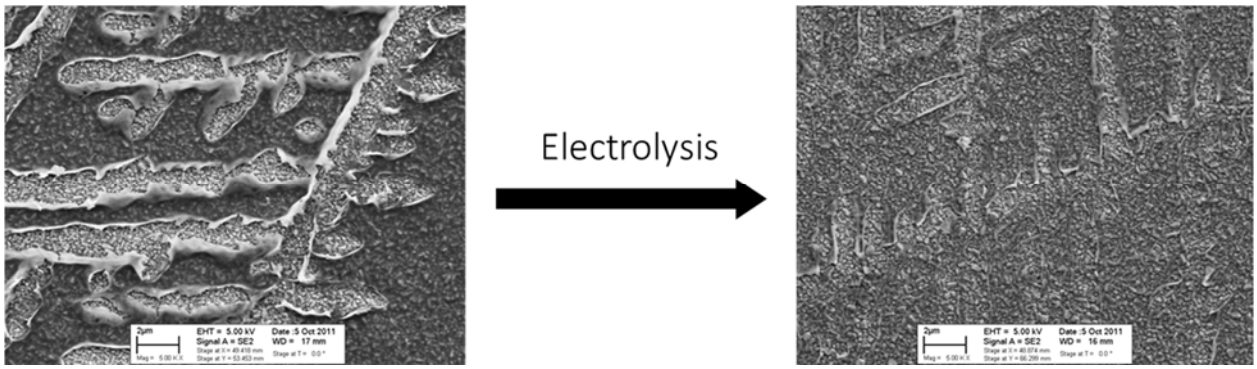

Figure 2-12. SEM images of the $Ni_{0.4}Fe_{0.2}Al_{0.4}$ catalyst before and after electrolysis.

SEM images and elemental analysis were collected using a LEO 1530 scanning electron microscope (SEM) coupled with a Thermo-Fischer NORAN Seven System energy dispersive X-ray spectroscopy (EDX) detector.

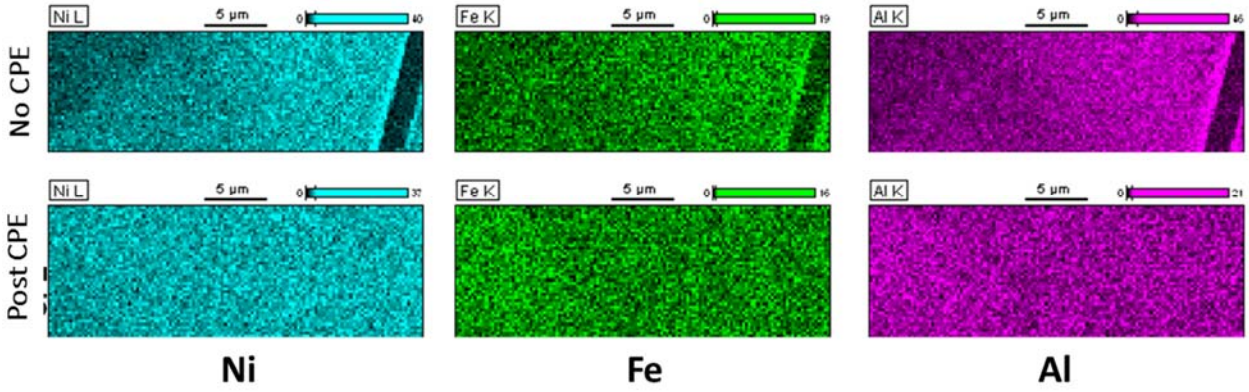

Figure 2-13. Elemental mapping of $Ni_{0.4}Fe_{0.2}Al_{0.4}$ catalyst before and after electrolysis.

$Ni_{0.4}Fe_{0.2}Al_{0.4}$ catalyst was analyzed before and after controlled potential electrolysis (CPE) at η=450 mV for 5.5 hours. SEM images (Figure 2-12) show smooth thin films with small cracks both before and after electrolysis, but the post-electrolysis film is clearly thinner. Elemental mapping (Figure 2-13) of the catalyst film demonstrates a homogeneous distribution of each metal with no evidence of phase segregation. However, elemental analysis found a ~50% loss of Al after electrolysis (Table 2-4), consistent with the high solubility of Al_2O_3 under alkaline conditions.

Table 2-4. Elemental analysis of $Ni_{0.4}Fe_{0.2}Al_{0.4}$ catalyst before and after electrolysis.

Element	Before CPE	Post CPE
Ni	2.2	2.7
Fe	1	1
Al	2.6	1

2.5 References

1. Dau, H.; Limberg, C.; Reier, T.; Risch, M.; Roggan, S.; Strasser, P. *ChemCatChem* **2010**, *2*, 724-761.
2. Betley, T. A.; Wu, Q.; Van Voorhis, T.; Nocera, D. G. *Inorg. Chem*. **2008**, *47*, 1849-1861.
3. Kanan, M. W.; Surendranath, Y.; Nocera, D. G. *Chem. Soc. Rev.* **2009**, *38*, 109-114.
4. Bockris, J. O.; Otagawa, T. *J. Electrochem. Soc.* **1984**, *131*, 290-302.
5. Suntivich, J.; May, K. J.; Gasteiger, H. A.; Goodenough, J. B.; Shao-Horn, Y. *Science* **2011**, *334*, 1383-1385.
6. Reddington, E.; Sapienza, A.; Gurau, B.; Viswanathan, R.; Sarangapani, S.; Smotkin, E. S.; Mallouk, T. E. *Science* **1998**, *280*, 1735-1737.
7. Dokoutchaev, A. G.; Abdelrazzaq, F.; Thompson, M. E.; Willson, J.; Chang, C.; Bocarsly, A. *Chem. Mater.* **2002**, *14*, 3343-3348.
8. Woodhouse, M.; Parkinson, B. A. *Chem. Soc. Rev.* **2009**, *38*, 197-210.
9. Woodhouse, M.; Herman, G. S.; Parkinson, B. A. *Chem. Mater.* **2005**, *17*, 4318-4324.
10. Katz, J. E.; Gingrich, T. R.; Santori, E. A.; Lewis, N. S. *Energy Environ. Sci.* **2009**, *2*, 103-112.
11. Winkler, G. R.; Winkler, J. R. *Rev. Sci. Instrum.* **2011**, *82*, 114101.
12. Ye, H.; Park, H. S.; Bard, A. J. *J. Phys. Chem. C* **2011**, *115*, 12464-12470.
13. Jaramillo, T. F.; Baeck, S. H.; Kleiman-Shwarsctein, A.; Choi, K. S.; Stucky, G. D.; McFarland, E. W. *J. Comb. Chem.* **2005**, *7*, 264-271.
14. Rocheleau, R. E.; Miller, E. L.; Misra, A. *Energy Fuels* **1998**, *12*, 3-10.
15. Reece, S. Y; Hamel, J. A.; Sung, K.; Jarvi, T. D.; Essewein, A. J.; Pijpers, J. J.; Nocera, D. G. *Science* **2011**, *334*, 645-648.

16. Steinmiller, E. M. P.; Choi, K. S. *Proc. Nat. Acad. Sci. USA* **2009**, *106*, 20633-20636.

17. Zhong, D. K.; Cornuz, M.; Sivula, K.; Graetzel, M.; Gamelin, D. R. *Energy Environ. Sci.* **2011**, *4*, 1759-1764.

18. Liu, T.; Campbell, B. T.; Burns, S. P.; Sullivan, J. P. *Appl. Mech. Rev.* **1997**, *50*, 227-246.

19. Matsumoto, Y.; Sato, E. *Mater. Chem. Phys.* **1986**, *14*, 397-426.

20. Godinho, M. I.; Catarino, M. A.; Pereira, M. I. D.; Mendonca, M. H.; Costa, F. M. *Electrochim. Acta* **2002**, *47*, 4307-4314.

21. Singh, R. N.; Singh, J. P.; Cong, H. N.; Chartier, P. *Int. J. Hydrogen Energy* **2006**, *31*, 1372-1378.

22. Singh, R. N.; Singh, N. K.; Singh, J. P. *Electrochim. Acta* **2002**, *47*, 3873-3879.

23. Zaharieva, I.; Najafpour, M. M.; Wiechen, M.; Haumann, M.; Kurz, P.; Dau, H. *Energy Environ. Sci.* **2011**, *4*, 2400-2408.

24. Moore, G. F.; Brudvig, G. W. *Annu Rev Conden Ma P* **2011**, *2*, 303-327.

25. Umena, Y.; Kawakami, K.; Shen, J. R.; Kamiya, N. *Nature* **2011**, *473*, 55-60.

26. Chen, Y. W. D.; Noufi, R. N. *J. Electrochem. Soc.* **1984**, *131*, 1447-1451.

27. Dincă, M.; Surendranath, Y.; Nocera, D. G. *Proc. Nat. Acad. Sci. USA* **2010**, *107*, 10337-10341.

28. Meier, R. J.; Schreml, S.; Wang, X.-d.; Landthaler, M.; Babilas, P.; Wolfbeis, O. S. *Angew. Chem. Int. Ed.* **2011**, *50*, 10893-10896.

29. Walter, M. G.; Warren, E. L.; McKone, J. R.; Boettcher, S. W.; Mi, Q. X.; Santori, E. A.; Lewis, N. S. *Chem. Rev.* **2010**, *110*, 6446-6473.

30. Certain examples of these lamps were observed to emit light with a significant tail into the visible and the use of either a cut-off filter or judicious selection of lamps is required.

31. Wold, A.; Post, B.; Banks, E. *J. Am. Chem. Soc.***1957**, *79*, 6365-6366.

32. Bockris, J. O'M.; Otagawa, T. *J. Electrochem. Soc.* **1982**, *129*, 2391-2392.

33. Abràmoff, M. D.; Magalhaes, P. J.; Ram, S. J. *Biophotonics International* **2004**, *14*, 36-42.

34. We used a modification of the spreadsheet described in: Graham, D. J.; Midgeley, N. G. *Earth Surf. Process. Landforms* **2000**, *25*, 1473-1477.

35. KapałkaA.; Fóti, G.; Comninellis C. *Electrochem. Commun.,* **2008**, *10*, 607 - 610.

Chapter III

Inverse Spinel $NiFeAlO_4$ as a Highly Active Oxygen Evolution Electrocatalyst: Promotion of Activity by a Redox-Inert Metal Ion

This work is previously published:

Chen, J. Y. C.; Miller, J. T.; Gerken, J. B.; Stahl, S. S. *Energy Environ. Sci*. **2014**, *7*, 1382-1386

3.1 Introduction

The oxygen evolution reaction (OER, Eq. 3-1) is the ideal anodic half-reaction for photoelectrochemical conversion of solar energy to chemical fuels. It is the focus of widespread attention because of the large overpotentials typically required to achieve high rates and the need to identify earth-abundant alternatives to noble-metal electrocatalysts.[1]

$$2\ H_2O \rightarrow O_2 + 4\ H^+ + 4\ e^- \quad \textbf{(Eq. 3-1)}$$

Combinatorial methods provide an efficient means to explore diverse metal oxides as potential OER electrocatalysts,[2] and we recently reported an O_2-sensitive fluorescence-quenching assay developed for this purpose.[2g] Use of this technique led to the unexpected discovery that Al^{III} ions significantly promote the catalytic activity of mixed metal oxides containing Ni, Fe, and/or Co (Figure 3-1). The most significant effect was observed with Ni/Fe-based oxides, with Al^{III}-containing compositions showing much higher activity than oxides composed of only Ni and/or Fe. Here, we report systematic structural and electrochemical studies of Ni:Fe:Al oxides, which reveal the inverse spinel $NiFeAlO_4$ as a promising, highly active OER electrocatalyst.

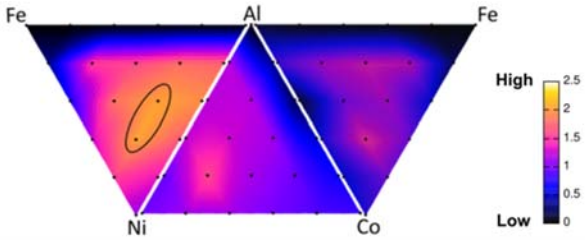

Figure 3-1. Ternary diagrams showing relative electrocatalytic water oxidation activity of thin-film mixed metal oxides at pH 13, 670 mV vs Ag/AgCl (overpotential = 406 mV). Circled compositions correspond to Ni:Fe:Al in 2:1:2 and 3:1:1 ratios (upper and lower dots, respectively. Data adapted from ref. 2g).

The catalyst screening data illustrated in Figure 1 were obtained with thin films of amorphous mixed metal oxides in which the composition of individual metal ions was varied in increments of 20 mol % (cf. black dots in Figure 3-1). Oxides composed of Ni:Fe:Al in 2:1:2 and 3:1:1

stoichiometries exhibited the highest electrocatalytic activity for water oxidation. The ability of Fe to enhance Ni-oxide electroactivity is widely known,[2h,3] but the significant promotion effect of Al in such materials was without precedent.

3.2 Results and Discussions

3.2.1 Physical Characterizations of the Oxides

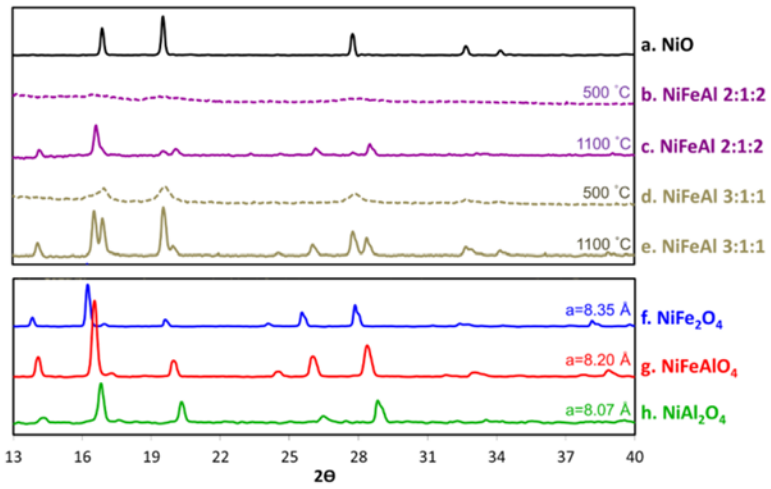

Figure 3-2. Mo Kα pXRD patterns of NiO and Ni-containing mixed metal oxides prepared by calcination at 500 or 1100 °C. Lattice parameters for the stoichiometric spinel oxides associated with diffraction patterns f, g, and h were determined using all peaks present between 2θ =13~30° following Bragg's Law

To gain structural insights into these materials, powder samples of the Ni:Fe:Al 2:1:2 and 3:1:1 mixed oxides were prepared by calcination of metal nitrate salts at 500 °C, similar to the method used in our previous screening assay. Powder X-ray diffraction (pXRD) analysis of the materials revealed only broad peaks associated with NiO (Figure 3-2a), reflecting the lack of well-defined Fe- or Al-containing oxide phases (Figs. 3-2b and 3-2d). The Ni:Fe:Al 3:1:1 material exhibited sharper NiO diffraction peaks with higher intensities. Subsequently, independent samples with the same metal-ion stoichiometries were prepared by calcination at higher temperature (1100 °C). The pXRD patterns of these materials show increased crystallinity, and the presence of new diffraction

peaks, in addition to those corresponding to NiO (Figs. 3-2c and 3-2e). We speculated that the non-NiO component(s) could account for the significant enhancement of catalytic activity with the Ni:Fe:Al-oxide materials.

The non-NiO peaks in the XRD trace exhibit a pattern similar to $NiFe_2O_4$, but with slightly higher 2θ values. $NiFe_2O_4$ is an inverse spinel oxide that has been studied previously as an electrocatalyst for water oxidation.[4] The higher 2θ values in our material reflect a smaller unit cell that could arise from substitution of Fe^{III} with Al^{III} ions within the lattice. Consequently, we prepared authentic samples of $NiFe_2O_4$, $NiFeAlO_4$, and $NiAl_2O_4$ by calcination of metal salts in the appropriate stoichiometry at 1100 °C. As shown in Figs. 3-2f –h, the XRD patterns of these materials exhibit a monotonic decrease in the lattice parameter as Al content increases.[5] The diffraction pattern of $NiFeAlO_4$ matches that of the non-NiO component present in the Ni:Fe:Al 2:1:2 and 3:1:1 mixtures (cf. Figure 3-2c and 3-2e). This inverse spinel oxide has been studied previously in the context of its magnetic properties and potential application to data storage,[5,6] but it has not been investigated as an electrocatalyst.

Inverse spinel oxides have the general formula AB_2O_4, in which the divalent cation A occupies an octahedral site and the trivalent cations B occupy one octahedral and one tetrahedral site. In $NiFeAlO_4$, the Fe^{III} and Al^{III} ions could occupy either the O_h or T_d sites (Figure 3-3).

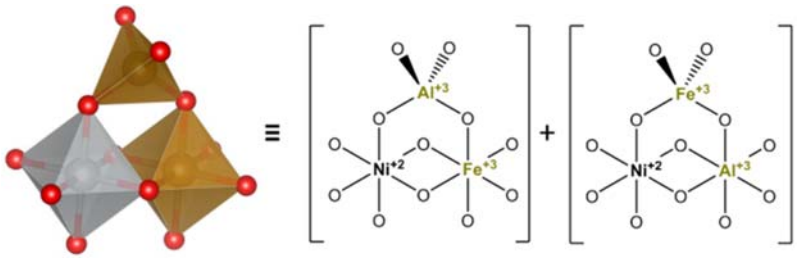

Figure 3-3. Simplified structural representation of $NiFeAlO_4$ showing only site occupancy of the metals. M^{II} ion (grey) occupies an octahedral site while M^{III} ions (brown) occupy both octahedral and tetrahedral sites.

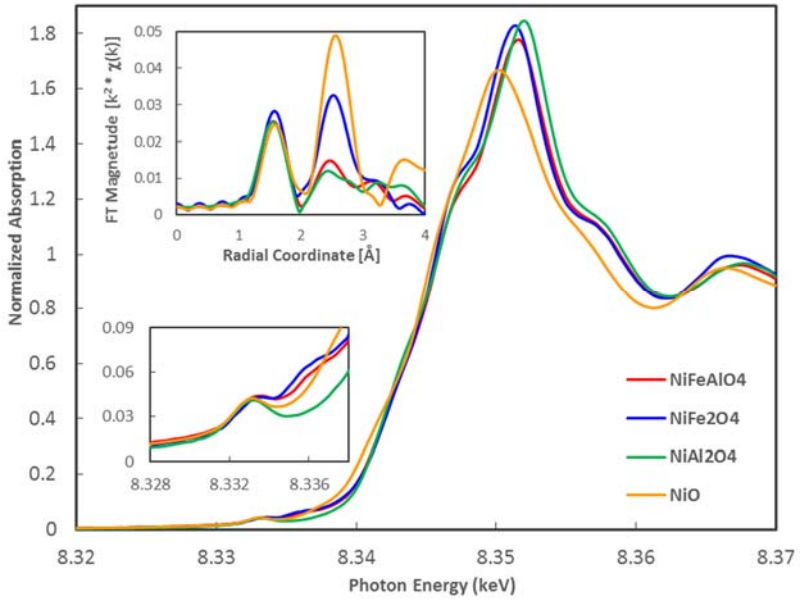

Figure 3-4. Ni-edge XAS spectra of $NiFeAlO_4$ (red), $NiFe_2O_4$ (blue), $NiAl_2O_4$ (green), and NiO (orange). Upper inset shows the Fourier transform (k^2-weighted) spectrum of the oxides in the EXAFS region showing phase-uncorrected radial coordinates. Lower inset is an expansion of the pre-edge region.

A Ni K-edge X-ray absorption (XAS) spectrum was obtained for $NiFeAlO_4$ (Figure 3-4) and compared with the spectra of NiO, $NiFe_2O_4$, and $NiAl_2O_4$. The edge positions of the inverse spinel oxides are 0.7 eV higher than that of NiO but lower than Ni^{III}, such as β-NiOOH, which is another 0.9 eV higher at 8343.7 eV.[7] The XANES edge is an allowed transition from the 1s to unfilled p states, thus the edge energy varies substantially with the types of ligands present. A more reliable determination of the oxidation state of the Ni uses the small pre-edge peak (about 8.333 keV, see lower insert). This peak is due to the dipole forbidden transition from the 1s to 3d orbitals, which is very characteristic of the oxidation state. The weak appearance of the pre-edge feature seen here is a result of the highly symmetric environment surrounding the octahedral Ni centers. A peak cooresponding to Ni-O coordination (1.6 Å of the phase-uncorrected radial coordinate) in the EXAFS region overlaps between the inverse spinel oxides and NiO (upper insert). Since all Ni atoms are octahedrally coordinated in NiO, this observed overlap indicates that the Ni atoms in the

inverse spinels are largely, if not completely, octahedrally coordinated. In the Ni-O-M coordination sphere, much reduced intensities are observed in the in the Al-containing inverse spinel oxides, reflecting the lower scattering ability of the Al atom compared to Ni and Fe.

An Fe K-edge X-ray absorption spectrum was also obtained for $NiFeAlO_4$ and compared with the spectra of Fe_3O_4, $NiFe_2O_4$, and Fe_2O_3 (Figure 3-5). In the XANES region, the pre-edge features are very similar for $NiFeAlO_4$, Fe_3O_4, and $NiFe_2O_4$, and distinct from that of the rhombohedral oxide Fe_2O_3. The pre-edge features arise from a forbidden 1s-3d electronic transition, and non-centrosymmetric lattice sites,[5] such as tetrahedrally coordinated Fe in $NiFeAlO_4$, Fe_3O_4, and $NiFe_2O_4$, have a higher extinction coefficient and dominate the absorption. The presence of this pre-edge feature in the $NiFeAlO_4$ spectrum indicates that the tetrahedral site is at least partially occupied by Fe^{III}. The Fe edge positions of $NiFe_2O_4$, $NiFeAlO_4$, and Fe_2O_3 appear at higher energy relative to that of Fe_3O_4, consistent with the higher average Fe oxidation state in the former materials (Fe^{+3} vs. $Fe^{+2.67}$).

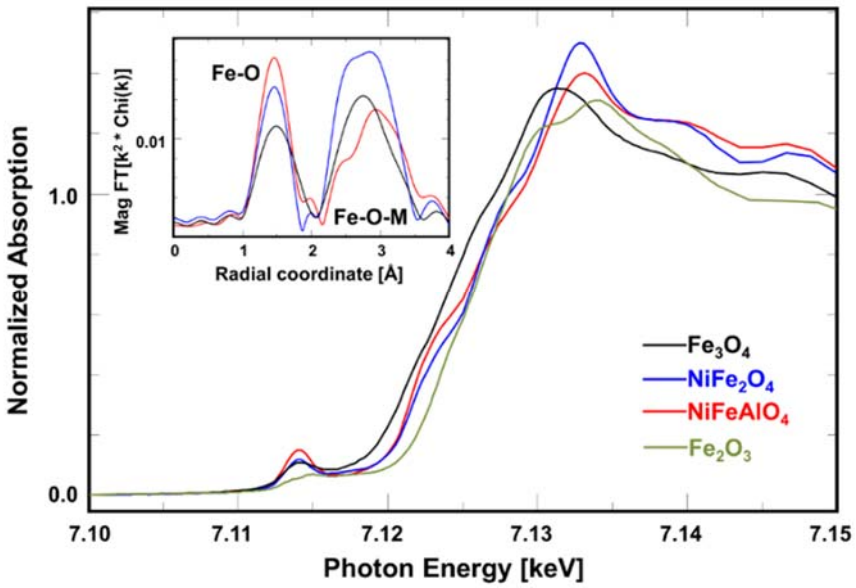

Figure 3-5. Fe-edge XAS spectra of Fe_3O_4 (black), $NiFe_2O_4$ (blue), $NiFeAlO_4$ (red), and Fe_2O_3 (magenta). Inset shows the Fourier transform (k^2-weighted) spectrum of the inverse spinel oxides in the EXAFS region showing phase-uncorrected radial coordinates.

The EXAFS regions of the spectra were also analyzed (inset, Figure 3-5; see also, Table 3-5 in Experimental Detail†). The phase-uncorrected peak at 1.4 Å for each oxide corresponds to scattering from the first coordination shell of Fe, consisting of Fe-O bonds associated with octahedral and tetrahedral Fe sites. The differences observed in peak intensity between the three inverse spinel oxides suggest variations in the distribution of Fe atoms in the O_h and T_d sites (vide infra). The peaks between 2 – 3.5 Å correspond to scattering from the second coordination sphere of Fe (Fe-O-M, M = Ni, Fe, Al). In this region, the $NiFeAlO_4$ scattering peak exhibits relatively low intensity, consistent with small crystallite sizes (i.e. more disordered).

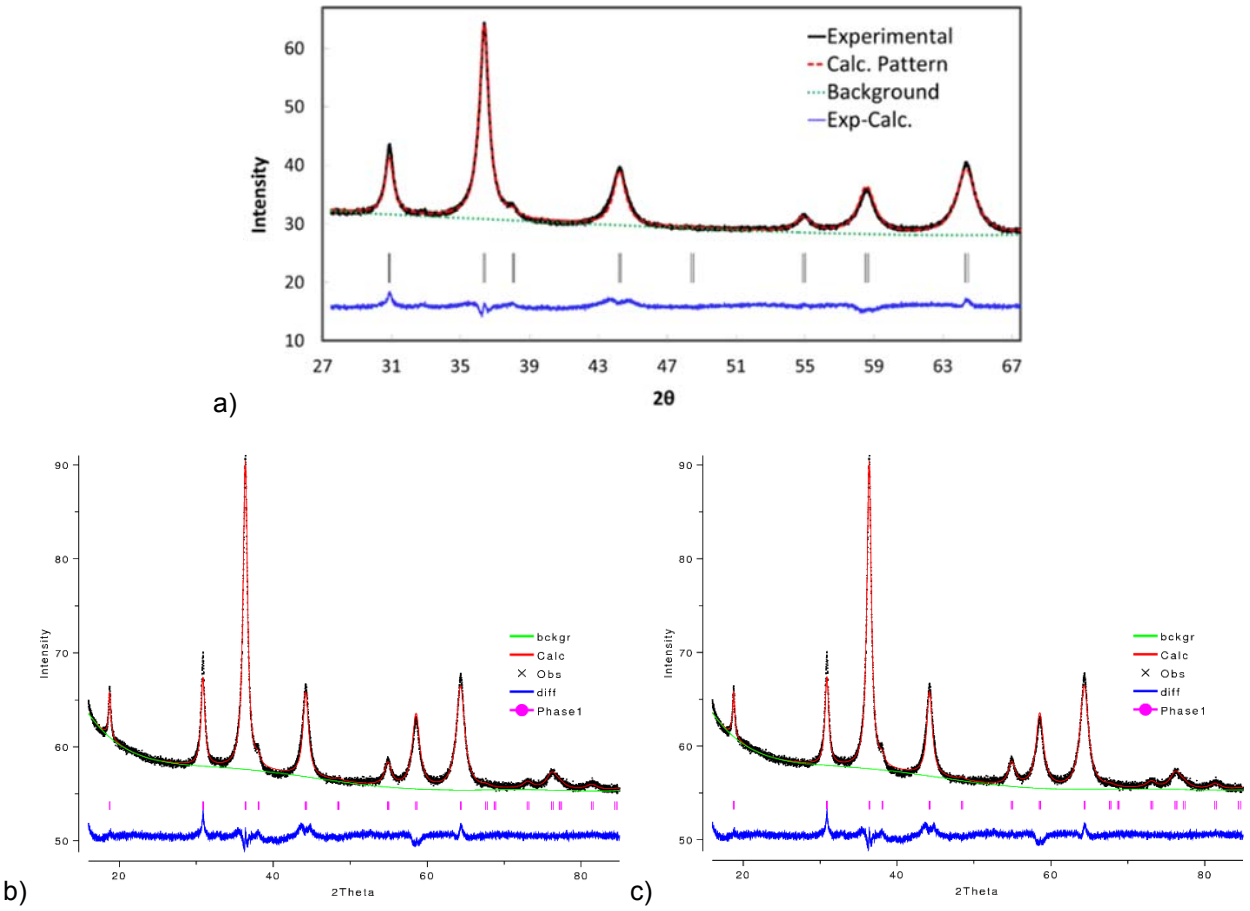

Figure 3-6. Experimental (black) and simulated (red) Cu Kα pXRD patterns for $NiFeAlO_4$. The best fit arises from Fe distribution of 64% T_d:36% O_h (a). The calculated lattice parameter matches with the one extracted for this material from the data in Figure 4-2. b) $R_f^2 = 0.036$, c) $R_f^2 = 0.037$.

Fitting of the $NiFeAlO_4$ EXAFS data provides evidence that the Fe^{III} and Al^{III} ions are distributed between the O_h vs. T_d sites (see Experimental Details);[5] however, the error associated with this fitting prevents reliable quantitation of the distribution. More precise determination of this metal-ion distribution is possible by Rietveld analysis of the pXRD pattern (Figure 3-6).[8] The diffraction patterns were simulated with the distribution of Fe and Al as refinable parameters and the Ni ions fixed in O_h sites. If Ni ions are allowed to occupy tetrahedral sites, the total electron density can remain unchanged by compensating shifts of Fe and Al ions. Although the difference in anomalous scattering between Fe and Ni with Cu Kα radiation is insufficient to rigorously locate the nickel, the Ni K-edge XAS data support the assignment of Ni ions to octahedral sites (Figure 3-4). Good agreement with all the available experimental data corresponds to an Fe distribution of 64% T_d:36% O_h, and the opposite distribution for Al (Figure 3-6a).

3.2.2 Electrochemical Analysis of the Oxides

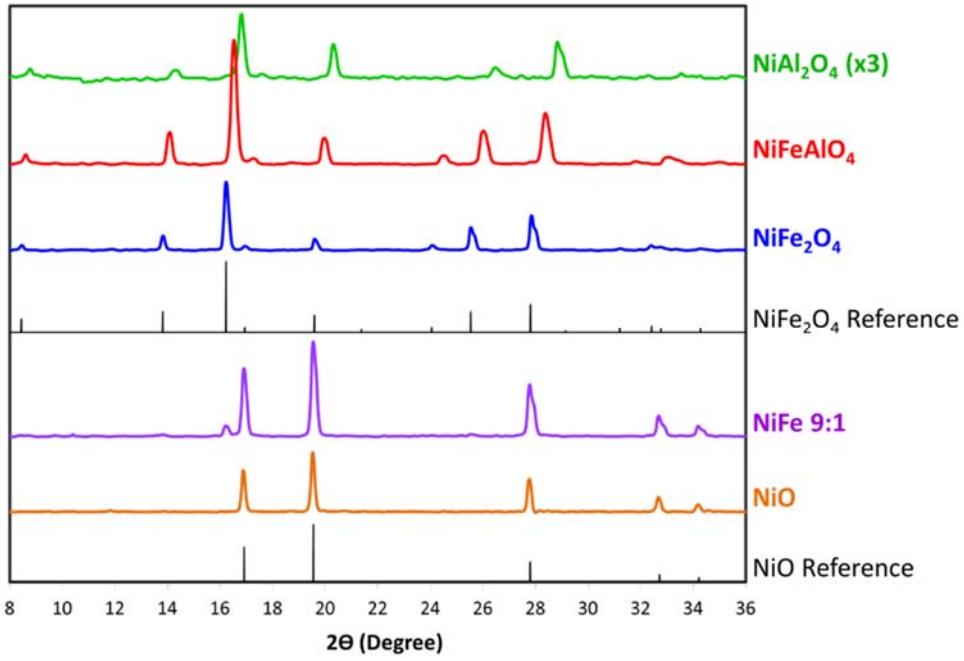

Figure 3-7. Mo Kα pXRD spectra of oxides examined for electrochemical activity. All oxides shown were prepared at 1100 °C. The intensity of the spectrum of $NiAl_2O_4$ has been expanded for easy comparison. Al_2O_3 phase was never observed. A small amount of $NiFe_2O_4$ is also observed in the spectrum of NiFe 9:1, in accordance with the literature.[9]

Inverse spinel ferrites (i.e., MFe_2O_4) with different A- (e.g., Mn^{II}, Co^{II}, Ni^{II}, Cu^{II}) and B-site (e.g., Cr^{III}, V^{III}) ions have been studied as OER electrocatalysts,[4,10,11] but $NiFeAlO_4$ is unique in its use of a redox inert Al^{III} ion in a B-site. In order to benchmark the OER activity of $NiFeAlO_4$, we investigated its electrochemical properties relative to known catalysts with related compositions, including NiO,[12] NiFe 9:1,[3c,g,h,j] and $NiFe_2O_4$,[4] as well as $NiAl_2O_4$, which has not been reported previously as an OER electrocatalyst. Each of these oxides was prepared by identical methods via calcination of metal nitrate salts at 1100 °C. The corresponding pXRD data (Figure 3-7) are consistent with single-phase crystalline materials, except for NiFe 9:1, in which both NiO and small amounts of $NiFe_2O_4$ were present.[4g]

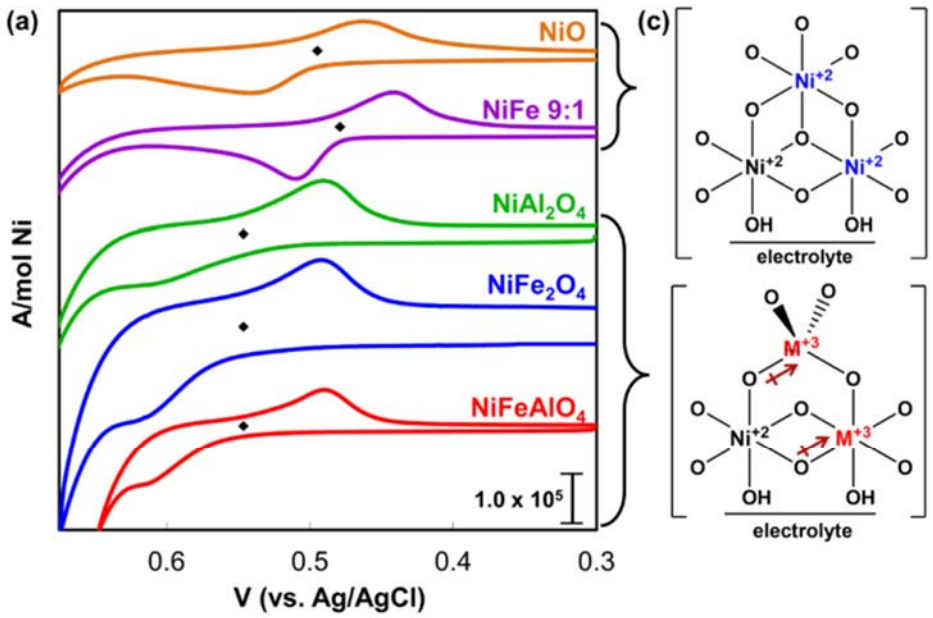

(b)

Oxide	Ni^{+2}/Ni^{+3} $E_{1/2}$ (mV vs. Ag/AgCl)	E at 2.5×10^5 A/mol Ni (mV vs. Ag/AgCl)
NiO	502	710
NiFe 9:1	476	700
$NiAl_2O_4$	555	681
$NiFe_2O_4$	556	660
$NiFeAlO_4$	558	651

Figure 3-8. Redox properties of different Ni-based oxide materials. (a) Cyclic voltammograms (corrected for ohmic resistance); black diamonds indicate the $E_{1/2}$ position. (b) Tabulated $E_{1/2}$ (Ni^{II}/Ni^{III}) and the potentials required to achieve a current density of 2.5×10^5 A/mol Ni. (c) Structural representations of NiO and inverse spinel oxides.

Voltammograms of all five oxides (Figure 3-8a) reveal a distinct Ni^{II}/Ni^{III} redox feature, and the $E_{1/2}$ value for the inverse spinel oxides lies ~50 mV higher than that of the NiO-based materials (Figure 3-8b).[13] This observation can be rationalized by the inductive effect of M^{III} ions proximal to Ni^{II} in the inverse spinel lattice (Figure 3-8c).[14] In contrast, the Ni^{II} ions in the NiO materials (i.e., NiO and NiFe 9:1) are predominantly surrounded by other Ni^{II} ions. In this way, the short-range effects arising from the incorporation of M^{III} ions in the lattice can perturb the extended electronic structure of the solid oxide. The onset of catalytic activity (defined as the potential at a current density of 2.5 x 10^5 A/mol Ni, Figure 3-8b) exhibits the opposite trend: the catalytic wave appears at lower potential for the inverse spinel oxides relative to NiO and NiFe 9:1.

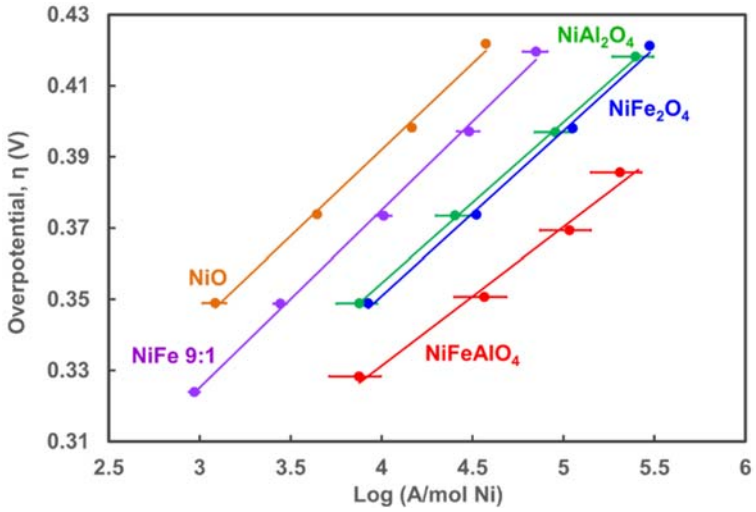

Figure 3-9. Steady-state Tafel plot of the oxides in the low current density linear regime. Data shown are the average of three trials with error bars indicating one standard deviation. The error bars for $NiFe_2O_4$ is very small and hidden within the data point symbols.

Steady-state Tafel measurements were used to obtain a more quantitative assessment of the OER electrocatalytic activity (Figure 3-9). The activity of each oxide was normalized to the amount of redox active Ni in each material detected by cyclic voltammetry (Figure 3-11; see Experimental Details).[15] As shown in Figure 3-9, the NiFe 9:1 mixed oxide shows enhanced

activity relative to NiO. The spinel-based oxides exhibit even higher activity, with $NiFeAlO_4$ showing the highest activity among this group while achieving 94% Faradaic yield (Figure 3-16, see Experimental Details). The similar performance of $NiAl_2O_4$ and $NiFe_2O_4$ suggests Fe-based redox activity is not required for catalytic O_2 formation, while the improved performance of $NiFeAlO_4$ relative to $NiFe_2O_4$ and $NiAl_2O_4$ suggests that Fe and Al play a synergistic role in water oxidation.

Elemental analysis of the $NiFeAlO_4$ material before and after a 15 h electrolysis (Figure 3-17) reveals no significant change in the ratio of the three metals (overpotential = 500 mV; see Table 3-1). This observation is significant in light of the solubility of hydrated Al_2O_3 at pH 13 (Ksp = 10^{-2} M).[16] The lack of Al leaching implies significant stabilization of the Al ions within the $NiFeAlO_4$ lattice.

Table 3-1. Elemental analysis of $NiFeAlO_4$ before and after electrolysis.

Element	Initial	Electrolyzed
Ni	1	1
Fe	1.02 ± 0.08	1.03 ± 0.06
Al	1.04 ± 0.15	1.21 ± 0.22

The beneficial effect of a redox-inert metal ion in $NiFeAlO_4$ is noteworthy[17] and reminiscent of Ca^{II} in the OEC of photosystem II. The calcium ion has been suggested to play at least two roles: to bind and activate one water molecule that participates in O–O bond formation[18] and/or to modulate the Mn redox properties within the OEC.[19] The mechanistic role of Al^{III} in $NiFeAlO_4$ includes, but is not limited to, modulation of the Ni redox properties. This redox influence is not unique to Al, but arises from incorporation of M^{III} ions into the oxide lattice. It is tempting to speculate that the low overpotential for $NiFeAlO_4$ (cf. Figure 3-9) reflects the ability of Al^{III} to

activate a water molecule for O–O bond formation, but further studies are needed to elucidate the mechanistic role of Al (and Fe) in these systems.

3.3 Conclusions

We have identified the inverse spinel oxide $NiFeAlO_4$ as a novel low-overpotential electrocatalyst for water oxidation. These results add definition to the unexpected and ill-defined promoting effect Al ions has on Ni/Fe-based electrocatalysts, discovered via combinatorial screening. The identification of a $NiAlFeO_4$ as a well-defined composition of matter associated with this effect should greatly facilitate mechanistic investigations and testing in (photo)electro-chemical devices. Efforts toward these goals have been initiated.

3.4 Experimental Details

$Ni(NO_3)_3$, $Fe(NO_3)_3$, $Al(NO_3)_3$ hydrates, and NaOH (99%) were purchased from Sigma Aldrich and used as received. Glassy carbon rotating disk electrodes (Pine Instruments) were sonicated in nitric acid for 2 hours prior to first use. Before each use, the glassy carbon electrode is polished first with a fine grid pad, followed by 0.05 μm alumina. An aqueous Ag/AgCl reference electrode (3 M NaCl) and Pt wire counter electrodes (BASi Analytical Instruments) were used. The Ag/AgCl reference electrode is regenerated in 3 M KCl after 2-3 experiments due to the corrosive nature of the alkaline conditions to the vycor tip. $K_3Fe(CN)_6$ (in pH 7 phosphate solution, $E_{1/2}$=225 mV vs. Ag/AgCl) was used to check the potential of the reference electrode after regeneration. Acetylene black conductive carbon powder is obtained from Soltex Inc. and treated with HNO_3 at 80 °C for 12 hours. Nafion (5 wt% in an alcohol solution) was purchased from Sigma Aldrich. Ultrapure water (Thermo-Scientific, 18 MΩ) was used for all solution preparations.

3.4.1 Catalyst Preparation

Oxide powders were prepared by nitrate combustion followed by calcination. In an alumina crucible, 1 M aqueous metal nitrate solutions containing 0.5 M glycine were mixed in the appropriate ratios. Combustion was carried out behind a blast shield on a hot plate at the highest setting, during which vigorous bubbling was observed with occasional sparking. In the case of NiO, a stainless steel mesh was used to cover the crucible to prevent powder dispersion into air. Subsequently, the dried powders were calcined at either 500 °C for 6 hours at 250 °C per hour (used for screening assay) or 1100 °C for 1 hour with a ramp at 998 °C per hour (the highest ramp rate of our furnace). The oxide was allowed to cool to room temperature inside the furnace.

3.4.2 Materials Characterizations

Powder X-ray diffraction patterns (pXRD) were recorded using Rigaku Rapid II system equipped with a 2-D imaging plate and Mo Kα X-ray tube (λ= 0.709Å) at room temperature. The detector was operated at 50 kV and 50 mA and scans were collected between the range of 5° - 45° with a step size of 0.01° and a sampling time of 0.3 s per step. Ground powder samples were mounted on a glass fiber using clear nail polish or vacuum grease as adhesive. The recorded patterns were matched to NiO (PDF#47-1049), $NiFe_2O_4$ (PDF#10-0325), and $NiAl_2O_4$ (PDF#1-1299) patterns from the ICDD database.

Surface areas (3-trial average) were determined by the N_2-BET method. Measurements were collected using a Micrometrics Gemini VII 2390 Analyzer. Three measurements were collected for each oxide sample and standard deviation reported as the error (Figure 3-10).

Particle images and elemental analysis were performed using a LEO 1530 scanning electron microscope (SEM) coupled with a Thermo-Fischer energy dispersive X-ray spectroscopy (EDX) detector (Figure 3-10).

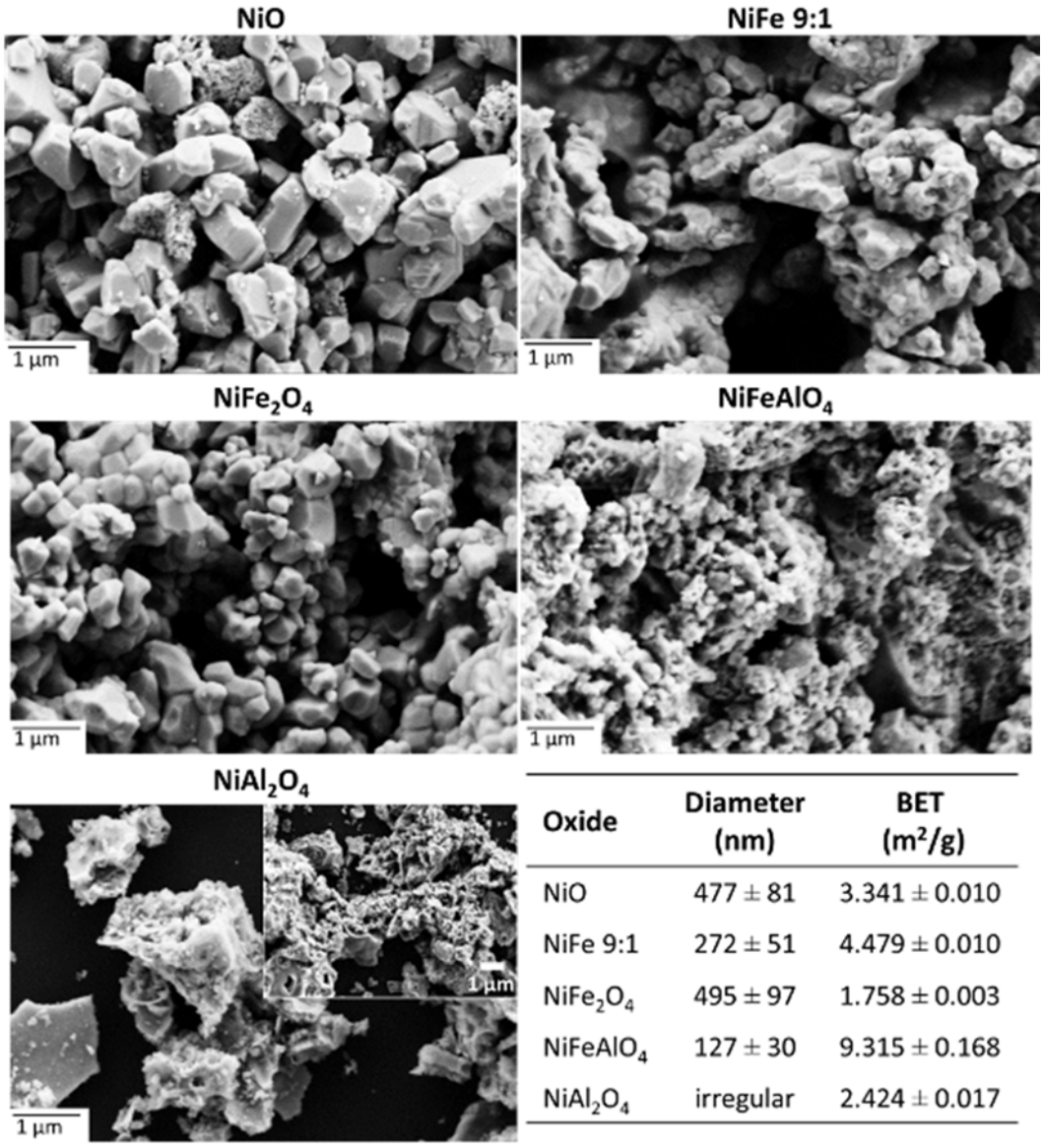

Oxide	Diameter (nm)	BET (m^2/g)
NiO	477 ± 81	3.341 ± 0.010
NiFe 9:1	272 ± 51	4.479 ± 0.010
$NiFe_2O_4$	495 ± 97	1.758 ± 0.003
$NiFeAlO_4$	127 ± 30	9.315 ± 0.168
$NiAl_2O_4$	irregular	2.424 ± 0.017

Figure 3-10. SEM images of the oxides with particle size and BET surface area measurements. NiO, NiFe 9:1, and $NiFe_2O_4$ exhibit highly facetted appearances, demonstrating their high crystallinity resulting from the high temperature calcination. Oxides containing Al are noticeably less facetted under identical preparation conditions, particularly $NiAl_2O_4$. The inset in the figure of $NiAl_2O_4$ shows a lower magnification view of the oxide. BET measurements showed low surface areas, consistent with the large particle sizes observed (diameters were averaged over 50 particles).

3.4.3 Rietveld Refinement and XRD Simulation

Powder X-ray diffraction (XRD) for Rietveld refinement was performed on a D-8 Advance X-ray diffractometer with Cu Kα radiation (λ=1.54056 and 1.54439 Å, 1:0.5 ratio) at room temperature. XRD patterns were recorded between the range of 12-85° and 27.5-68.5° with a step size of 0.01° and a sampling time of 10 seconds per step. Rietveld refinement was done using

EXPGUI and GSAS software.[20] Gaussian broadening parameters were obtained by fitting a NaCl diffraction pattern obtained on the same instrument over the same 2θ range with a step size of 0.01° and a sampling time of 7 seconds per step. Lorentzian broadening, U_{iso}, unit cell length, O position, and Fe and Al fractional occupancies were refined for both $NiFeAlO_4$ datasets together. Background, absorption, and sample translation, shift, and asymmetry parameters were refined for each sample independently. Additional structural models of the spinel oxides were constructed in VESTA and simulated powder patterns were created from the models using RIETAN-FP.[21,22] In these models, the nickel ions were ordered on sublattices within the octahedral sites. The best fit to the experimental data was achieved with Fd-3m symmetry, indicating disordered cation distribution within the O_h sites, compared to the ordering of the Ni occupancy of the octahedral sites in either $P4_122$ or Immb symmetry.[23]

3.4.4 Electrochemistry

All electrochemical experiments were performed using a standard three-component electrolysis cell with either a BASi Analytical Instrument or PINE Instrument Company potentiostat.

Catalyst ink was prepared as follows: 2.5 mg of the oxide was mixed with 2.5 mg of acetylene black conductive carbon additive. Nafion (5 wt%, 0.15 mL, adjusted to pH 11 with 0.1 M NaOH) and 0.85 mL of H_2O:*i*PrOH in 80:20 ratio were subsequently added. Sonication of the ink for at least 30 minutes provided the necessary mixing, and 10 μL of ink was then deposited onto a glassy carbon (GC) rotating disk electrode. The ink deposit was removed by rinsing and sonication in methanol. The GC electrode was polished before each use with 0.5 μm alumina, followed by sonication in methanol to remove residual alumina. In all experiments, GC rotating disk (0.25 mm diameter), Ag/AgCl (in 3 M NaCl or KCl), and Pt wire were used as the working, reference, and

counter electrode respectively. The electrolyte was a 0.1 M (pH 13) NaOH solution. All potentials were referenced to Ag/AgCl (0.209 V vs. NHE).

Cyclic voltammograms (CV) were collected using scan rates of 50 and 1 mV/s *at the end of the Tafel experiments (after reaching steady state).* Ohmic resistances for CV experiments were correct using values measured by the BASi potentiostat. Prior to the collection of *Tafel data*, pre-electrolysis was performed at 0.7 V (vs. Ag/AgCl) until a steady current is observed. Tafel data were subsequently collected starting from 0.8 V vs. Ag/AgCl and decreased by 25 mV increments until the observed current fell below 10^{-7} A. Current was recorded at each applied potential until steady state was reached (typically 2 to 5 minutes), and the current averaged over the last 30 seconds was used to construct the Tafel plots. Ohmic resistances for the Tafel measurements were determined using method described by Kapałka et al.[24]

3.4.4.1 Electrochemical Activity Normalization Methods

Integration of the cathodic scan of the Ni^{II}/Ni^{III} feature of the cyclic voltammograms provided the moles of redox active Ni-atoms (Table 3-2). These CVs were collected at a scan rate of 1 mV/s (Figure 3-11) after the completion of the Tafel experiments where the systems have reached steady state. The CVs were collected in 0.1 M NaOH using a glassy carbon rotating disk electrode. This is a valid method of counting the mole of active Ni atoms since the Ni^{II}/Ni^{III} redox feature is isolated from other redox events. It is has been shown that Fe_3O_4 exhibits no redox event at this range of potentials, thus we assumed no change in the oxidation state of Fe atoms.[25] This method of quantify the amount of active metal has also been reported previously.[26]

Table 3-2. Averaged moles of redox active Ni (< 1% of total Ni atoms present on electrode).

	NiO	**NiFe 9:1**	**$NiFe_2O_4$**	**$NiAl_2O_4$**	**$NiFeAlO_4$**
Active Ni (mols)	$9.39E^{-10}$ ($\pm$ $1.6E^{-10}$)	$12.3E^{-10}$ ($\pm$ $0.78E^{-10}$)	$1.88E^{-10}$ ($\pm$ $0.35E^{-10}$)	$5.95E^{-10}$ ($\pm$ $1.5E^{-10}$)	$18.5E^{-10}$ ($\pm$ $3.1E^{-10}$)

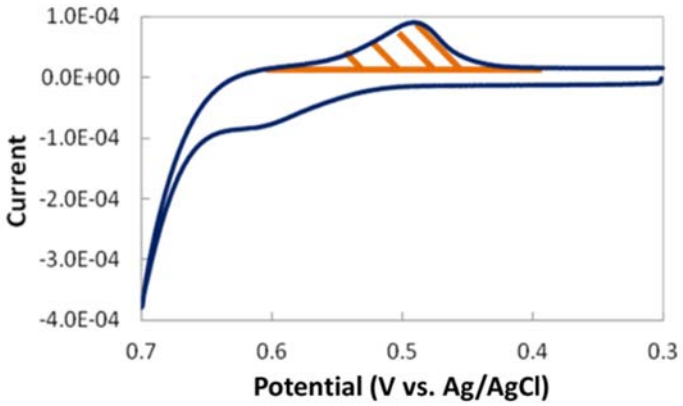

Figure 3-11. CV of $NiAl_2O_4$ illustrating area integrated in the determination of redox-active Ni-atom.

This method of normalization was chosen for a couple reasons. For thin-film oxides directly interfaced with a working electrode, normalization using geometric or electrochemically active surface area is reasonable. For powder oxides, surface area measured by BET N_2-adsorption/desorption method is appropriate. However, metal oxide water oxidation catalysts have been shown to undergo significant structural changes under applied potential, resulting in an increase in surface area.[27] Nonetheless, a correlation between BET surface area and the moles of redox active Ni-atom is observed (Figure 3-12), and when used to normalized electrochemical activity, similar trend is observed with $NiFeAlO_4$ outperforming other oxides (Figure 3-13) and exhibiting the lowest Tafel slope (Table 3-3).

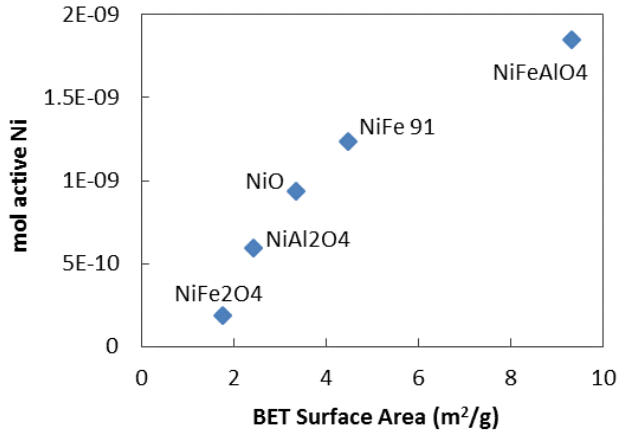

Figure 3-12. Correlation between the moles of redox active Ni (as determined by CV integration) and BET surface area. As BET surface area increased, a corresponding increase in the moles of redox active Ni was also observed.

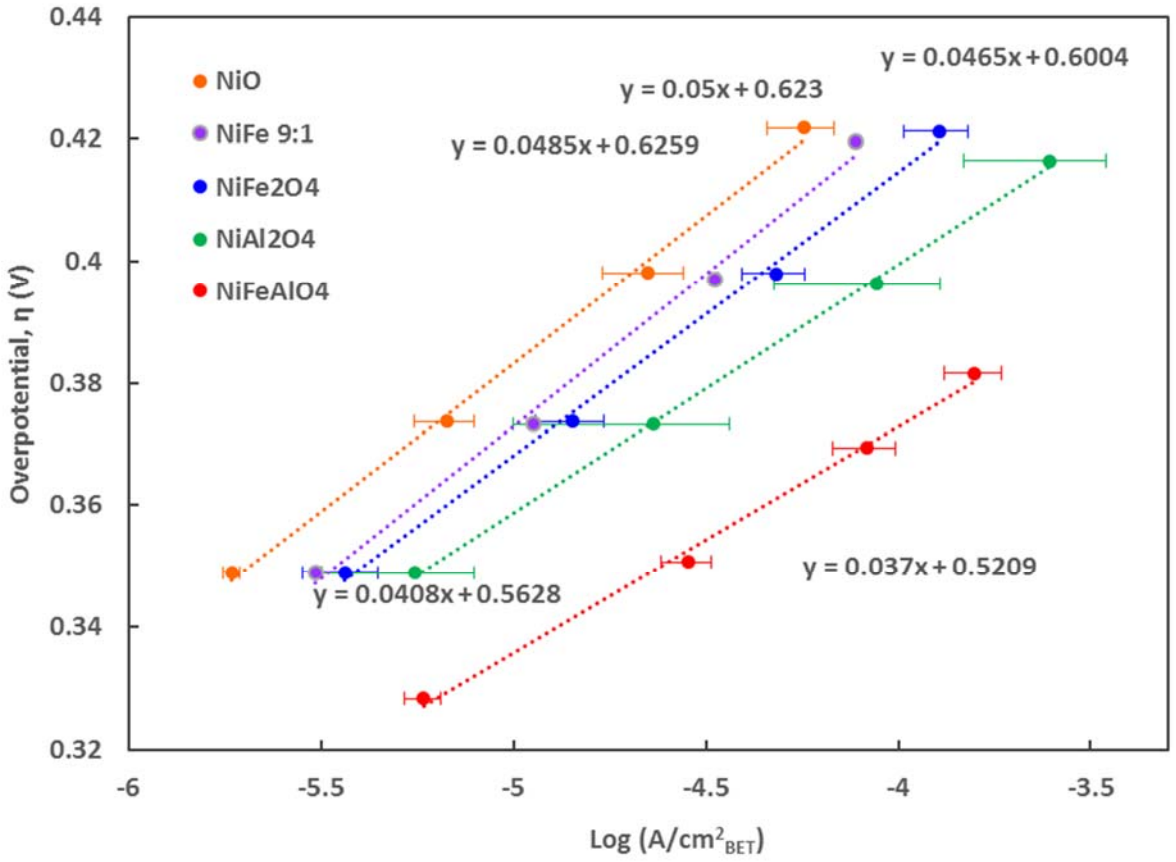

Figure 3-13. BET Surface area normalized steady-state electrocatalytic water oxidation activity. Tafel measurements were conducted in 0.1 M NaOH (pH 13) using a glassy carbon rotating disk electrode rotating at 1600 rpm. The error bar for NiFe 9:1 is small and hidden by the data symbol.

Table 3-3. Tafel slopes of the oxides examined (determined from BET surface area normalized Tafel plot) using all data points shown in Figure 3-13.

	NiO	NiFe 9:1	$NiFe_2O_4$	$NiAl_2O_4$	$NiFeAlO_4$
Tafel Slope (mV/dec)	49	50	47	41	37

An additional method is to determine electrochemically active surface area via capacitance, which can be measured by potential cycling between potentials where no faradaic process is interfering. In this study, potential was cycled between 0.2 – 0.3 V (vs. Ag/AgCl) at scan rates of 30, 20, 10, 5, and 2 mV/s (Figure 3-14a). The slope of the i - v plot gave the capacitance (Figure 3-14b).

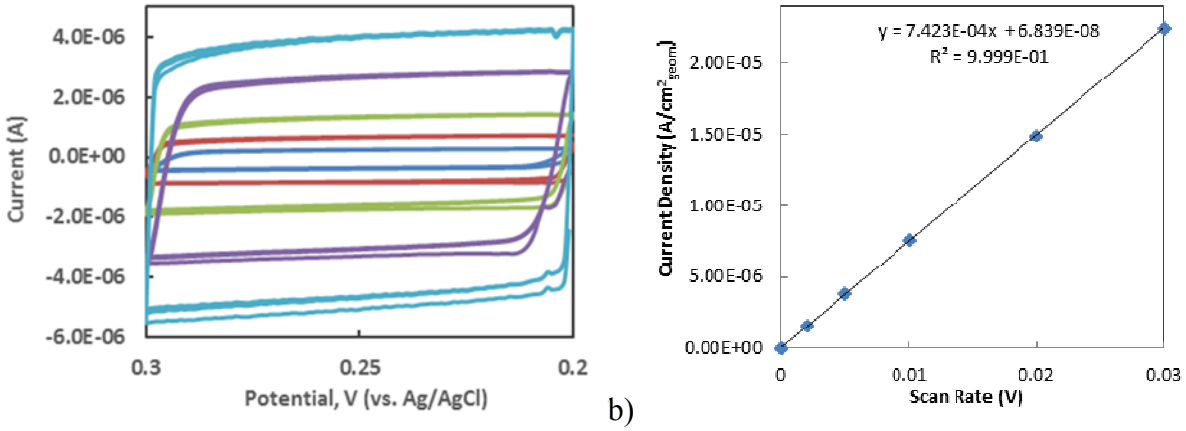

Figure 3-14. Example cyclic voltammetry and i – v plot of acetylene black, illustrating capacitance determination. Varying scan rate (v, 30, 20, 10, 5, 2 mV/s) produced different currents (a), and the slope of the i - v plot (b) gave capacitance.

For the system examined in this study, the significant amount of conductive carbon additive incorporated into the catalyst ink makes this approach unfeasible. As can be seen in Table 3-4, the capacitance of the acetylene black (AB) carbon additive clearly dominates and the addition of $NiFeAlO_4$ catalyst did not result in any significant change of the capacitance. Furthermore, the inclusion of carbon additive is necessary to achieve sufficient electrical contact between the catalyst and the electrode, as illustrated by the low capacitance of $NiFeAlO_4$ alone as compared to AB, as well as the low electrochemical activity observed when AB is excluded (Figure 3-15).

Table 3-4. Averaged capacitance of the oxides in Farad.

	$NiFeAlO_4$	**Acetylene Black**	**AB + $NiFeAlO_4$**
Pre-Electrolysis	9.56E-06 (± 1.30E-06)	1.40E-04 (±0.08E-04)	1.46E-04 (±0.05E-04)
Post-Electrolysis	2.45E-05 (± 0.39E-05)	1.78E-04 (±0.15E-04)	1.57E-04 (±0.09E-04)

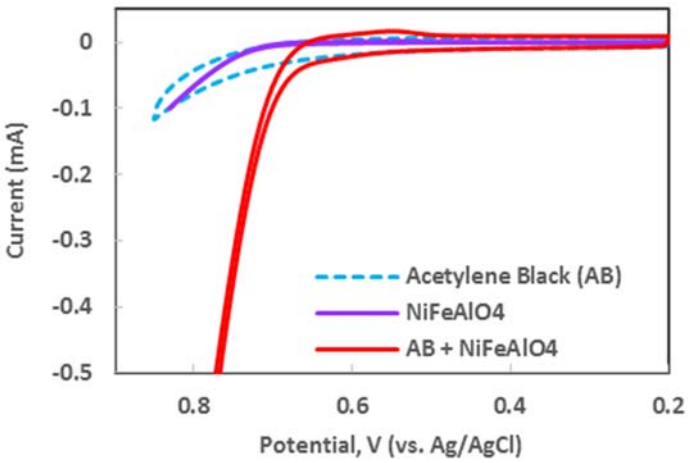

Figure 3-15. CV traces of acetylene black (AB), $NiFeAlO_4$, and [AB+$NiFeAlO_4$]. AB alone generated only low amounts of current due to its inability to oxidize water. $NiFeAlO_4$ alone also gave only low amounts of current due to insufficient electrical contact with the electrode. The combination of catalyst with AB resulted in a significant enhancement of observed current, illustrating the necessity of both the catalyst and conductive additive.

3.4.5 Oxygen Detection

O_2-detection was carried out in fully deoxygenated 0.1 M NaOH electrolyte using an Ocean Optic FOSPOR O_2 probe (O_2 sensitivity of 0 – 5%). 20 µL of the catalyst ink is deposited onto a cleaned fluorine-doped tin oxide (FTO) and an air-tight H-cell, with inlets for N_2 purging and insertion of the O_2 sensing probe, was used. Current density was fixed at 1 mA/cm^2_{geom} for 112 minutes. A 94% Faradaic yield was obtained, indicating that the oxidation of conductive carbon additive is not a significant side reactions (Figure 3-16).

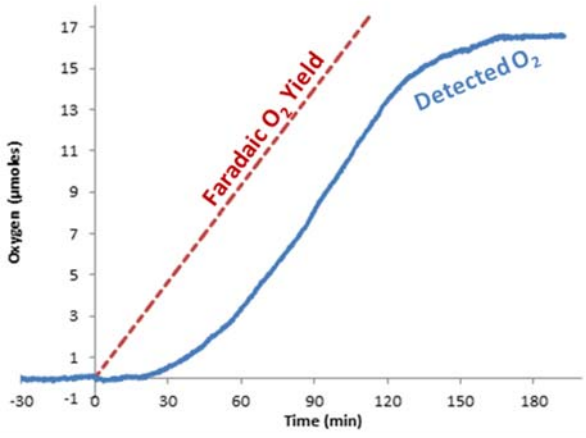

Figure 3-16. O_2 detection trace (blue line) with calculated Faradaic yield (red dotted line). The observed delay in the onset of O_2 detection is due to the time required for O_2 to diffuse out of the electrolyte solution.

3.4.6 EDX Ratiometric Analysis of $NiFeAlO_4$ Before and After an 15-hour Electrolysis

Electrolysis was carried out in 0.1 M NaOH at 750mV (vs. Ag/AgCl) for 15 hours using a glassy carbon (GC) rotating disk electrode. The electrode was prepared as described previously. An approx. 20% decrease in current was observed (Figure 3-17), however it is unclear whether this is solely due to catalyst degradation or also contributions from the degradation of the conductive carbon and/or Nafion included in the ink deposit. EDX analysis was performed on the identical electrode prior to and after the 15 hour electrolysis (see Table 3-1)

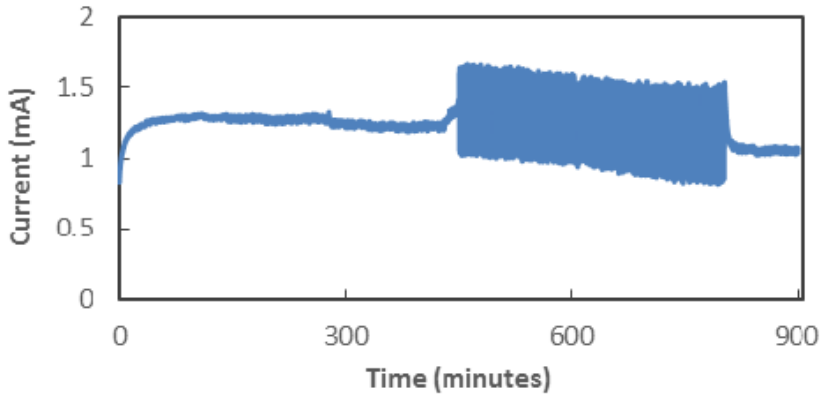

Figure 3-17. Electrolysis trace of $NiFeAlO_4$ over 15 hours. The significant noise observed between 450 – 800 minutes was due to the electrode being partially covered by large bubbles, which occurred during the night.

3.4.7 X-ray Absorption Spectroscopy

Fe (7.112 keV) and Ni (8.333 keV) K-edge X-ray absorption measurements were conducted on the bending magnet beamline of the Materials Research Collaborative Access Team (MRCAT 10-BM) at the Advanced Photon Source (APS) at Argonne National Laboratory. The X-ray ring at APS has a current of 102 mA and the beamline has a flux of 5 X 10^{10} photons/s. Ionization chambers were optimized for the maximum current with linear response (ca. 10^{10} photons detected s^{-1}). Catalyst samples were pressed into a cylindrical sample holder consisting of six wells, forming a self-supporting wafer. The catalyst amount used was calculated to give an absorbance (μx) of approximately 1.0 and data were collected in air at RT. The X-ray beam was 0.5 x 2.0

mm^2, and data were collected in transmission mode. A third detector in series simultaneously collected a Fe, or Ni foil reference spectrum with each measurement for energy calibration.

Table 3-5. Ni and Fe EXAFS Fittting Results

Ni and Fe EXAFS Fitting Results							
Sample	**Pre-edge energy (keV)**	**Scatter**	**N**	**R, Å**	**$\Delta\sigma^2$ (x 10^3)**	**E_o, eV**	**Comments**
NiO	8.3331	Ni-O	6.0	2.09	0.0	-0.3	Ni(II) XANES and Ni-O Standard
$NiAl_2O_4$ (1100 °C)	8.3331	Ni-O	6.1	2.05	0.0	-0.7	Ni(II)
$NiFe_2O_4$ (1100 °C)	8.3333	Ni-O	6.3	2.06	0.0	-1.2	Ni(II); Ni coordination similar to $NiAl_2O_4$
$NiFeAlO_4$ (1100 °C)	8.3331	Ni-O	6.2	2.05	0.0	-1.4	Ni(II)
Fe_3O_4	7.1140	Fe-O	1.3	1.88	0.0	-5.5	XANES Standard
		Fe-O	4.1	2.07	0.0	2.4	
Fe_2O_3	7.1145	Fe-O	3.0	1.96	-3.0	-4.1	XANES and EXAFS Standard
		Fe-O	3.0	2.09	-3.0	1.1	
$NiFe_2O_4$ (1100 °C)	7.1140	Fe-O	1.8	1.87	-8.0	-4.4	Fe structure similar to Fe_3O_4
		Fe-O	3.4	2.04	-8.0	3.5	
$NiFeAlO_4$ (1100 °C)	7.1141	Fe-O	1.7	1.87	-5.0	-9.7	Fe structure similar to Fe_3O_4
		Fe-O	3.4	2.04	-5.0	9.6	

XAS spectra were analyzed using *WinXAS 3.1* software and results are summarized in Table 3-5. The data were obtained from -250 eV below the edge to 1000 eV above the edge and normalized with linear and cubic fits of the pre-edge and post-edge regions, respectively. The oxidation state was obtained from the energy of the pre-edge peak and compared to respective reference compounds (i.e. NiO, Fe_3O_4, and Fe_2O_3). The pre-edge feature in Fe-edge spectra arise most prominently from tetrahedrally coordinated Fe atoms, which has an oxidation state of $^{+3}$ in Fe_3O_4. The EXAFS was extracted by performing a cubic spline fit with 5 nodes from 2.5 to 13 $Å^{-1}$. The first-shell fits of the Fe and Ni coordination sphere (i.e., Fe-O and Ni-O) were obtained by fitting the Fourier transform of the k^2-weighted EXAFS from k = 2.6 – 11.5 $Å^{-1}$ and R = 1.0 -1.8 Å using experimental phase and amplitude functions obtained from NiO (6 Ni-O at 2.09 Å). The

phase and amplitude of NiO, which is an excellent reference compound due to its high symmetry, were used to get a good fit for the Fe_2O_3 reference (3 Fe-O at 1.96 Å and 3 Fe-O at 2.09 Å). Scattering is proportional to the number of electrons in the adsorbing and scattering atoms. Since Ni^{+2} differs from Fe^{+3} by only three electrons, this small change is not enough to give a different phase and amplitude, and thus justifies the use of phase and amplitude generated from NiO. The Fe-O first shell coordination in Fe_2O_3 and Fe_3O_4 are different. Fe_3O_4 has 1 Fe atom in a T_d site with Fe-O distances of 1.88 Å and 2 Fe atoms in O_h sites with Fe-O distances of 2.07 Å. For Fe_3O_4, the fractional Fe occupancy of the T_d site is 0.33 (i.e., 1 of 3 sites), and the fractional Fe occupancy of the O_h sites is 0.667. The net Fe coordination number arising from the EXAFS fits reflects the weighted average of the Fe coordination numbers in the T_d and O_h sites:

Total T_d Fe-O bonds = 4

Total O_h Fe-O bonds = 2 x 6 = 12

Net Fe-O coordination number (N) = [4 (T_d) + 12 (O_h)]/3 Fe atoms = **5.33 Fe-O**

Using the known bond distances for T_d and O_h in Fe_3O_4, fits were adjusted to give the correct Fe-O coordination numbers for this reference material. The T_d and O_h Fe-O bond distances in $NiFe_2O_4$ are 1.88 and 2.07 Å, respectively, based on XRD data (ICSD Collection Code: 157691). In the fits used to determine the Fe occupancy of the T_d and O_h sites of the unknown samples (e.g., $NiFe_2O_4$ and $NiFeAlO_4$) these bond distances were held constant. Several Fe-O T_d and O_h coordination numbers gave acceptable fits to the EXAFS data. The fraction of Fe in a T_d site is the T_d Fe-O coordination number divided by 4 and similarly the fraction of Fe in an O_h site is the O_h Fe-O coordination number divided by 6. Correctly fitted Fe-O coordination numbers were those that resulted in a total fraction of T_d and O_h Fe equaling to 1.0 (i.e., all the Fe in the sample). For $NiFe_2O_4$ and $NiFeAlO_4$ the Fe occupancy of the T_d and O_h sites was very similar at about 0.45 T_d

and 0.55 O_h (compared to 0.33 T_d and 0.66 O_h in Fe_3O_4), which is consistent with the replacement of one octahedrally coordinated Fe by Ni atom.

3.5 References

1. For recent reviews, see: (a) Walter, M. G.; Warren, E. L.; McKone, J. R.; Boettcher, S. W.; Mi, Q. X.; Santori, E. A.; Lewis, N. S. *Chem. Rev.* **2010**, *110*, 6446-6473. (b) Surendranath, Y.; Nocera, D. G. *Prog. Inorg. Chem.* **2012**, *57*, 505-560. (c) Singh, A.; Spiccia, L. *Coord. Chem. Rev.* **2013**, *257*, 2607-2622.

2. For leading references, see: (a) Chen, G. Y.; Delafuente, D. A.; Sarangapani, S.; Mallouk, T. E. *Catal. Today* **2001**, *67*, 341-355. (b) Dokoutchaev, A. G.; Abdelrazzaq, F.; Thompson, M. E.; Willson, J.; Chang, C.; Bocarsly, A. *Chem. Mater.* **2002**, *14*, 3343-3348. (c) Jaramillo, T. F.; Baeck, S. H.; Kleiman-Shwarsctein, A.; Choi, K. S.; Stucky, G. D.; McFarland, E. W. *J. Comb. Chem.* **2005**, *7*, 264-271. (d) Woodhouse, M.; Herman, G. S.; Parkinson, B. A. *Chem. Mater.* **2005**, *17*, 4318-4324. (e) Ye, H.; Park, H. S.; Bard, A. J. *J. Phys. Chem. C* **2011**, *115*, 12464-12470. (f) Winkler, G. R.; J. R. Winkler, *Rev. Sci. Instrum.*, **2011**, *82*, 114101; (g) Gerken, J. B.; Chen, J. Y. C.; Massé, R. C.; Powell, A. B.; Stahl, S. S. *Angew. Chem. Int. Ed.* **2012**, *51*, 6676-6680. (h) Smith, R. D. L.; Prévot, M. S.; Fagan, R. D.; Trudel, S.; Berlinguette, C. P. *J. Am. Chem. Soc.* **2013**, *135*, 11580-11586. (i) Gregoire, J. M.; Xiang, C.; Mitrovic, S.; Liu, X.; Marcin, M.; Cornell, E. W.; Fan, J.; Jin, J. *J. Electrochem. Soc.* **2013**, *160*, F337-F342.

3. (a) Mlynarek, G.; Paszkiewicz, M.; Radniecka, A. *J. Appl. Electrochem.* **1984**, *14*, 145-149. (b) Córdoba, S. I.; Carbonio, R. E.; Teijelo, M. L.; Macagno, V. A. *Electrochim. Acta* **1987**, *32*, 749-755. (c) Corrigan, D. A. *J. Electrochem. Soc.* **1987**, *134*, 377-384. (d) otvin, E.; Brossard, L. *Mater. Chem. Phys.* **1992**, *31*, 311-318. (e) Miller, E. L.; Rocheleau, R. E. *J.*

Electrochem. Soc. **1997**, *144*, 3072-3077. (f) errill, M. D.; Dougherty, R. C. *J. Phys. Chem. C* **2008**, *112*, 3655-3666. (g) Landon, J.; Demeter, E.; İnoğlu, N.; Keturakis, C.; Wachs, I. E.; Vasić, R.; Frenkel, A. I.; Kitchin, J. R. *ACS Catalysis* **2012**, *2*, 1793-1801. (h) Trotochaud, L.; Ranney, J. K.; Williams, K. N.; Boettcher, S. W. *J. Am. Chem. Soc.* **2012**, *134*, 17253-17261. (i) Gong, M.; Li, Y.; Wang, H.; Liang, Y.; Wu, J. Z.; Zhou, J.; Wang, J.; Regier, T.; Wei, F.; Dai, H. *J. Am. Chem. Soc.* **2013**, *135*, 8452-8455. (j) Louie, M. W.; Bell, A. T. *J. Am. Chem. Soc.* **2013**, *135*, 12329-12337.

4. (a) C. Iwakura, M. Nishioka and H. Tamura, *Nippon Kagaku Kaishi*, 1982, 1136-1140; (b) C. Iwakura, M. Nishioka and H. Tamura, *Nippon Kagaku Kaishi*, 1982, 1294-1298; (c) N. K. Singh and R. N. Singh, *Indian J. Chem., Sect A*, 1999, **38**, 491-495; (d) D. Hong, Y. Yamada, T. Nagatomi, Y. Takai and S. Fukuzumi, *J. Am. Chem. Soc.*, 2012, **134**, 19572-19575
5. K. I. Lilova, K. Shih, C. W. Pao, J. F. Lee and A. Navrotsky, *J. Am. Ceram. Soc.*, 2012, **95**, 423-430
6. For previous characterisation of these materials, see: (a) S. J. Pickart and L. R. Maxwell, *Phys. Rev.*, 1953, **92**, 1120 -1126; (b) J. S. Smart, *Phys. Rev.*, 1954, **94**, 847-850; (c) L. Kozlowski and W. Zarek, *Acta Phys. Pol., A*, 1972, **42**, 633-674; (d) J. J. Bara, *Phys. Status Solidi A*, 1977, **44**, 737-740; (e) J. J. Bara, A. T. Pedziwiatr, Z. M. Stadnik, A. Szytula, J. Todorovič, Z. Tomkowicz and W. Zarek, *Phys. Status Solidi A*, 1977, **44**, 325-331; (f) T. Yao, O. Imafuji and H. Jinno, *J. Am. Ceram. Soc.*, 1991, **74**, 314-317
7. D. K. Bediako, B. Lassalle-Kaiser, Y. Surendranath, J. Yano, V. K. Yachandra and D. G. Nocera, *J. Am. Chem. Soc.* 2012, **134**, 6801-6809

8. (a) A. C. Larson, R B. Von Dreele, "General Structure Analysis System (GSAS)", Los Alamos National Laboratory Report LAUR 86-748 (2000); (b) B. H. Toby, *J. Appl. Cryst.*, 2001, **34**, 210-213

9. J. Landon, E. Demeter, N. İnoğlu, C. Keturakis, I. E. Wachs, R. Vasić, A. I. Frenkel and J. R. Kitchin, *ACS Catal.,* 2012, **2**, 1793-1801

10. (a) J. Orehotsky, H. Huang, C. R. Davidson and S. Srinivasan, *J. Electroanal. Chem.*, 1979, **95**, 233-235; (b) N. K. Singh, S. K. Tiwari, K. L. Anitha and R. N. Singh, *J. Chem. Soc., Faraday Trans.*, 1996, **92**, 2397-2400; (c) J. P. Singh, N. K. Singh and R. N. Singh, *Int. J. Hydrogen Energy*, 1999, **24**, 433-439; (d) J. R. Scheffe, J. Li and A. W. Weimer, *Int. J. Hydrogen Energy*, 2010, **35**, 3333-3340

11. (a) R. N. Singh, N. K. Singh and J. P. Singh, *Electrochim. Acta*, 2002, **47**, 3873-3879; (b) R. N. Singh, J. P. Singh, H. N. Cong and P. Chartier, *Int. J. Hydrogen Energy*, 2006, **31**, 1372-1378; (c) Anindita, A. Singh and R. N. Singh, *Int. J. Hydrogen Energy*, 2010, **35**, 3243-3248

12. (a) Y. W. D. Chen and R. N. Noufi, *J. Electrochem. Soc.*, 1984, **131**, 1447-1451; (b) M. Dinca, Y. Surendranath and D. G. Nocera, *Proc. Nat. Acad. Sci. USA*, 2010, **107**, 10337-10341

13. Incorporation of Fe into Ni-based layered double hydroxide (LDH) electrocatalysts via electrodeposition has been shown to increase the potential of the NiII/NiIII redox feature. See refs 3a-c,h,j. Our NiFe 9:1 oxide is distinct from LDH-type material and is composed of a mixture of NiO and NiFe2O4 (see Figure S1 in ESI†).

14. (a) J. Etourneau, J. Portier and F. Menil, J. Alloys Compd., 1992, 188, 1-7; (b) A. K. Padhi, K. S. Nanjundaswamy, C. Masquelier, S. Okada and J. B. Goodenough, J. Electrochem. Soc., 1997, 144, 1609-1613.

15. BET surface area and capacitive measurements are both unreliable for activity normalization due to the tendency for metal oxide OEC to undergo significant structural changes under applied potential (see ref 9 in ESI†), and the large contribution to capacitance by the conductive carbon incorporated in the catalyst ink (see Table S2 in ESI†).

16. E. Deltombe, C. Vanleugenhaghe, M. Pourbaix, in Atlas D'Équilibres Électrochimiques, ed. M. Pourbaix, Gauthier-Villars, Paris, 1963, Section 5.2, pp. 168-176..

17. Redox-inert metal ions have been featured in other metal-oxide electrocatalysts: (a) R. M. Bendert and D. A. Corrigan, *J. Electrochem. Soc.*, 1989, **136**, 1369-1374; (b) M. Wiechen, I. Zaharieva, H. Dau and P. Kurz, *Chem Sci*, 2012, **3**, 2330-2339; (c) M. Risch, K. Klingan, F. Ringleb, P. Chernev, I. Zaharieva, A. Fischer and H. Dau, *Chemsuschem*, 2012, **5**, 542-549

18. (a) A. W. Rutherford, *Trends Biochem. Sci*., 1989, **14**, 227-232; (b) V. L. Pecoraro, M. J. Baldwin, M. T. Caudle, W. Y. Hsieh, N. A. Law, *Pure Appl. Chem.* 1998, **70**, 925-929; (c) J. S. Vretto, D. A. Stone, G. W. Brudvig, *Chem.Rev.,* 2001, **40**, 7937-7945; (d) J. P. McEvoy, G. W. Brudvig, 2006, **106**, 4455-4483

19. (a) J. S. Kanady, E. Y. Tsui, M. W. Day and T. Agapie, *Science*, 2011, **333**, 733-736; (b) E. Y. Tsui, R. Tran, J. Yano and T. Agapie, *Nat. Chem.*, 2013, **5**, 293-299

20. a) A. C. Larson and R. B. Von Dreele, "General Structure Analysis System (GSAS)", Los Alamos National Laboratory Report LAUR 86-748 (2000); b) B. H. Toby, *J. Appl. Cryst.*, 2001, **34**, 210-213

21. K. Momma and F. Izumi, *J. Appl. Crystallogr.* 2011, **44**, 1272 - 1276

22. F. Izumi and K. Momma, *Solid State Phenom*. 2007, **130**, 15 - 20

23. For discussion of cation ordering in inverse spinels, see: C. Haas, *J. Phys. Chem. Solids,* 1965, **26**, 1225 - 1232

24. A. Kapałka, G. Foti and C. Comninellis, *Electrochem. Comm.,* 2008, **10**, 607-610

25. K.-S. Jung and L. de Pierrefeu, *Corros. Sci*. 2010, **52**, 817-825

26. T. Nakagawa, C. A. Beasley and R. W. Murray, *J. Phys. Chem. C*, 2009, **113**, 12958-12961

27. K. J. May, C. E. Carlton, K. A. Stoerzinger, M. Risch, J. Suntivich, Y.-L. Lee, A. Grimaud and Y. Shao-Horn, *Phys. Chem. Lett*. 2012, **3**, 3264-3270

Chapter IV

Operando Analysis of NiFe- and Fe-Oxide Electrocatalysts for Water Oxidation: Detection of Fe^{+4} by Mössbauer Spectroscopy

4.1 Introduction

The oxygen evolution reaction (OER) is one of the main bottlenecks in the development of efficient photoelectrochemical conversion of solar energy into chemical fuels.[1] Oxide materials containing both Ni and Fe have emerged as the most active electrocatalysts under alkaline conditions, and they exhibit substantially higher activity than oxides containing only Ni or Fe.[2] In a recent survey of trimetallic oxides, we observed that oxides with Ni, Fe and a third metal (Al, Ga, Mo, among others) are even more active than NiFe oxides.[3,4] These observations prompted us to explore the mechanistic basis for the synergistic effects of the different metals in these catalysts. In light of the complexity of the trimetallic catalysts, we elected to focus our initial studies on the simpler NiFe oxide catalysts. Here, we report operando Mössbauer spectroscopic investigations of a layered NiFe-oxide electrocatalyst under OER conditions and compare the results to those obtained with a hydrous Fe-oxide electrocatalysts. The data provide direct evidence for the formation of Fe^{+4} in the layered NiFe oxide during oxygen evolution, while no Fe^{+4} is observed in the Fe-oxide material. The results provide unique insight into the synergistic role of Ni and Fe in electrocatalytic water oxidation.

NiFe oxide catalysts have been the subject of substantial historical[2a,2b,5] and contemporary[6] investigation in the context of alkaline electrolysis and battery (e.g., NiCd) applications.[7, 8] Recent studies by the groups of Boettcher and Bell are particularly pertinent because of their focus on characterization of NiFe oxide electrocatalysts under OER conditions, and provide unique insights into these catalyst. For example, Boettcher and coworkers demonstrated that the incorporation of Fe into a NiOOH lattice enhances the oxide conductivity, but further showed that this effect is insufficient to explain the dramatic enhancement of catalytic activity.[6e] Bell and coworkers performed a thorough investigation of NiFe-oxide electrocatalysts via operando X-ray absorption

spectroscopy (XAS).[7d] They observed significant contraction of Ni–O and Fe–O bond lengths under OER conditions; however, analysis of the Fe XANES spectra led them to conclude that Fe remains largely, if not entirely, in the Fe^{+3} oxidation state. In the same report, computational studies by Nørskov and coworkers implicated Fe^{+3} species as the active sites for water oxidation.

Mössbauer spectroscopy provides a unique opportunity to probe the Fe sites in these catalysts. An early study by Corrigan and coworkers showed that the Fe sites undergo electronic and structural changes upon applying a positive potential, suitable to oxidize Ni but insufficient to promote water oxidation. The observed change in the Mössbauer isomer shift from $\delta = 0.32$ to 0.22 mm/s was attributed to partial transfer of electron density away from Fe^{+3} species.[7a] The present study builds on this earlier work by using Mössbauer spectroscopy to probe NiFe-oxide electrocatalysts under active OER conditions.

4.2 Results and Discussion

4.2.1 Catalyst Synthesis

To obtain catalyst materials suitable for operando Mössbauer studies, we sought a synthetic protocol for the preparation of NiFe oxides directly interfaced with an electrode. NiFe layered double hydroxide (LDH) catalyst precursors are readily prepared via coprecipitation and hydrothermal synthesis as powders;[9] however, interfacing these materials with an electrode typically requires use of a polymer binder, such as Nafion. The resulting catalyst composite has restricted access to catalyst active sites and often exhibits poor mechanical stability, especially under OER conditions. Cathodic deposition of NiFe hydroxides has been used in previous studies; however, these materials are often contaminated with metallic Fe and Ni.[10] Initial Mössbauer and X-ray absorption studies of electrodeposited catalysts revealed a significant amount of metallic Ni and Fe in the NiFe-oxide samples (Figure 4-10 and 4-11 in the Experimental Details).

To overcome the limitations noted above, we developed a protocol that enabled preparation of Ni, Fe and NiFe hydroxides directly on a carbon paper substrate.[11] Carbon paper provides high surface area for oxide growth and has minimal contribution to any background signal during Mössbauer measurements. Briefly, hydrothermal synthesis was carried out anaerobically using hydrates of $Ni(NO_3)_2$ and/or $FeSO_4$ at 100 °C. The use of an Fe^{+2} salt under anaerobic condition was crucial to ensure controlled precipitation of $Fe(OH)_2$, which has a K_{sp} more compatible with $Ni(OH)_2$. Triethanolamine and urea were employed as an Fe-chelating agent and in situ source of ammonia, respectively, and the carbon paper (< 0.5 mm) was included in the reaction vessel. Full details are provide in the Experimental Detail.

4.2.2 Physical Characterizations

SEM images of the 3:1 NiFe-oxide catalyst showed thin hexagonal plates vertically attached to the fibers of the carbon paper (Figure 4-1a). EDX analysis of 20-30 small areas over the entire catalyst deposit showed a Ni:Fe ratio of ~3:1 (Table 4-1). SEM images of the 100% Fe LDH/CP catalyst showed nets of needles horizontally attached to the fibers of the CP, as well as some thin plates vertically attached to CP (Figure 4-1b and insets). EDX analyses (Table 4-1) over the entire catalyst deposited area confirmed that only Fe and O are present (and carbon from CP).

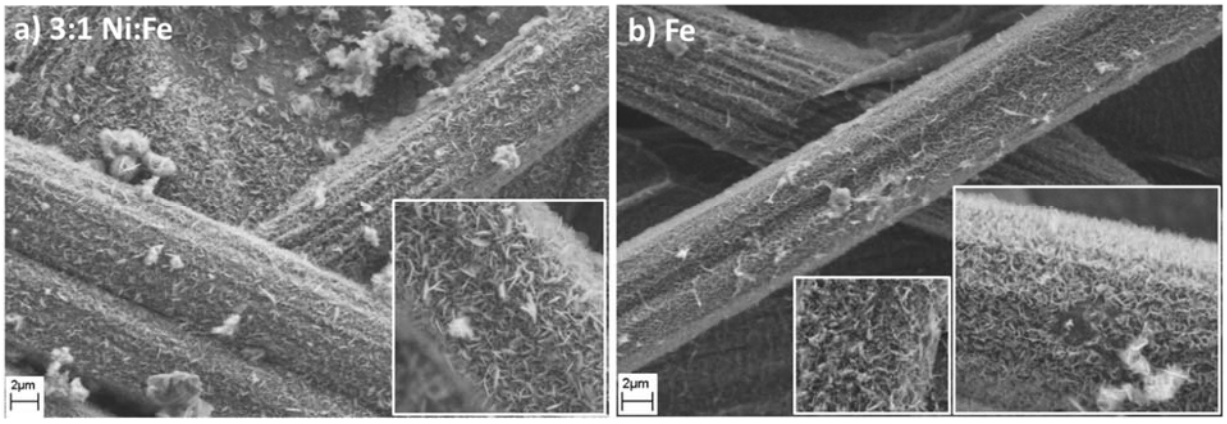

Figure 4-1. SEM images of NiFe- and Fe-oxide catalysts. Enlarged insets provide the detailed morphology of each catalyst. It is interesting to note that in the 100% Fe sample, two different fine morphologies can be observed.

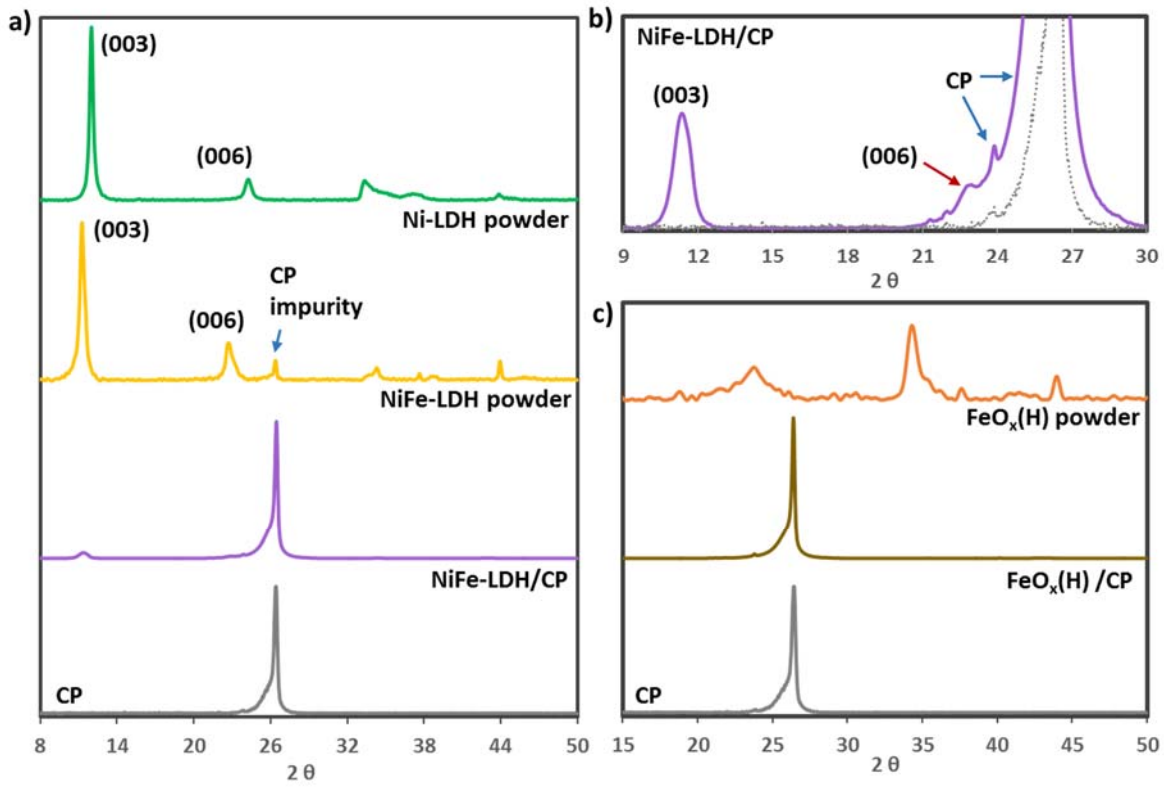

Figure 4-2. (a) Powder X-ray diffraction pattern (pXRD) of the NiFe-LDH catalyst precursor as free powder (yellow) and on carbon paper (purple and in b) showing basal peaks at θ =11.3° for the 003 plane and θ=22.6° for the 006 plane Pattern of a Ni-only oxide (green) prepared using identical method displayed similar LDH pattern with shifted 2θ values. (c) pXRD pattern for the Fe-only catalyst on carbon paper displayed no diffraction peaks (brown). Pattern of the Fe-oxide powder obtained is ill-defined.

The X-ray diffraction pattern of the NiFe catalyst (Figure 4-2a, 4-2b) showed broad peaks at θ=11.3° and 22.6° for the 003 and 006 basal planes respectively, confirming the presence of the LDH structure in the NiFe-LDH, and elemental mapping (Figure 4-3) showed an even distribution of Fe throughout the material. The patterns recorded for NiFe-LDH are consistent with those reported in the literature.[12] Pattern of a Ni-only oxide (green) prepared using identical method displayed similar LDH pattern with shifted 2θ values (Figure 4-2a) as a result of different interlayer distances. pXRD pattern for the Fe-only catalyst on carbon paper displayed no diffraction peaks (Figure 4-2c). Efforts to match the pattern of the oxide powder obtained with Fe_2O_3, Fe_3O_4, and α-, β-, γ-, δ-FeOOH were unsuccessful due to the ill-defined nature of the pattern observed.

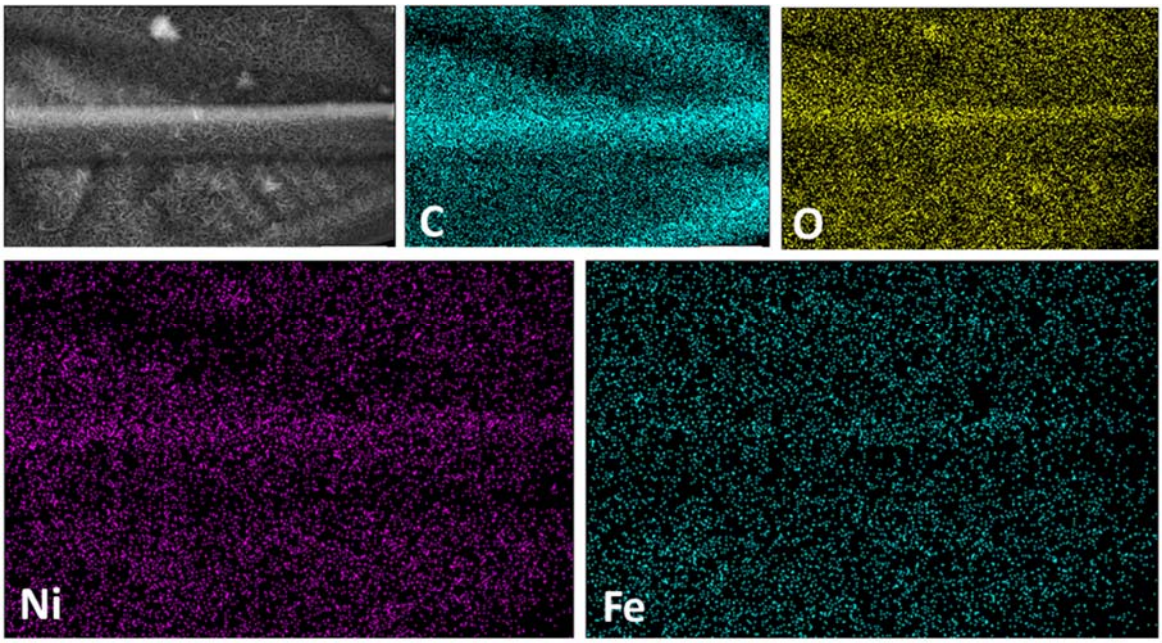

Figure 4-3. EDX elemental mapping of the 3:1 NiFe-LDH catalyst showing no evidence of phase segregation.

4.2.3 Cyclic Voltammetry

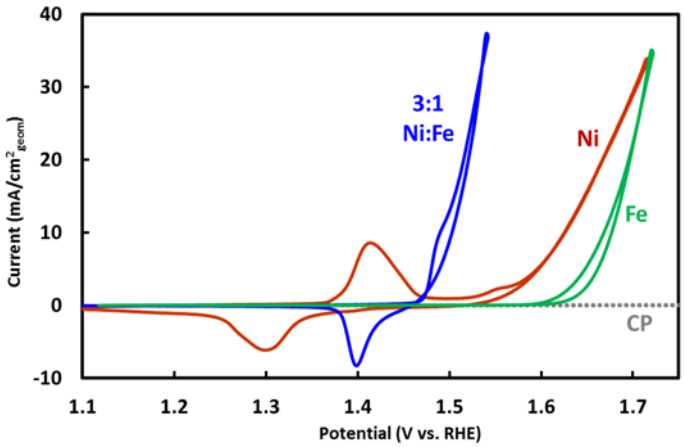

Figure 4-4. CV of Ni- (red), 3:1 Ni:Fe- (blue), and Fe- (green) oxide catalysts. Carbon paper back ground is shown in gray. CVs were taking at a scan rate of 10 mV/s.

Cyclic voltammograms (CV) of Ni, Fe, and 3:1 NiFe catalysts are shown in Figure 4-4. The NiFe catalyst has an onset potential of < 1.5 V, while the Ni and Fe catalysts exhibit onset potentials 100–150 mV higher. The Ni catalyst shows a quasireversible redox feature with $E_{1/2}$=1.35 V and the introduction of Fe into the Ni-oxide material results in a positive shift of the

$Ni^{+2/+3}$ redox feature.[5,6d,6e] The anodic wave of the 3:1 NiFe catalyst is nearly merged with the catalytic wave, however a cathodic wave is evident. The Fe catalyst exhibits the highest onset potential and no redox features were observed, consistent with previous reports.[13]

4.2.4 Mössbauer Measurements

CVs were recorded prior to operando experiments and used to identify potentials for Mössbauer measurements (Figure 4-5a). Electrodes with higher catalyst loadings were used for Mössbauer measurements but proper iR compensation could not be performed by our instrument as a result of the high currents generated. Consequently, CV of the NiFe catalyst used in the Mössbauer experiment does not show a well-defined anodic feature for the oxidation of Ni^{+2}. However, currents observed at the onset (1.49 V) of the apparent catalytic wave is still ascribed to that of Ni^{+2} oxidation based on CV recorded on the NiFe electrode used for electrochemical experiment (Figure 4-4), where it was demonstrated that the oxidation of Ni^{+2} precedes OER. Mössbauer spectrum of the NiFe catalyst acquired under open-circuit conditions (Figure 4-5b) exhibited a doublet with an isomer shift (δ) of 0.34 mm/s and quadrupole splitting (Δ) of 0.5 mm/s, and no change was observed at the onset of Ni^{+2} oxidation (1.49 V, Figure 4-5c). When applied potential was increased to 1.62 V where significant OER takes place, a new singlet with δ = -0.27 mm/s was observed, consistent with oxidation of Fe sites in the material (Figure 4-5d). Further increase in the applied potential to 1.76 V resulted in an increase in the population of this species from 12% to 21% of the total Fe. Upon re-applying a potential of 1.49 V to the electrode, the current returns to the similar lower value observed during the initial application of 1.49 V. However, the oxidized Fe species is still present under this condition (Figure 4-5f). After allowing the catalyst to remain at open circuit for two days, an ex situ spectrum collected showed that the oxidized Fe species is no longer present (Figure 4-5g). In contrast, the only Fe species observed in

the Fe catalyst under all conditions is a doublet with $\delta \approx 0.36$ mm/s and $\Delta \approx 0.65$ mm/s (Figure 4-5h-j, Table 4-3).

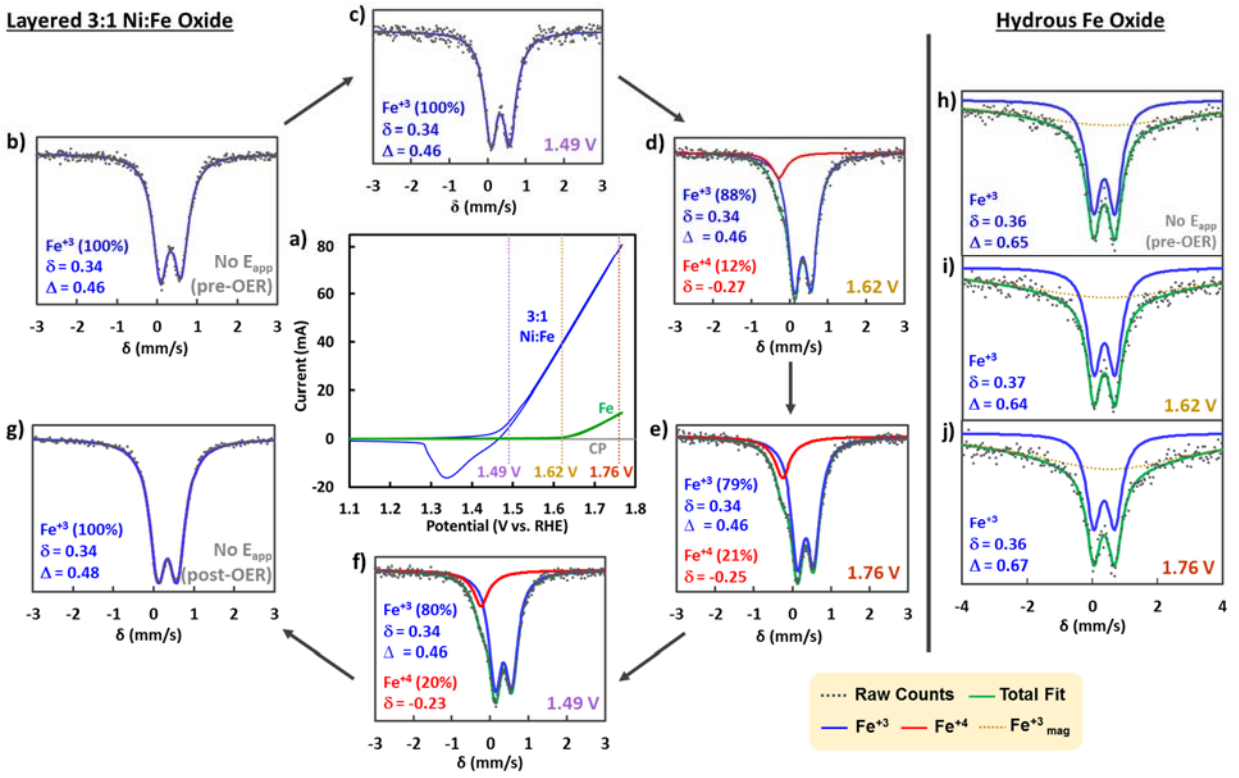

Figure 4-5. CV of layered NiFe-oxide (blue) and hydrous Fe-oxide (green) electrocatalysts (a) used for the operando experiments with corresponding Mössbauer spectra of each catalyst collected at open circuit, at 1.49 V (purple), 1.62 V (yellow), and 1.76 V (orange). CV data was recorded in the Mössbauer-electrochemical cell with a scan rate of 25 mV/s prior to Mössbauer measurements. These data are not normalized and the high current prevented proper iR compensation by our potentiostat.

A doublet with $\delta \approx 0.34$ mm/s is consistent with those previously reported for the un-oxidized layered NiFe oxides[7a,8] and is indicative of high-spin Jahn-Teller-distorted Fe^{+3} species.[8b] Similar doublets have also been reported for the common polymorphs of hydrous Fe oxides (i.e. α/β/γ/δ-FeOOH); however, Mössbauer parameters varies significantly.[14] A second broad peak was observed in the Fe-only catalyst spectra (Figure 4-5h-j). This peak can be attributed to the same Fe^{+3} site of FeOOH in larger oxide particles where magnetism has not fully randomized at room temperature.[15] While the isomer shift values were nearly identical for the two catalysts, Fe catalyst

exhibited stronger quadrupole splitting. This indicate that the Fe^{+3} sites in the two catalysts have similar electronic environment, but Fe catalyst has a more distorted structure.

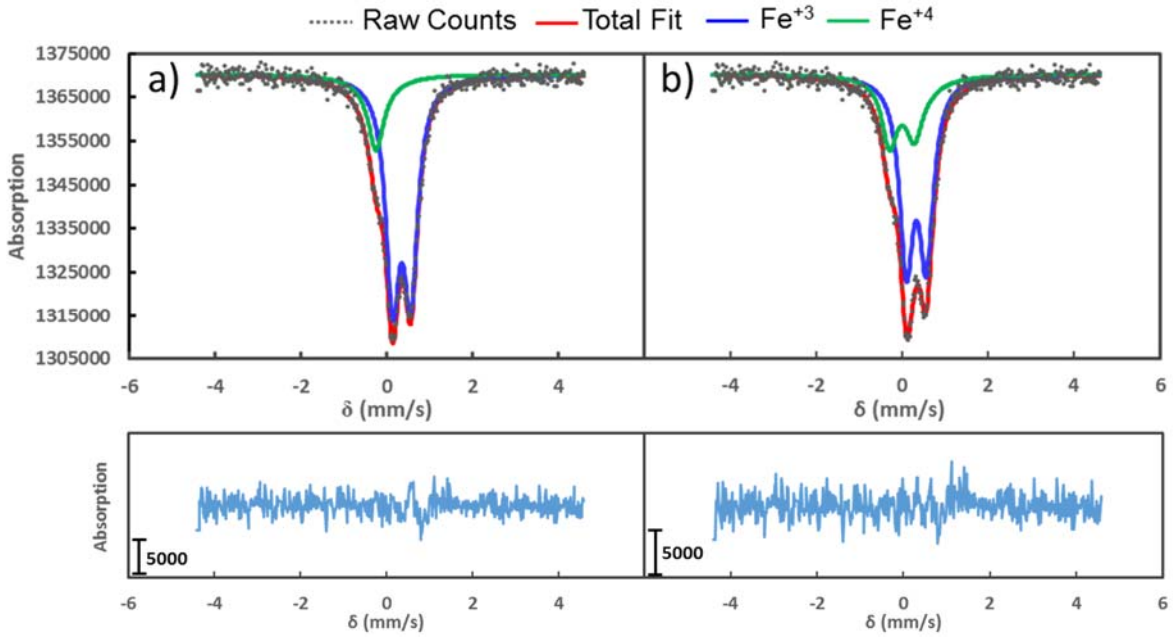

Figure 4-6. Two sets of parameters were found to produce reasonable fit for the Fe^{+4} specie. One consist of fitting the new species as a doublet with an isomer shift near zero (a). Alternatively, a singlet with an isomer shift at -0.25 mm/s and a quadrupole splitting of ~0.6 mm/s (b) also provided a good fit. Lower panel shows the difference spectrum between the raw data and the sum of Fe^{+3} and Fe^{+4} fits for each type of fitting, demonstrating that good fit is obtained in both cases.

Mössbauer parameters and quantification of the oxidized Fe species reported above were obtained from fitting this species as a singlet. However, the oxidized Fe species fits equally well as a doublet (Figure 4-6) with $\delta \approx 0.0$ and $\Delta \approx 0.58$ (see Table 4-2). Both isomer shifts are characteristic of Fe^{+4} species and have been reported for charged NiFe-LDH electrodes;[8] a singlet is characteristic of high spin Fe^{+4} species in a highly symmetrical environment, and a doublet is characteristic of low spin Fe^{+4} species in an unsymmetrical environment.[8b,16] The present data cannot distinguish between the low and high spin configurations; however, previous extended X-ray absorption fine structure analysis of anodized hydrous NiFe oxides reported only one Fe-O bond length, supporting a symmetrical environment about the oxidized Fe site.[7b,7c,7d] Based on

these precedents, we have chosen to fit the Fe^{+4} species as a singlet. No direct evidence for an oxidized Fe species was observed in the Fe catalyst, however, the presence of such oxidizing Fe intermediate cannot be excluded. We presume that OER by a hydrous Fe-oxide catalyst involves a highly oxidized Fe intermediate that rapidly oxidize water and is extremely short-lived.[13] Consequently, such species cannot be detected by conventional Mössbauer spectroscopy.

A synergistic modulation is observed between the Ni and Fe sites in the layered NiFe-oxide catalyst. As demonstrated previously, the electron-withdrawing effect of Fe^{+3} on NiFe-oxide catalysts is manifested in the anodic shift of the Ni^{+2} oxidation feature upon Fe incorporation into Ni-oxide catalysts (Figure 4-2).[2a,2f,5,6d,6e] Once oxidized, however, the NiOOH lattice (consists of Ni^{+3}/Ni^{+4}) exhibit an electron-donating influence on the Fe^{+3} sites, resulting in its facile oxidation to Fe^{+4}. Our data showed that at 1.62 V, no electrochemical activity is apparent in the Fe-oxide catalyst and only Fe^{+3} species is present. However, significant OER activity is observed in the NiFe-oxide catalyst along with 12% Fe^{+4} species. At 1.76 V, OER was observed in both catalysts but Fe^{+4} remained undetected in the Fe-oxide catalyst. Furthermore, that the population of Fe^{+4} was unchanged when the applied potential was reversed to 1.49 V indicates that the observed Fe^{+4} species is significantly stabilized when embedded in the NiOOH lattice.

The electron-withdrawing effect of Fe^{+3} and the electron-donating influence of NiOOH lattice can be rationalized through the donating ability of the oxygen ligand. When an oxygen is ligated to Fe^{+3}, it can engage in both σ- and π-donation because all the d-orbitals of Fe^{+3} (O_h, HS, d^5) are half filled. In contrast, Ni^{+2}, Ni^{+3} or Ni^{+4} (O_h, LS, d^8, d^7 and d^6 respectively) has no unfilled π-symmetry t_{2g} orbitals (i.e. d_{xy}, d_{xz}, d_{yz}), hence, an oxygen ligand can only engage in σ-donation to these Ni centers. In other words, the oxidation of Ni^{+2} is more difficult in the presence of Fe^{+3} due to the resulting electron-deficient oxygen ligands, while electron-rich oxygen ligands in NiOOH

lattice facilitate the oxidation of Fe^{+3} and a long-lived Fe^{+4} species can be detected. However its long lifetime is inconsistent with a species directly involved in catalysis. We believe that such stable Fe^{+4} species must exist within the plane of the oxide layers where it can be fully ligated to 6 oxygen ligands. This Fe^{+4} species is easily accessible but does not possess sufficient oxidation potential to evolve oxygen. Nevertheless, it likely modulates the oxidizing ability of nearby sites, which results in the enhancement of OER activity. In contrast, Fe sites near the edges of the NiOOH layers is only partially ligated. Presumably, such species can achieve a balance between having sufficient potential to oxidize water while not requiring large excess overpotential.

4.3 Conclusion

In conclusion, Fe^{+4} was only detected in the layered NiFe-oxide catalyst by Mössbauer spectroscopy during steady-state OER, demonstrating the stabilizing effect of the NiOOH lattice. However, the long lifetime of this Fe^{+4} species suggests it is not direct involved in water oxidation. We propose that the observed Fe^{+4} is embedded within the plane of the NiOOH layers but improves the oxidizing ability of nearby metal sites. Furthermore, partially ligated Fe species at the edge of the oxide layer might possess a balanced oxidation potential for easy access to high-valent species with minimal overpotential for OER.

4.4 Experimental Details

4.4.1 Materials

All chemicals were purchased from Sigma Aldrich in the highest purity available and used as received except for $FeSO_4 \bullet 7H_2O$. $FeSO_4 \bullet 7H_2O$ was recrystallized and stored under N_2 to avoid oxidation of Fe^{+2} to Fe^{+3}. ^{57}Fe metal was purchased from ISOFLEX and converted into $^{57}FeSO_4 \bullet 7H_2O$ (vide infra). Carbon paper (CP) was purchased from Fuel Cell Earth and was

subjected to hydrophilic treatment before use (vide infra). N_2 purged ultrapure water (18 MΩ, Thermo-Scientific) was used to prepare all aqueous solution. Hg/HgO reference electrode (1 M KOH) and Pt mesh counter electrode (BASi Analytical Instruments) were used in all electrochemical experiments.

4.4.2 Syntheses

4.4.2.1 $^{57}FeSO_4 \bullet 7H_2O$

Note: *excessive care was taken to keep ^{57}Fe from exposure to O_2 throughout the entire reaction*. A 10 cm piece of Tygon tubing threaded through a rubber septum was fitted to the tip of a 50 mL plastic syringe. The syringe was filled with N_2 purged 25% (v/v) H_2SO_4 in a N_2 purge box. A 1 g piece of ^{57}Fe metal was placed into a 100 mL 3-neck round bottom flask (RBF) and kept under active N_2 flow. The RBF was sealed with a rubber septum fit with a plastic syringe and 25% (v/v) H_2SO_4 was slowly added to the ^{57}Fe metal under active stirring and N_2 flow while the flask was heated to 70 ^oC. After 30 mL of acid solution was added, reaction was left to stir at 70 ^oC or until all metal has dissolved. (Degassed H_2O was syringed into the flask if evaporation became too significant and more acid solution was added if not all metal has dissolved after 12 hours).

Once all metal was dissolved (very pale-green solution), a Dean-Stark trap was fitted to the RBF and the reaction temperature increased to 105-110 ^oC to remove H_2O. When H_2O was removed, white solids were left in the flask with H_2SO_4, which were transferred into a pipette fitted with a polypropylene frit. N_2 was used to push H_2SO_4 out of the syringe pipette and the solid was left to dry under the N_2 stream for one hour. The white solid was transferred into the N_2 purge box and recrystallized as $^{57}FeSO_4 \bullet 7H_2O$ using a minimal amount of degassed H_2O at 70 ^oC. This solution was subsequently sealed and transferred to a 4 ^oC refrigerator until green crystals appeared.

4.4.2.2 Hydrophilic-Treated Carbon Paper

Each side of the carbon paper was first cleaned with plasma (O_2 gas) at 150 W for 5 minutes. Subsequently, the carbon paper was annealed in an inert atmosphere at 800 ^oC for 5 minutes to remove oxidized contaminant from the surface of the carbon paper. The resulting paper is thinner and very brittle, but no longer floats on water after some agitation.

4.4.2.3 Preparation of Ni/Fe-LDH Catalyst on Carbon Paper Electrode

Hydrophilic-treated carbon paper (3.5 cm x 0.8 cm) and urea (5 equiv.) were placed into a 6 mL glass vial and transferred into a purge box for catalyst generation. In the purge box, stock solutions of $Ni(NO_3)_2 \bullet 6H_2O$ (1 M) and $^{57}FeSO_4 \bullet 7H_2O$ (0.1 M) were prepared from degassed H_2O. Appropriate amounts of $^{57}FeSO_4$ stock solution were placed into a glass vial, followed by triethanolamine (TEA, 10 mM stock solution, 1 equiv. to Fe^{+2}) and mixed (a green Fe^{+2}-TEA complex precipitated shortly after mixing but re-dissolved during hydrothermal treatment). Subsequently, appropriate amounts of $Ni(NO_3)_2$ stock solution was added and mixed. The entire solution mixture was transferred into a vial containing CP and urea and mixed until the urea had dissolved and CP was fully wetted. The reaction mixture was then sealed under N_2 and placed into a furnace (preheated) for 6 hours at 100 ^oC. At the end of the hydrothermal synthesis, carbon paper was removed from the glass vials, rinsed with ultrapure water, and stored in a glass vial with just enough water to keep the carbon paper wet. Catalysts with 25% and 100% Fe were prepared (Table 4-1). For electrodes used in electrochemical experiments, $[M]_{tot}$ was kept <4 mM.

Table 4-1. Specific Reaction Conditions Employed for Catalyst Synthesis

Final Catalyst	$[M]_{tot}$ (mM)	Ni:Fe	TEA	Urea (mg)	Vol_{tot} (ml)	Temp.	Final Ratio
25% Fe	16	3:1	1 [Fe] equiv.	5 $[M]_{tot}$ equiv.	2.0	100 ^oC	3.6(±0.5):1
100% Fe	9	0:1	1 [Fe] equiv.	5 $[M]_{tot}$ equiv.	2.0	100 ^oC	100% Fe

4.4.3 Characterization

Powder X-ray diffraction patterns (pXRD) were recorded using the Bruker D8 Advance system equipped with the LYNXEYE detector and a Cu Kα X-ray tube. The detector was operated at 50 kV and 50 mA and scans were collected between the range of 5° - 75° with a step size of 0.01° and an exposure time of 5 s per step. SEM images and EDX elemental analysis were performed using a ZEISS-LEO SUPRA 55 VP scanning electron microscope coupled with the NORAN SYSTEM SEVEN energy dispersive X-ray spectroscopy detector (ThermoFisher-Scientific).

4.4.4 *Operando* Mössbauer-Electrochemical Cell

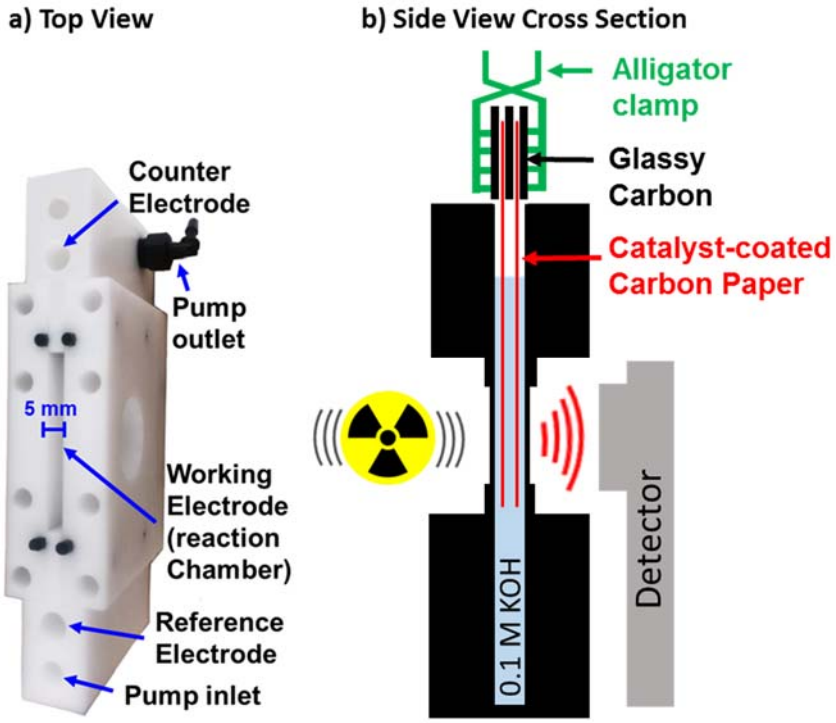

Figure 4-7. *Operando* Mössbauer-electrochemical cell. (a) Top view showing the various parts of the cell. (b) Side-view cross section schematic representation of the cell with the working electrode assembly inserted.

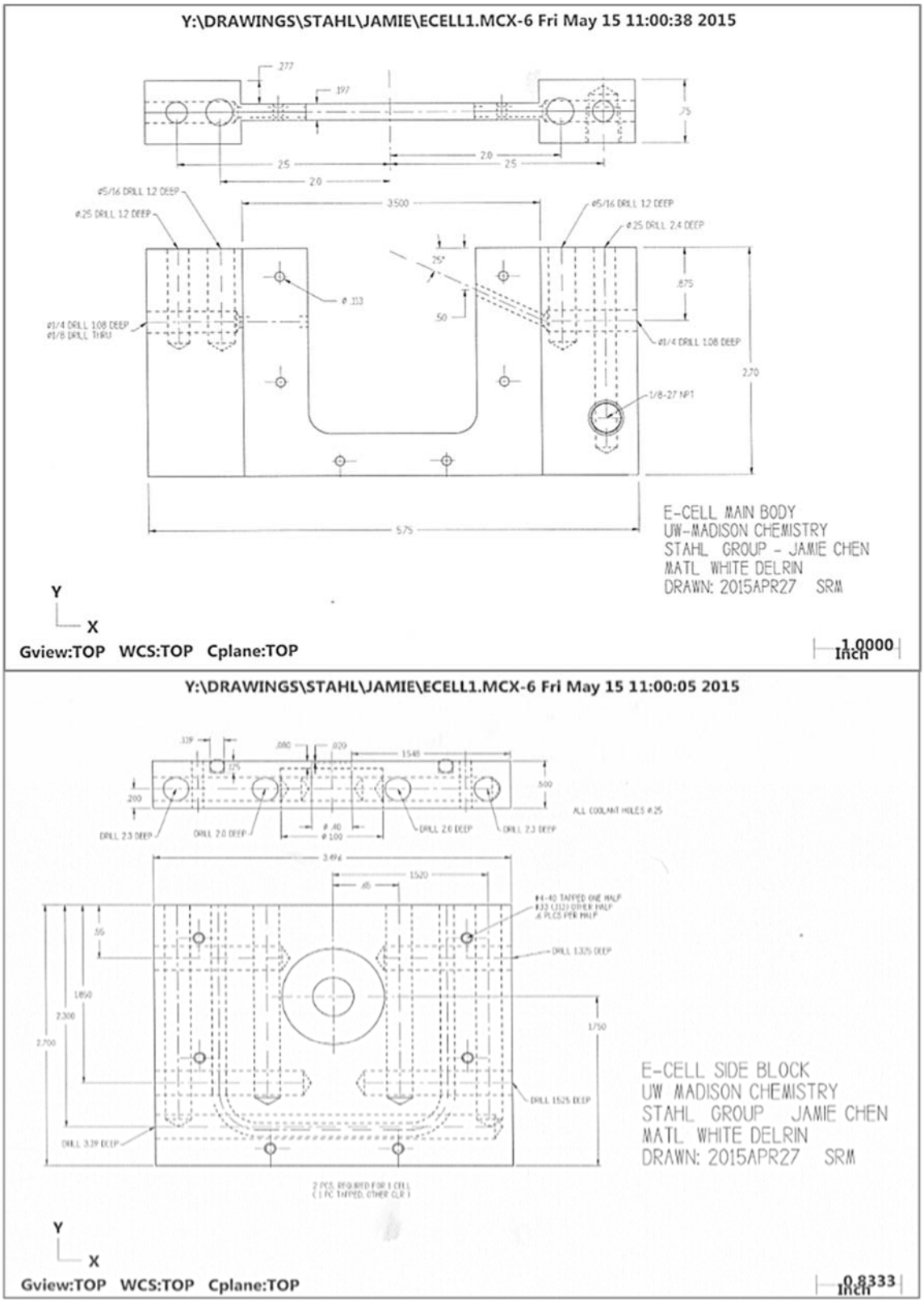

Scheme 4-1. Design prints for constructing the *operando* Mössbauer-electrochemical cell. a) Middle piece housing compartments for counter and reference electrodes. b) Front and back pieces (identical) of the cell with ducts drilled within the thickness of the wall for temperature control capabilities.

A Delrin electrochemical cell was constructed for the *in operando* Mössbauer experiments (Scheme 4-1). Two thin windows (~0.6 mm thick, 8 mm diameter) were carved into both walls of the anode compartment (5 mm width, Figure 4-7) in line with the γ-ray source and detector. A 5 mm width was chosen for the anode compartment to avoid excess attenuation of γ-ray (50% transmittance with 5 mm of water) but still allow for the stacking of multiple electrodes to enhance Mössbauer signal quality during *in operando* measurements. A pump was used to continuously circulate 95 mL (in 150 ft of 1/8" ID Tygon tubing) of 0.1 M KOH throughout data acquisition.

4.4.5 Mössbauer Measurements

Mössbauer experiments were conducted with a ^{57}Co source in a Pd matrix, using a constant acceleration drive. The spectrometer was calibrated using an iron foil. The ^{57}Co source used was a point source with 0.5 mm diameter, and the relative activity was 10 mCi. A VORTEX detector with 150 eV resolution was used to discriminate the 14.41 keV radiation. Data analysis was performed using in-house software. All data presented were taken at room temperature. The samples were prepared from fully enriched $^{57}FeSO_4 \bullet 7H_2O$.

Ex-situ measurements were collected by stacking 4 wet catalyst/CP pieces. The catalyst/CP pieces were kept wet during acquisition by placement in a small plastic bag with a couple drops of water. The plastic bag was subsequently taped onto the sample holder. Typical acquisition time ranged from 18-24 hours.

The cell was snuggly positioned between the source and the detector inside a lead cage. The pump and the potentiostat were positioned outside the cage, where a small opening on the lead cage (away from the source) guided the pump tubing and potentiostat leads inside to the cell (Figure 4-8). The cell was replenished with fresh 0.1 M KOH after data collection at each condition was completed.

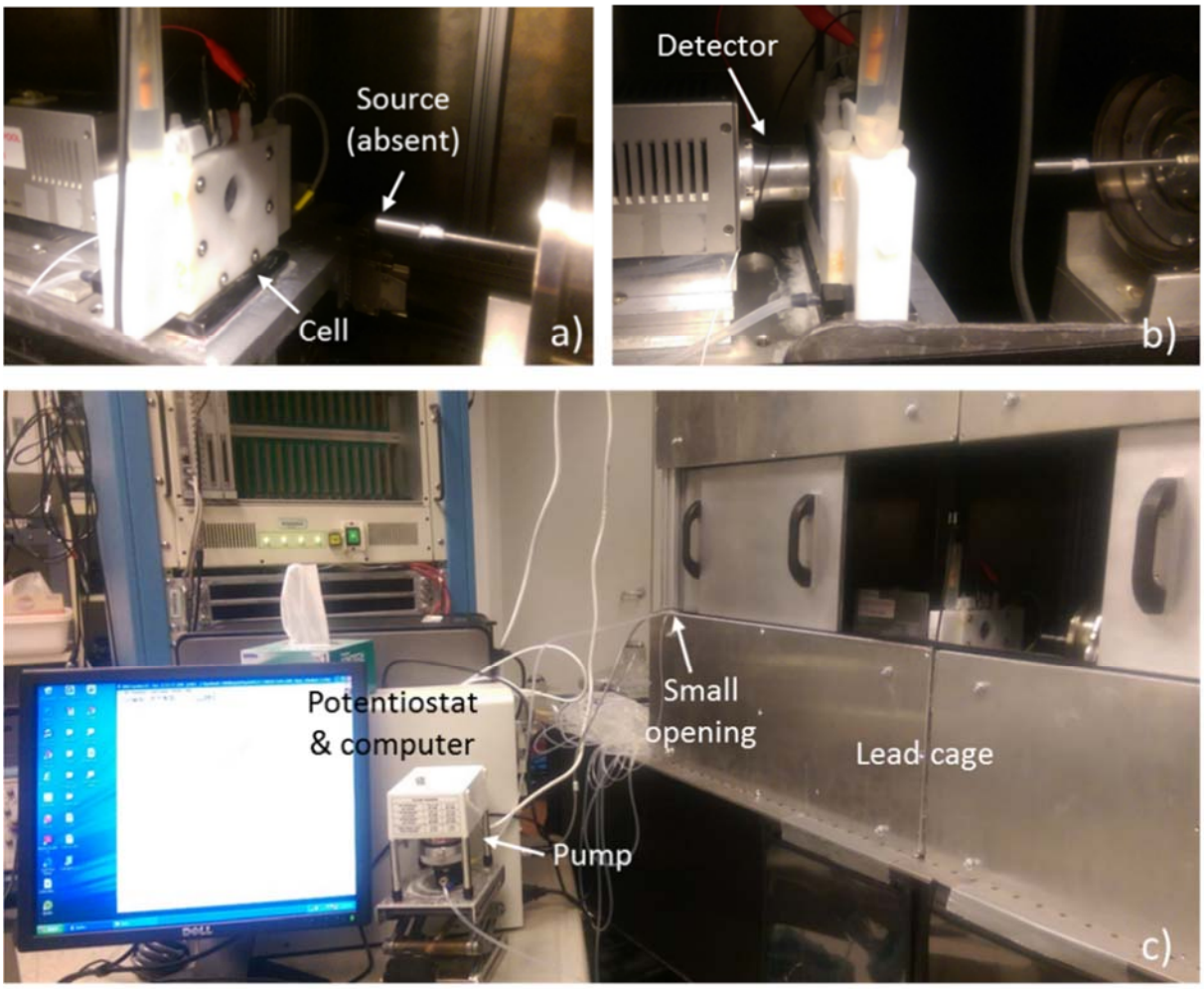

Figure 4-8. View of the experimental setup for *operando* Mössbauer experiment from a) source side b) detector side and c) outside the lead cage.

The working electrode assembly was prepared as follows: the top of each catalyst/CP piece was wrapped together securely with a thin strip of Cu using white teflon tape. The uncovered portion of the Cu strip was then sandwiched between pieces of glassy carbon electrode (1 mm thick), which was tightly clamped with a large alligator clamp. This entire working electrode assembly (Figure 4-9) was then connected to the potentiostat by clamping the working electrode clip on the large alligator clamp. Two pieces of catalyst/CP were used in all *operando* experiments.

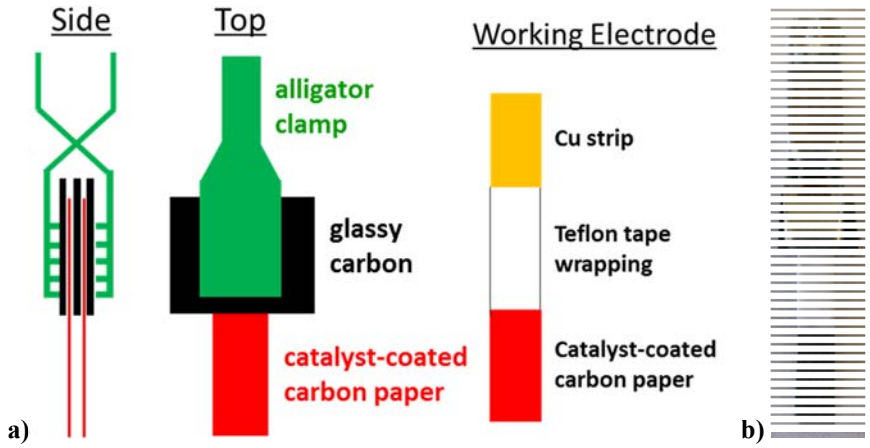

Figure 4-9. (a) Schematic representation of the working electrode assembly. (b) Pictorial view of the working electrode assembly used in *operando* Mössbauer measurements

Table 4-2. Mössbauer Parameters for the layered 3:1 NiFe-Oxide Catalyst

Layered 3:1 NiFe-Oxide Catalyst									
	Site 1 (Fe^{+3})				Site 2 (Fe^{+4})				χ^2
	% Comp	IS	QS	Width	% Comp	IS	QS	Width	
No E_{app}- start	1	0.34	0.5	0.44					1.13
1.49 V	1	0.34	0.49	0.42					0.99
1.62 V (Fe^{+4} as doublet)	0.796	0.34	0.46	0.39	0.204	-0.007	0.59	0.415	0.92
1.62 V ($Fe^{+4\ as}$ as singlet)	0.885	0.34	0.46	0.39	0.115	-0.27	0	0.415	0.91
1.76 V (Fe^{+4} as doublet)	0.678	0.34	0.46	0.39	0.322	0.004	0.58	0.415	1.09
1.76 V (Fe^{+4} as singlet)	0.794	0.34	0.46	0.39	0.206	-0.25	0	0.415	1.12
1.49 V_2^{nd} (Fe^{+4} as doublet)	0.686	0.34	0.46	0.39	0.314	0.012	0.56	0.415	1.13
1.49 V_2^{nd} (Fe^{+4} as singlet)	0.803	0.34	0.46	0.39	0.197	-0.23	0	0.415	1.14
No E_{app}- end	1	0.34	0.48	0.485					5.88

Table 4-3. Mössbauer Parameters for the hydrous Fe-Oxide Catalyst.

Hydrous Fe-Oxide Catalyst									
	Site 1 (Fe^{+3})				Site 2 (Fe^{+3} with randomizing magnetism)				χ^2
	% Comp	IS	QS	Width	% Comp	IS	QS	Width	
No E_{app}-start	0.395	0.36	0.65	0.542	0.602	0.53	0	6.35	1.02
1.49 V	0.31	0.37	0.65	0.542	0.689	0.37	0	8.62	1.03
1.62 V	0.322	0.37	0.64	0.542	0.673	0.48	0	6.97	1.10
1.76 V	0.29	0.36	0.65	0.542	0.71	0.55	0	6.12	0.98
No E_{app}-end	0.355	0.36	0.64	0.52	0.645	0.35	0	5.35	1.42

4.4.6 Spectroscopic Data of Electrodeposited NiFe-LDH Catalysts

Our early efforts in spectroscopic investigation of NiFe-LDH used catalyst materials prepared via the method reported by Bell. However, a significant amount of metallic Ni and Fe phases were detected by both and Mössbauer and XAS spectroscopy. Evidence of the metallic phase can be seen in the Mössbauer spectrum collected at room temperature (Figure 4-10) where a distinct sextuplet corresponding to metallic Fe with IS=0.13 and magnetic splitting H=324.5 is present. Metallic phases are also apparent in both the XANES and EXAFS spectra (Figure 4-11).

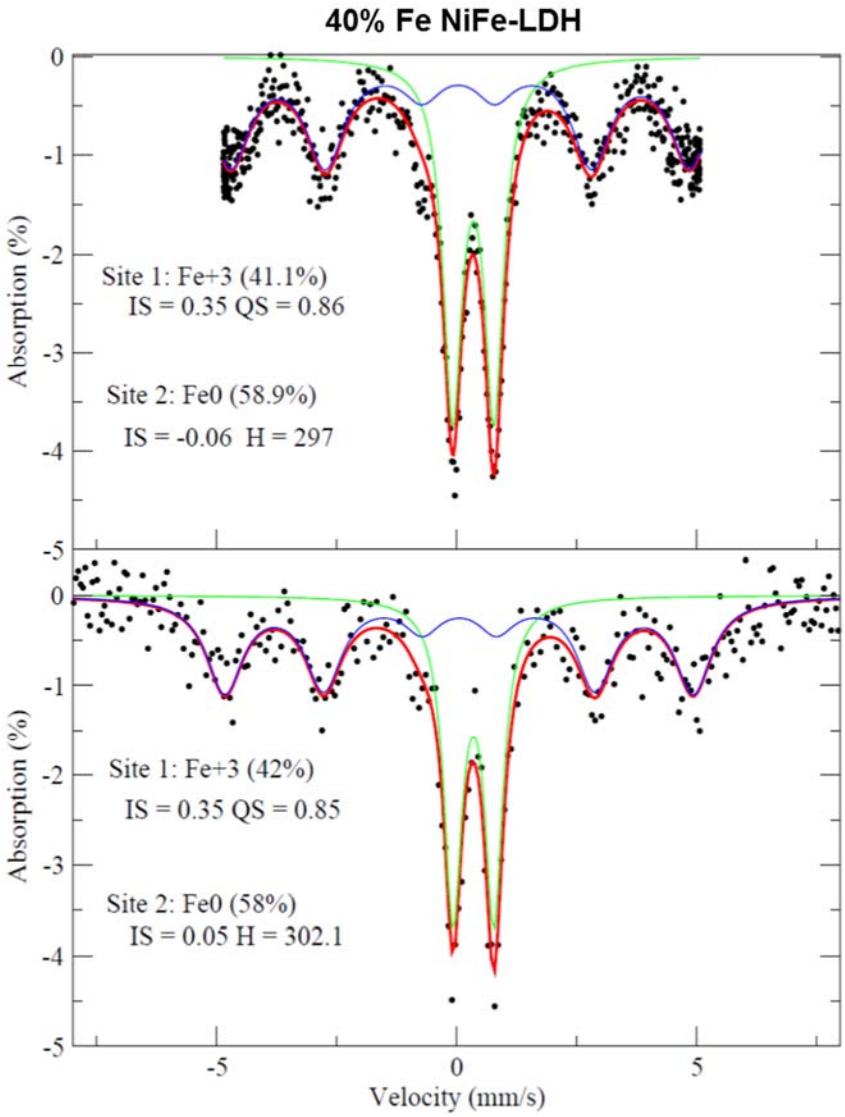

Figure 4-10. Mössbauer spectra of electrodeposited 40% Fe NiFe-LDH collected at two different velocities at room temperature. Sextuplet of the metallic Fe can be readily identified

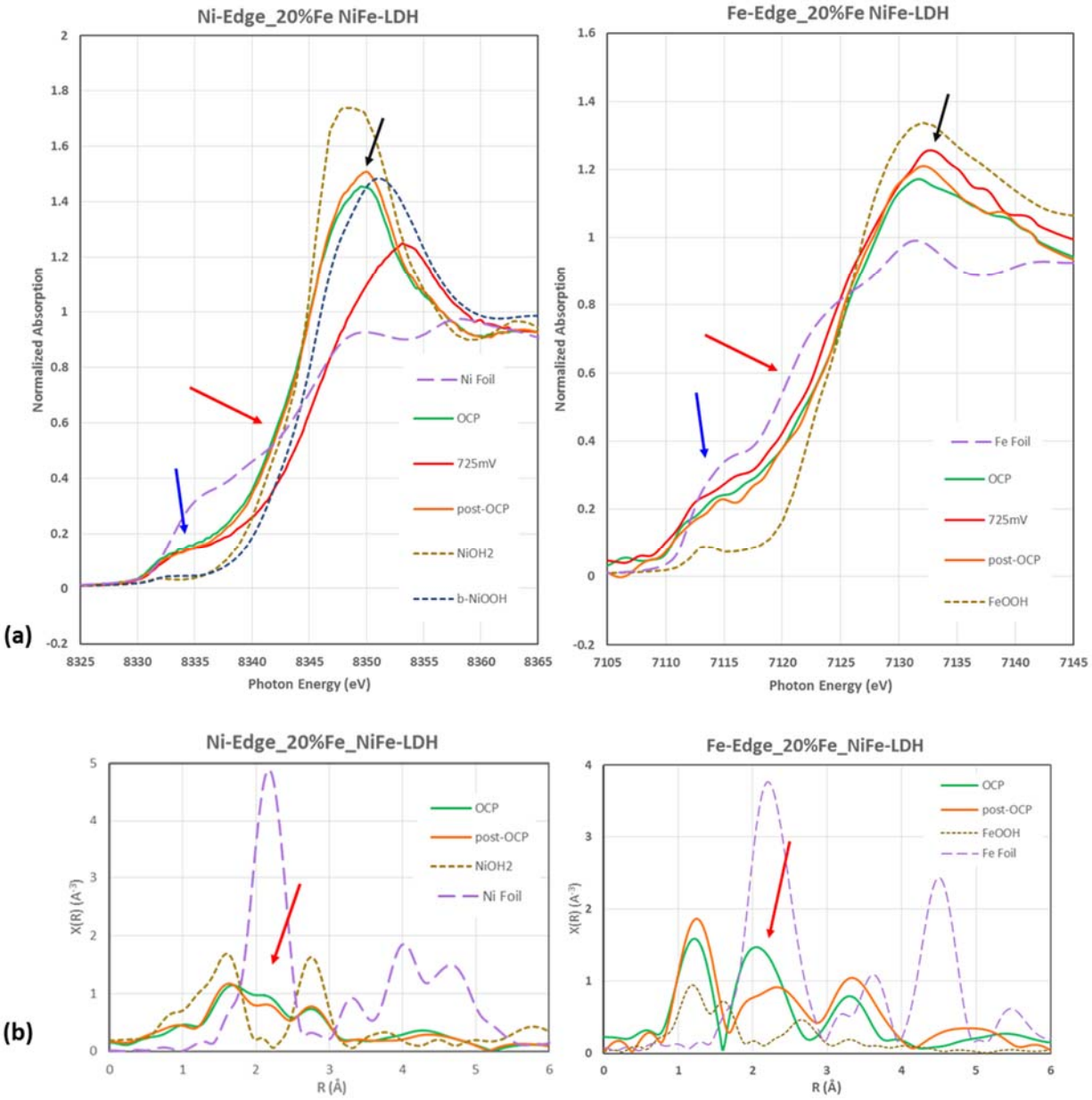

Figure 4-11. Ni and Fe K-edge (a) XANES and (b) EXAFS spectra of electrodeposited 20% Fe NiFe-LDH. Arrows points to features in each spectrum where the presence of metallic phase is evident.

4.5 References

1. For selected reviews on metal oxide electrocatalysts: (a) Dau, H.; Limberg, C.; Reier, T.; Risch, M.; Roggan, S.; Strasser, P. *ChemCatChem* **2010**, *2*, 724-761. (b) Walter, M. G.; Warren, E. L.; McKone, J. R.; Boettcher, S. W.; Mi, Q. X.; Santori, E. A.; Lewis, N. S. *Chem. Rev.* **2010**, *110*, 6446-6473. (c)

Surendranath, Y.; Nocera, D. G. In *Progress in Inorganic Chemistry, Vol 57*; Karlin, K. D., Ed.; John Wiley & Sons Inc: Hoboken, 2012; Vol. 57, p 505-560. (d) Singh, A.; Spiccia, L. *Coord. Chem. Rev.* **2013**, *257*, 2607-2622. (e) Galan-Mascaros, J. R. *ChemElectroChem* **2015**, *2*, 37-50. (f) Gong, M.; Dai, H. J. *Nano Res* **2015**, *8*, 23-39.

2. For leading references, see: (a) Corrigan, D. A. *J. Electrochem. Soc.*, **1987**, *134*, 377-384. (b) Miller, E. L.; Rocheleau, R. E. *J. Electrochem. Soc.* **1997**, *144*, 3072-3077. (c) Trotochaud, L.; Ranney, J. K.; Williams, K. N.; Boettcher, S. W. *J. Am. Chem. Soc.* **2012**, *134*, 17253-17261. (d) McCrory, C. C. L.; Jung, S. H.; Peters, J. C.; Jaramillo, T. F. *J Am Chem Soc* **2013**, *135*, 16977-16987. (e) Smith, R. D. L.; Prévot, M. S.; Fagan, R. D.; Trudel, S.; Berlinguette, C. P. *J. Am. Chem. Soc.* **2013**, *135*, 11580-11586. (f) Chen, J. Y. C.; Miller, J. T.; Gerken, J. B.; Stahl, S. S. *Energy Environ. Sci.* **2014**, *7*, 1382-1386. (g) Wang, H. T.; Lee, H. W.; Deng, Y.; Lu, Z. Y.; Hsu, P. C.; Liu, Y. Y.; Lin, D. C.; Cui, Y. *Nat. Commun.* **2015**, *6*.

3. (a) Gerken, J. B.; Chen, J. Y. C.; Massé, R. C.; Powell, A. B.; Stahl, S. S. *Angew. Chem. Int. Ed.* **2012**, *51*, 6676-6680. (b) Gerken, J. B.; Shaner, S. E.; Massé, R. C.; Porubsky, N. J.; Stahl, S. S. *Energy Environ. Sci.* **2014**, *7*, 2376-2382.

4. For other examples of Ni-Fe-M3 oxides with high OER electrocatalytic activity, see: (a) Singh, R. N.; Singh, N. K.; Singh, J. P. *Electrochim. Acta* **2002**, *47*, 3873-3879; (b) Singh, R. N.; Singh, J. P.; Cong, H. N.; Chartier, P. *Int. J. Hydrogen Energy* **2006**, *31*, 1372-1378. (c) Anindita; Singh, A.; Singh, R. N. *Int. J. Hydrogen Energy* **2010**, *35*, 3243-3248. (d) Kumar, M.; Awasthi, R.; Sinha, A. S. K.; Singh, R. N. *Int. J. Hydrogen Energy* **2011**, *36*, 8831-8838.

5. (a) G. Młynarek, M. Paszkiewicz and A. Radniecka, *J. Appl. Electrochem.*, **1984**, *14*, 145-149. (b) S. I. Córdoba, R. E. Carbonio, M. L. Teijelo and V. A. Macagno, *Electrochim. Acta*, **1987**, *32*, 749-755. (c) E. Potvin and L. Brossard, *Mater. Chem. Phys.*, **1992**, *31*, 311-318. (d) M. D. Merrill and R. C. Dougherty, *J. Phys. Chem. C*, **2008**, *112*, 3655-3666.

6. (a) Hong, D.; Yamada, Y.; Nagatomi, T.; Takai, Y.; Fukuzumi, S. *J. Am. Chem. Soc.* **2012**, *134*, 19572-19575. (b) J. Landon, E. Demeter, N. İnoğlu, C. Keturakis, I. E. Wachs, R. Vasić, A. I. Frenkel and J.

R. Kitchin, *ACS Catalysis*, **2012**, *2*, 1793-1801. (c) M. Gong, Y. Li, H. Wang, Y. Liang, J. Z. Wu, J. Zhou, J. Wang, T. Regier, F. Wei and H. Dai, *J. Am. Chem. Soc.*, **2013**, *135*, 8452-8455. (d) M. W. Louie and A. T. Bell, *J. Am. Chem. Soc.*, **2013**, *135*, 12329-12337. (e) Trotochaud, L.; Young, S. L.; Ranney, J. K.; Boettcher, S. W. *J. Am. Chem. Soc.* **2014**, *136*, 6744-6753.

7. (a) Corrigan, D. A.; Conell, R. S.; Fierro, C.; Scherson, D. A. *J. Electrochem. Soc.* **1987**, *134*, C131-C131. (b) Kim, S. H.; Tryk, D. A.; Antonio, M. R.; Carr, R.; Scherson, D. *J. Phys. Chem.* **1994**, *98*, 10269-10276. (c) Balasubramanian, M.; Melendres, C. A.; Mini, S. *J. Phys. Chem. B* **2000**, *104*, 4300-4306. (d) Friebel, D.; Louie, M. W.; Bajdich, M.; Sanwald, K. E.; Cai, Y.; Wise, A. M.; Cheng, M. J.; Sokaras, D.; Weng, T. C.; Alonso-Mori, R.; Davis, R. C.; Bargar, J. R.; Norskov, J. K.; Nilsson, A.; Bell, A. T. *J. Am. Chem. Soc.* **2015**, *137*, 1305-1313.
8. Independent Mössbauer studies of layered NiFe oxides as battery cathode materials revealed the formation of Fe^{+4} species; however, the relevance of the conditions used in these studies and to those of OER is not straightforward. See the following: (a) Guerlou-Demourgues, L.; Fournes, L.; Delmas, C. *J. Electrochem. Soc.* **1996**, *143*, 3083-3088. (b) Axmann, P.; Erdbrügger, C. F.; Buss, D. H.; Glemser, O. *Angew. Chem. Int. Ed.* **1996**, *35*, 1115-1118.
9. For a selected list of methods: (a) Axmann, P.; Glemser, O. *J. Alloys Compd.* **1997**, *246*, 232-241. (a) Xiao, T.; Tang, Y. W.; Jia, Z. Y.; Li, D. W.; Hu, X. Y.; Li, B. H.; Luo, L. J. *Nanotechnology* **2009**, *20*. (b) Abellan, G.; Coronado, E.; Marti-Gastaldo, C.; Pinilla-Cienfuegos, E.; Ribera, A. *J Mater Chem.* **2010**, *20*, 7451-7455. (c) Han, Y. F.; Liu, Z. H.; Yang, Z. P.; Wang, Z. L.; Tang, X. H.; Wang, T.; Fan, L. H.; Ooi, K. *Chem. Mater* **2008**, *20*, 360-363.
10. This complication was noted, for example, by Bell and coworkers (see ref. 7d). Low electrode potentials (~ –0.9 V vs. Ag/AgCl) are needed to reduce water to H_2 and hydroxide ions and establish the pH gradient that leads to precipitation of the metal oxides. Undesired electroplating of Ni and Fe often occurs simultaneously with the desired metal-oxide electrodeposition at these potentials.
11. For a related preparation of a NiCo LDH on carbon paper, see: Liang, H. F.; Meng, F.; Caban-Acevedo, M.; Li, L. S.; Forticaux, A.; Xiu, L. C.; Wang, Z. C.; Jin, S. *Nano Lett.* **2015**, *15*, 1421-1427.

12. (a) Song, F.; Hu, X. *Nat Commun* **2014**, *5*. (b) Abellan, G.; Coronado, E.; Marti-Gastaldo, C.; Pinilla-Cienfuegos, E.; Ribera, A. *Journal of Materials Chemistry* **2010**, *20*, 7451-7455.

13. (a) Doyle, R. L.; Lyons, M. E. G. *J. Electrochem. Soc.* **2013**, *160*, H142-H154. (b) Wu, Y. Z.; Chen, M. X.; Han, Y. Z.; Luo, H. X.; Su, X. J.; Zhang, M. T.; Lin, X. H.; Sun, J. L.; Wang, L.; Deng, L.; Zhang, W.; Cao, R. *Angew. Chem. Int. Ed.* **2015**, *54*, 4870-4875.

14. See, for example: (a) Rossiter, M. J.; Hodgson, A. E. M. *J Inorg. Nucl. Chem.* **1965**, *27*, 63-71. (b) Dezsi, I.; Keszthel.L; Kulgawcz.D; Mcinar, B.; Eissa, N. A. *Phys Status Solidi* **1967**, *22*, 617-629. (c) Johnson, C. E. *J. Phys. Part C Solid* **1969**, *2*, 1996-2002. (d) Meppel, K. R. N.V., Ph.D. Dissertation, Delft University of Technology, 1972. (e) Murad, E.; Schwertmann, U. *Mineral Mag.* **1984**, *48*, 507-511. (f) Madsen, M. B.; Morup, S.; Koch, C. J. W.; Borggaard, O. K. *Surf. Sci.* **1985**, *156*, 328-334. (g) Pollard, R. J.; Cardile, C. M.; Lewis, D. G.; Brown, L. J. *Clay. Miner.* **1992**, *27*, 57-71.

15. Neel temperature (T_N) of FeOOHs depend on particle size (see ref. 13). Magnetic spins randomize at lower temperature for smaller crystallites, thus exhibiting a doublet at room temperature. Larger particles tend to exhibit sextuplets at room temperature due to the persistent magnetism. Among the polymorphs, α-FeOOH has the most persistent magnetism where particles <85Å are required for room temperature magnetism randomization, making it the least likely candidate for the FeOOH catalyst examined here. However, the room temperature spectrum of β-, γ-, and δ-FeOOH can frequently be found as either a doublet or a broad multiplet.

16. (a) Adler, P. *J Solid State Chem.* **1994**, *108*, 275-283. (b) Gallagher, P.K.; Macchesney, J. B.; Buchanan, D. N. *J. Chem. Phys.* **1964**, *41*, 2429-2434. (c) Takano, M.; Nakanishi, N.; Takeda, Y.; Naka, S.; Takada, T. *Mater Res Bull* **1977**, *12*, 923-928.

Appendix I

Optimization of NiFe-LDH Synthesis directly on Carbon Paper

This section describes the optimization of reaction condition in order to obtain NiFe-LDH of the desired ratio and loading for *in operando* Mössbauer experiment. In particular the use of $FeSO_4•7H_2O$ was required since $^{57}FeSO_4•7H_2O$ was our available source of enriched Fe. We also aimed to carry out each reaction using the least amount of $FeSO_4•7H_2O$ because only a limited quantity of $^{57}FeSO_4•7H_2O$ was available. The lower limit of detection for conventional Mössbauer measurements is 0.1 mg Fe/cm^2. The hydrothermal synthesis condition was initially based on that described by Tang et al..[1] Each of the following subsection will discuss the modification made. $Ni(NO_3)_2•6H_2O$ was used in all cases and reaction time was always 6 hours.

Table 5-1. Anaerobic vs. Aerobic Condition

Fe Salt	EG:H_2O	Atm.	Temp.	Vol (soln/tot)	$[M]_{tot}$	Ni:Fe	[Urea]	Total Loading (mg)	Final Ni:Fe
$FeCl_2$	2:3	N_2	85 ºC	4.5/9	8 mM	15:1	160 mM	---	~8:1
$FeCl_2$	2:3	N_2	85 ºC	4.5/9	8 mM	9:1	160 mM	---	~5.5:1
$FeCl_2$	2:3	N_2	85 ºC	4.5/9	8 mM	4:1	160 mM	---	~4.5:1
$FeCl_2$	2:3	Air	85 ºC	4.5/9	8 mM	15:1	160 mM	---	~2.5:1
$FeCl_2$	2:3	Air	85 ºC	4.5/9	8 mM	9:1	160 mM	---	~2.5:1

Following procedure of Tang et al. which was performed in air, no control over the final Ni:Fe ratio was observed even with the use of $FeCl_2$ that was rigorously kept air-free. However, when the reaction was carried out anaerobically in a N_2 box using carefully degassed water, final Ni:Fe ratio can be systematically varied.

Table 5-2. $FeSO_4•7H_2O$ vs. $FeCl_2$

Fe Salt	EG:H_2O	Atm.	Temp.	Vol (soln/tot)	$[M]_{tot}$	Ni:Fe	[Urea]	Total Loading (mg)	Final Ni:Fe
$FeCl_2$	EG 10mM	N_2	85 °C	4.5/9	8 mM	9:1	160 mM	~0.06	~5.3:1
$FeCl_2$	EG 10mM	N_2	85 °C	4.5/9	8 mM	4:1	160 mM	~0.11	~4.7:1
$FeSO_4•7H_2O$	EG 10mM	N_2	85 °C	4.5/9	8 mM	9:1	160 mM	~0.05	~5:1
$FeSO_4•7H_2O$	EG 10mM	N_2	85 °C	4.5/9	8 mM	4:1	160 mM	~0.03	~6.5:1
$FeSO_4•7H_2O$	1:4	N_2	85 °C	4.5/9	8 mM	9:1	160 mM	~0.1	~4:1
$FeSO_4•7H_2O$	1:4	N_2	85 °C	4.5/9	8 mM	4:1	160 mM	~0.13	~4.3:1

This set of screening results demonstrates that $FeSO_4•7H_2O$ is a competent source of Fe^{+2} salt for the controlled synthesis of NiFe-LDH.

Table 5-3. TEA vs. EG and Reducing Urea Concentration

Fe Salt	EG:H_2O	Atm.	Temp.	Vol (soln/tot)	$[M]_{tot}$	Ni:Fe	[Urea]	Total Loading (mg)	Final Ni:Fe
$FeSO_4•7H_2O$	EG 100mM	N_2	85 °C	4.5/9	8 mM	4:1	160 mM	0.026	~4.5:1
$FeSO_4•7H_2O$	EG 100mM	N_2	85 °C	4.5/9	8 mM	4:1	40 mM	---	~3.4:1
$FeSO_4•7H_2O$	EG 100mM	N_2	85 °C	4.5/9	8 mM	1:1	160 mM	---	~2.2:1
$FeSO_4•7H_2O$	EG 100mM	N_2	85 °C	4.5/9	8 mM	1:1	40 mM	0.008	~2.4:1
$FeSO_4•7H_2O$	1:4	N_2	85 °C	4.5/9	8 mM	4:1	160 mM	0.042	~3.5:1
$FeSO_4•7H_2O$	1:4	N_2	85 °C	4.5/9	8 mM	4:1	40 mM	---	~3:1
$1FeSO_4•7H_2O$	1:4	N_2	85 °C	4.5/9	8 mM	1:1	160 mM	0.017	~2:1
$FeSO_4•7H_2O$	1:4	N_2	85 °C	4.5/9	8 mM	1:1	40 mM	0.068	~2.4:1
$FeSO_4•7H_2O$	1:4	N_2	85 °C	4.5/9	8 mM	4:1	160 mM	---	~4:1
$FeSO_4•7H_2O$	1:4	N_2	85 °C	4.5/9	8 mM	4:1	40 mM	---	~4:1
Fe Salt	**TEA**	**Atm.**	**Temp.**	**Vol (soln/tot)**	**$[M]_{tot}$**	**Ni:Fe**	**[Urea]**	**Total Loading (mg)**	**Final Ni:Fe**
$FeSO_4•7H_2O$	1 equiv [Fe]	N_2	100 °C	4.5/9	8 mM	4:1	40 mM	0.219	~4:1
$FeSO_4•7H_2O$	3 equiv [Fe]	N_2	100 °C	4.5/9	8 mM	4:1	40 mM	0.262	~4:1

This set of screening results demonstrates that using triethanolamine (TEA)[2] and 100 °C reaction temperature dramatically improved catalyst loading. Agreement was also observed between solution and final Ni:Fe ratios. Also a large excess of urea was not necessary and can be

kept at 5 equivalent relative to total metal concentration. A TEA:Fe^{+2} ratio of 1:1 also was sufficient.

Table 5-4. Effect of $[M]_{tot}$ on Catalyst Loading and Reducing Reaction Volume

Fe Salt	TEA	Atm.	Temp.	Vol (soln/tot)	$[M]_{tot}$	Ni:Fe	[Urea]	Total Loading (mg)	Final Ni:Fe
$FeSO_4•7H_2O$	1 eqv [Fe]	N_2	100 °C	3/6	16 mM	4:1	5 eqv $[M]_{tot}$	0.271	~4.8:1
$FeSO_4•7H_2O$	1 eqv [Fe]	N_2	100 °C	2/6	16 mM	4:1	5 eqv $[M]_{tot}$	0.400	~4.7:1
$FeSO_4•7H_2O$	1 eqv [Fe]	N_2	100 °C	2/6	16 mM	0:1	5 eqv $[M]_{tot}$	0.013	Fe only
$FeSO_4•7H_2O$	1 eqv [Fe]	N_2	100 °C	3/6	32 mM	4:1	5 eqv $[M]_{tot}$	0.512	~4:1
$FeSO_4•7H_2O$	1 eqv [Fe]	N_2	100 °C	2/6	32 mM	4:1	5 eqv $[M]_{tot}$	0.528	~5.1:1
$FeSO_4•7H_2O$	1 eqv [Fe]	N_2	100 °C	2/6	16 mM	3:1	5 eqv $[M]_{tot}$	0.390	~3.5:1

Increasing total metal concentration does increase total catalyst loading, however precipitates were observed in all of these reactions, especially those with 32 mM $[M]_{tot}$, thus 16 mM was chosen as the maximum $[M]_{tot}$. The precipitates observed is the TEA complex of Fe^{+2}, which has been reported to have low solubility in water.[3] However, when heated to 100 °C during hydrothermal reaction, it re-dissolves and hence the final Ni:Fe ratio was not so different from the solution ratio.

1. Xiao, T.; Tang, Y. W.; Jia, Z. Y.; Li, D. W.; Hu, X. Y.; Li, B. H.; Luo, L. J. *Nanotechnology* **2009**, *20*.
2. (a) Abellan, G.; Coronado, E.; Marti-Gastaldo, C.; Pinilla-Cienfuegos, E.; Ribera, A. *J. Mater. Chem.* **2010**, *20*, 7451-7455. (b) Song, F.; Hu, X. *Nat. Commun.* **2014**, *5*.
3. Wen, Y. H.; Zhang, H. M.; Qian, P.; Zhou, H. T.; Zhao, P.; Yi, B. L.; Yang, Y. S. *Electrochim Acta* **2006**, *51*, 3769-3775.